


Radar Based Estimation of  
Asymmetric Target Inertial Parameters

by

Nicholas A. Hatch

A Dissertation  
Submitted to the Faculty  
of the  
WORCESTER POLYTECHNIC INSTITUTE  
in partial fulfillment of the requirements for the  
Degree of Doctorate of Philosophy  
in  
Electrical and Computer Engineering  
by



---

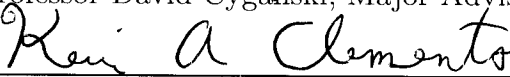
February 2006

APPROVED:



---

Professor David Cyganski, Major Advisor



---

Professor Kevin A. Clements



---

Professor Homer F. Walker

## Acknowledgements

This thesis would not have been possible without the encouragement I received from my advisor, Professor David Cyganski. He was always there to prod me along, and to challenge me to do my best. Our frequent tangents into completely unrelated topics provided a great supply of entertainment.

Many thanks to my patient and loving wife, Adrienne, who has been a great source of strength throughout this work. Also to my parents, who have supported me since the very beginning.

Thanks also to my labmates – David, Nick, and Ben for their friendship, encouragement and continuous comic relief. There was rarely a dull moment.

# Contents

<b>List of Figures</b>	<b>vi</b>
<b>List of Tables</b>	<b>ix</b>
Common Variables . . . . .	1
Common Abbreviations . . . . .	2
<b>1 Introduction</b>	<b>3</b>
1.1 Problem Statement and Goal of Thesis . . . . .	5
1.2 Contributions . . . . .	5
1.3 Organization . . . . .	6
<b>2 Background</b>	<b>7</b>
2.1 Sensors and Bandwidth . . . . .	7
2.2 The Radar Ranging Problem . . . . .	8
2.2.1 State Space Technique . . . . .	13
2.3 Target Isolation and Feature Tracking . . . . .	18
2.4 Coherence Errors . . . . .	21
2.5 Rigid Body Constraint . . . . .	21
2.5.1 Axial Symmetry . . . . .	24
2.6 Motion of a Force-Free Rigid Body . . . . .	25
2.6.1 Rigid Body Rotations & Geometry . . . . .	26
2.6.2 Precession, Nutation & Spin . . . . .	31
2.6.3 Integration of the Precession Function . . . . .	38
<b>3 Asymmetry Analysis</b>	<b>42</b>
3.1 Asymmetric Target . . . . .	42
3.2 Axially Symmetric Target . . . . .	47
3.3 Nearly Symmetric Target . . . . .	49
3.3.1 Precession $\phi(t)$ Model . . . . .	52
3.3.2 Nutation $\theta(t)$ Model . . . . .	56
3.3.3 Spin $\psi(t)$ Model . . . . .	57
3.4 Modulation Structure . . . . .	60
3.4.1 Axially Symmetric Target . . . . .	61

3.4.2	Nearly Symmetric Target . . . . .	67
3.5	Inertial Parameter Estimation . . . . .	96
3.5.1	Intermediate Result: Parameter Elimination . . . . .	97
<b>4</b>	<b>Conclusions</b>	<b>100</b>
4.1	Future Work . . . . .	102
<b>A</b>	<b>Scatterer Frequency Dependence</b>	<b>103</b>
<b>B</b>	<b>Torque-Free Motion Examples</b>	<b>106</b>
B.1	Rotation . . . . .	107
B.2	Rotation Rate . . . . .	110
B.3	Scatterer Position . . . . .	113
B.4	Range versus Time . . . . .	117
<b>C</b>	<b>Scatterer Position Estimation</b>	<b>120</b>
C.1	Track Factorization Method . . . . .	120
C.1.1	Single Body . . . . .	120
C.1.2	Multiple Bodies . . . . .	124
C.2	Rate Constrained . . . . .	129
C.2.1	Planar Motion . . . . .	129
C.2.2	Spinning and Precessing Motion . . . . .	132
<b>D</b>	<b>Frequency Decomposition: <math>\sin(\theta(t))</math></b>	<b>138</b>
<b>E</b>	<b>Elliptic Modulus Estimation</b>	<b>141</b>
<b>F</b>	<b>Elimination: 3 Parameter Implicit Function</b>	<b>148</b>
	<b>Bibliography</b>	<b>150</b>

# List of Figures

1.1	Radar Interrogating a Target . . . . .	3
2.1	Target Coordinate system and Radar Line of Sight . . . . .	10
2.2	Radar Data and the FFT . . . . .	12
2.3	Comparing FFT and MSA results . . . . .	14
2.4	Isolation of Targets . . . . .	19
2.5	Example Target with many scattering features . . . . .	20
2.6	Tracked Features . . . . .	20
2.7	Truth Track compared with Estimated Track . . . . .	22
2.8	Synthetic RTI . . . . .	22
2.9	Synthetic RTI with Tracking Error . . . . .	23
2.10	Rigid Body with fixed Scatterers . . . . .	23
2.11	Precession, Nutation, and Spin . . . . .	28
2.12	Projection of Target . . . . .	30
2.13	Principle Moments of Inertia and Angular Velocities . . . . .	32
2.14	Derivation Flow . . . . .	34
2.15	Jacobi Elliptic Sinusoids . . . . .	36
2.16	Example Spin, nutation and precession . . . . .	41
2.17	Example Spin, nutation and precession rates . . . . .	41
3.1	Motion case transitions for various initial conditions . . . . .	44
3.2	Values of $k$ for $\bar{\omega} = [1, 1, 10]$ . . . . .	45
3.3	Values of $k$ for $\bar{\omega} = [1, 1, 5]$ . . . . .	46
3.4	Values of $k$ for $\bar{\omega} = [1, 1, 1]$ . . . . .	46
3.5	Error in $sn$ Model . . . . .	51
3.6	Error in $\mathbf{K}(k)$ model, $\tilde{\mathbf{K}}(k)$ . . . . .	52
3.7	$\mathbf{\Pi}$ : $n$ Values for Various Inertia . . . . .	53
3.8	Error in $\mathbf{\Pi}(u, n = -0.2, k = 0.5)$ for Various Order Approximations . . . . .	54
3.9	Values of $r$ for various $n$ and $k$ . . . . .	54
3.10	Error in $\mathbf{\Pi}(sn(u), n, k)$ model, $\tilde{\mathbf{\Pi}}((sn)(u), n, k)$ , for Various $n$ and $k$ . . . . .	55
3.11	Error in $\frac{1}{\mathbf{K}(k)}$ model . . . . .	57
3.12	Values of $c$ for various inertia . . . . .	59
3.13	Error in $\tan^{-1}$ model . . . . .	59

3.14	Example Spin, nutation and precession rates . . . . .	61
3.15	Example Spin, nutation and precession rates . . . . .	62
3.16	Modulation Example 1: Angular Frequency Spectrum . . . . .	66
3.17	Modulation Example 2: Angular Frequency Spectrum . . . . .	66
3.18	Angular Frequency Spectrum: All terms . . . . .	69
3.19	Bessel function of the first kind evaluated for various $n$ and $\beta$ . . . . .	73
3.20	Angular Frequency Spectrum: Linear Components Only . . . . .	75
3.21	Angular Frequency Spectrum: Precession periodic component, $r_m^{1,2,3}$ . . . . .	76
3.22	Angular Frequency Spectrum: Precession periodic component, $r_m^3$ . . . . .	78
3.23	Angular Frequency Spectrum: Precession periodic component, $r_m^{1,2}$ . . . . .	81
3.24	Angular Frequency Spectrum: Spin periodic component, $r_m^{1,2,4}$ . . . . .	82
3.25	Angular Frequency Spectrum: Spin periodic component, $r_m^4$ . . . . .	84
3.26	Angular Frequency Spectrum: Spin periodic component, $r_m^{1,2}$ . . . . .	86
3.27	Angular Frequency Spectrum: Nutation periodic component, $r_m^{2,3,4,5}$ . . . . .	87
3.28	Angular Frequency Spectrum: Nutation periodic component, $r_m^5$ . . . . .	89
3.29	Angular Frequency Spectrum: Nutation periodic component, $r_m^2$ . . . . .	91
3.30	Angular Frequency Spectrum: Nutation periodic component, $r_m^4$ . . . . .	93
3.31	Angular Frequency Spectrum: Nutation periodic component, $r_m^3$ . . . . .	94
3.32	Surface of Implicit Inertial Function . . . . .	98
3.33	Intersecting Surfaces of Implicit Inertial Function . . . . .	99
A.1	PSLI Algorithm Example . . . . .	105
B.1	Example 1: Spin, nutation and precession . . . . .	108
B.2	Example 2: Spin, nutation and precession . . . . .	108
B.3	Example 3: Spin, nutation and precession . . . . .	109
B.4	Example 4: Spin, nutation and precession . . . . .	109
B.5	Example 1: Spin, nutation and precession rates . . . . .	110
B.6	Example 2: Spin, nutation and precession rates . . . . .	111
B.7	Example 3: Spin, nutation and precession rates . . . . .	111
B.8	Example 4: Spin, nutation and precession rates . . . . .	112
B.9	Example 1: 3D Scatterer Positions . . . . .	114
B.10	Example 1: 3D Scatterer Positions (colored by time) . . . . .	114
B.11	Example 2: 3D Scatterer Positions . . . . .	115
B.12	Example 3: 3D Scatterer Positions . . . . .	115
B.13	Example 4: 3D Scatterer Positions . . . . .	116
B.14	Example 1: Range versus Time . . . . .	117
B.15	Example 2: Range versus Time . . . . .	118
B.16	Example 3: Range versus Time . . . . .	118
B.17	Example 4: Range versus Time . . . . .	119
C.1	RTI - 1 Body, 5 Scatterers . . . . .	123
C.2	Position Estimation - 1 Body, 5 Scatterers . . . . .	123
C.3	RTI - 3 Bodies, 12 Scatterers . . . . .	126
C.4	Q-Matrix . . . . .	126

C.5	Q-Matrix, Block Diagonalized . . . . .	127
C.6	RTI - Separated Bodies . . . . .	127
D.1	Angular Frequency Spectrum: $\sin(\theta(t))$ . . . . .	139
E.1	Angular Frequency Spectrum for various $k$ . . . . .	143
E.2	$K(k)$ versus $k$ . . . . .	144
E.3	$k$ Estimation Example . . . . .	145
E.4	Error in the estimation of $k$ : $ k - k_{est} $ . . . . .	146
E.5	Direction Cosine constraint . . . . .	147

# List of Tables

2.1	Radar Signal Characteristics . . . . .	8
2.2	Example Moments of Inertia: Axially Symmetric Cone and Cylinder . . . . .	25
2.3	Example Moments of Inertia: Cone ( $r = 0.25m$ ) . . . . .	25
2.4	Angular Velocities of Orthogonal Axis . . . . .	35
3.1	Rotation Terms . . . . .	68
3.2	Linear Component Angular Frequency Spectrum Contributions . . . . .	76
3.3	Precession Periodic Component Angular Frequency Spectrum Contributions . . . . .	80
3.4	Spin Periodic Component Angular Frequency Spectrum Contributions . . . . .	85
3.5	Nutation Periodic Component Angular Frequency Spectrum Contributions . . . . .	94
3.6	All Angular Frequency Spectrum Contributions . . . . .	95
3.7	Estimation of Inertial Parameters: Nonlinear Estimation Unknowns & Equations . . . . .	97
3.8	Example Parameters for Estimating Moments of Inertia: $\bar{I} = [150, 130, 10]$ . . . . .	98
A.1	GTD-predicted $\alpha$ for Various Features. . . . .	104
B.1	Motion Example - Initial Conditions: $\bar{I}, \bar{\omega}, t$ . . . . .	106
B.2	Motion Example - Parameters: $h, T, k, n, c, \omega_\psi, \omega_\phi$ . . . . .	107
C.1	Position Estimation Example . . . . .	124
C.2	Multi-body Identification Example . . . . .	128
C.3	Motion Decomposition: Unknown and known terms . . . . .	134
E.1	Parameters for $k$ Estimation Trials . . . . .	145



## Common Variables

Symbol	Definition
$c$	Speed of light
$t$	Time
$f$	Frequency
$C_x, C_y, C_z$	Direction Cosines
$\alpha_c, \beta_c, \gamma_c$	Cosine Angles
$m$	Scatterer Index
$x, y, z$	Scatterer Cartesian coordinates
$p$	Scatterer coordinates vector
$\mathcal{F}\{\}$	Fourier Transform
$r$	Range
$R_y, R_z$	Rotation matrices defined about axis $y, z$
$\gamma$	Complex reflection coefficient
$A$	Radar Cross Section
$I_x, I_y, I_z$	Moments of Inertia
$\bar{I}$	Moments of Inertia Vector containing $I_x, I_y, I_z$
$T$	Kinetic Energy
$h$	Total Angular Momentum
$\mathbf{K}()$	Complete Elliptic Integral of the First Kind
$\mathbf{F}()$	Incomplete Elliptic Integral of the First Kind
$\mathbf{\Pi}()$	Incomplete Elliptic Integral of the Third Kind
$\omega_x, \omega_y, \omega_z$	Angular Velocities
$\bar{\omega}$	Angular Velocities vector containing $\omega_x, \omega_y, \omega_z$
$\alpha, \beta, \gamma$	Angular Velocity scalars
$sn(), cn(), dn()$	Jacobi Elliptic Functions
$k$	Elliptic Modulus

## Common Abbreviations

Acronym	Definition
AM	Amplitude Modulation
ATR	Automatic Target Recognition
FM	Frequency Modulation
MSA	Modern Spectral Analysis
PRF	Pulse Repetition Frequency
PSLI	Parametric Scattering Law Identification
RCS	Radar Cross Section
RTI	Range-Time Intensity
SNR	Signal-to-Noise Ratio
STM	State Transition Matrix
SVD	Singular Value Decomposition

# Chapter 1

## Introduction

A Radar system interrogates a target with a Radio Frequency (RF) pulse of energy and receives a one-dimensional (1D) projection of a target's three-dimensional (3D) Electromagnetic (EM) Radar Cross Section (RCS). As time progresses, the Radar may collect hundreds to thousands of these 1D projections. One receives the data in the form of a complex reflection coefficient for each interrogation frequency and moment in time. The range to the scatterer, the interrogation frequency and various EM characteristics of the scatterer determine the value of this coefficient.

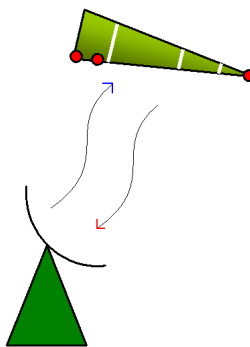


Figure 1.1: Radar Interrogating a Target: Red dots indicate locations of reflecting features

Given this backscattered energy returned by the target, our ultimate desire is to form a descriptive representation of the target. Due to the possible complexity of the situation, the RCS of the scattering features alone is often not enough to make critical decisions about the

identity of the target. We often wish to also discover shape and size information from the target's signature[11]. This representation is then used as a tool for further characterization and discrimination. These goals may be achieved by forming a one-dimensional (1D) range versus time intensity (RTI) plot, a two-dimensional (2) "Linear Image"[43, 49], or if possible a 2D or 3D "focused Image" to show scatterer locations ( $X, Y, Z$ ) in a target centered coordinate system[35]. Focused images are images that have been compensated for motion of the target or Radar platform over the duration of the RTI.

The motion of a feature on a target may be expressed as simple sinusoids for target rotation about one axis, or abstruse, non-sinusoidal and anharmonic functions for general free body target motion. The highly desirable focused images may only be formed with knowledge of this motion. Rudimentary methods currently exist to find this motion, but they allow for non-physical motions as solutions. One example of a non-physical motion would be a sudden change in orientation, but any motion requiring the action of a force or torque on the object is disallowed for the free body target. Even what appear to be correct motions, might truly be perturbed to some extent. This would cause undesirable blurring or obfuscation of the image created using the acquired direction cosines as line of sight values.

A motion estimation method with physics based constraints has the possibility of mitigating these issues by eliminating unwanted degrees of freedom in the estimation problem. Forcing the system to be that of a force-free rigid body would do this, limiting the resulting motion to a definable spin, nutation, and precession. Furthermore, using values from such a constrained method would allow for the estimation of additional motion parameters describing the target's shape to aid in more accurate characterization and discrimination.

## 1.1 Problem Statement and Goal of Thesis

Rigid body targets in exo-atmospheric free fall undergo motions defined by classical dynamics. Radar signatures provide a platform for estimation of various parameters relating to the motion and scattering characteristics of the target. This thesis provides a Radar based, physics constrained, estimator of the motion which generates these signatures. As part of this analysis, it defines a motion model for a “nearly” axially symmetric target in terms of its inertial parameters.

We show that the time-varying range to a point on the rigid body can be expressed in the form of an amplitude and frequency modulated signal. The frequency decomposition of this range function is used to estimate the target’s inertial parameters. This result has immediate application as a tool to assist the Radar analyst in further target characterization and constitutes an essential step to the full reconstruction of a target’s geometry from its signature.

## 1.2 Contributions

The following contributions to this field are made in this work:

1. The analytic integration of the time varying precession function, as it appears to not be readily available in the literature.
2. An analytic closed-form formulation of a point scatterer’s range path on an exo-atmospheric free falling asymmetric rigid body.
3. A formulation of the motion parameters in terms of inertial deviation from axial symmetry.
4. An amplitude and frequency modulation interpretation of the motion formulation.
5. A method for the estimation of inertial parameters.
6. A multi-body motion factorization extension to prior art based upon 2D image analysis technique.

## 1.3 Organization

Chapter 2 presents general information helpful for understanding the scope of the problem. It first introduces background pertaining to available sensors and the Radar ranging problem. It then covers problematic issues with collected data such as coherence errors and physical interference sources. Finally it introduces the mathematics for the rotation of a force-free rigid body and treats the transformation of a description of a rotating body to a description of what the Radar senses and collects as data. In particular, it covers the analytic formulation of the range function for a freely moving asymmetric body.

Chapter 3 explores how asymmetry and initial angular velocities affect a target's motion. It also shows what rotation simplifications occur when the target is axially symmetric and introduces rotation models for a "nearly" symmetric target. It then presents a harmonic decomposition analysis of the target's angular frequency spectrum and introduces a means of estimating inertial parameters of a nearly symmetric target.

Appendix A shows an extension to modern spectral analysis useful for tracking and categorizing reflecting features on a target. Appendix B contributes a collection of examples of rotations, rotation rates, three dimensional positions of features, and range versus time plots for various motions. Appendix C first reviews an alternative method for determining some motion parameters and introduces a technique for separating and sorting tracks from multiple bodies. It then acknowledges methods for finding discrete scatterer positions given angular velocity information and tracked scatterers.

## Chapter 2

# Background

In this chapter, the reader is provided a brief overview of the challenges one encounters when attempting to analyze a target scene. First, the concept of super-resolution methods are briefly introduced owing to their usefulness in many aspects of the Radar analysis problem. The issues of coherence and imaging are then presented, as a motivation for motion estimation. Finally, the foundation is laid for understanding the motion of a free falling target.

### 2.1 Sensors and Bandwidth

There are many types of Radar sensors that can be used for target discrimination. This section introduces two such sensor types that produce target data for which the analysis within this work may be applied. Implementations of these Radars both reside at the Reagan Test Site (RTS) in the Kwajalein Atoll, southwest of Hawaii.

The ARPA Lincoln C-Band Observables Radar (ALCOR) was constructed between 1968 and 1970. It supports both narrowband and wideband operating modes. The narrowband (NB) mode uses 6 MHz of bandwidth to acquire and track the target. Once acquired, it may switch to its wideband (WB) mode to collect signature data[1, 24, 7]. The wideband waveform with 512 MHz of bandwidth provides a range resolution of approximately 0.5 meters.

The Millimeter Wave Radar (MMW) is a dual frequency (Ka- and W-Band) monopulse

tracking Radar[3]. It has a signal bandwidth of up to 2 GHz yielding a range resolution of 0.014 meters. Operating at this bandwidth allows for a range window of 37.5 meters. At times when a larger window is needed, the bandwidth may be reduced to 1000 MHz or 500 MHz. This in turn allows for an proportional increase in the sampling rate.

Table 2.1: Radar Signal Characteristics.

	ALCOR	MMW
Band(s)	C	Ka, W
WB Bandwidth(s) (GHz)	0.5	0.5, 1, 2
PRF	38-323	50-2000
Pulse Width( $\mu sec$ )	10	50
Modulation	Linear FM Chirp	Linear FM Chirp

Various operating characteristics of these two Radars are summarized in Table 2.1. The high PRFs may supply a large number of target interrogations. These interrogations will capture the motion of the target as it moves over time.

## 2.2 The Radar Ranging Problem

When analyzing Radar data, one typically will use spectral analysis to identify the range and Radar Cross Section (RCS) of each scattering feature. It is apparent that the Radar ranging problem is equivalent to a spectral analysis problem when one decomposes the, frequency and time dependent, complex reflection coefficient. The complex reflection coefficient may be seen in Eq. 2.1. What is referred to here as RCS, the amplitude function, is sometimes instead referred to as the complex reflection coefficient. In this work the reflection coefficient shall include the range term as well.

$$\gamma(f, t) = \underbrace{A}_{RCS} e^{-j\frac{4\pi f}{c} \underbrace{r(t)}_{range}} \quad (2.1)$$

The RCS is a complex valued constant for each scattering center. A scattering center refers to the feature reflecting the signal. Its magnitude is an indication of the strength of



the returned RF signal for the particular time at which the target was interrogated with a given frequency and likewise its phase expresses any phase shift experienced during the reflection process.

One can further expand the model to show the construction of the time varying range function  $r(t)$  from object feature coordinates with respect to a body fixed (usually target centered) coordinate system and the view parameters connecting the canonical object description with a particular orientation with respect to the Radar sensor.

The viewpoint may be represented as corresponding time-varying direction cosines with respect to the line of sight vector that describe rotations of the target. The final range function is obtained upon projection onto the line of sight vector. A list of direction cosines represents a three element unit length vector pointing to a cartesian coordinate on the unit sphere[47]. As shown in Eq. 2.2 through Eq. 2.4, each element of this vector may be written in terms of cosines of angles from the three orthogonal axes to the line of sight vector.

$$C_x = \cos(\alpha_c) \quad (2.2)$$

$$C_y = \cos(\beta_c) \quad (2.3)$$

$$C_z = \cos(\gamma_c) \quad (2.4)$$

Fig. 2.1 depicts the body fixed target coordinate system in relation to the Radar's line of sight and the corresponding direction cosines that arise in this representation.

The direction cosines change as functions of time as the target rotates. Eq. 2.5 defines  $C_{xyz}$  as a symbolic representation of this vector.

$$C_{xyz} = \begin{bmatrix} C_x(t) & C_y(t) & C_z(t) \end{bmatrix} \quad (2.5)$$

A point,  $p$ , in the target fixed coordinate system has a three dimensional position as determined by coordinates  $x$ ,  $y$ , and  $z$ .

$$p = \begin{bmatrix} x \\ y \\ z \end{bmatrix} \quad (2.6)$$

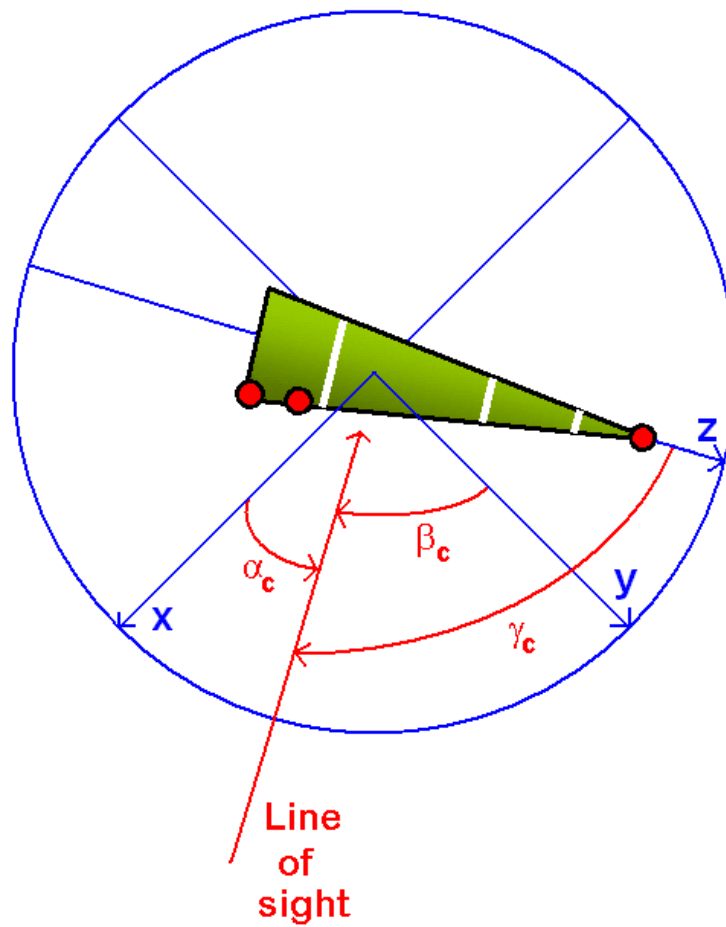


Figure 2.1: Scatterers positions are set in a target centered coordinate system. The direction cosine representing the line of sight is relative to this coordinate system. The direction cosines are the cosines of the angles  $\alpha_c$ ,  $\beta_c$ , and  $\gamma_c$ . These angles are between the axes  $x$ ,  $y$ , and  $z$  respectively and the line of size vector.

The dot product of the direction cosine vector  $C_{xyz}$ , and the position of the point  $p$  on the target as seen in Eq. 2.7, is the operation which forms the 1D range found in Eq. 2.8.

$$r(t) = \begin{bmatrix} C_x(t) & C_y(t) & C_z(t) \end{bmatrix} \begin{bmatrix} x \\ y \\ z \end{bmatrix} \quad (2.7)$$

$$\gamma(f, t) = \underbrace{A}_{RCS} e^{-j\frac{4\pi f}{c}} \underbrace{[C_x(t)x + C_y(t)y + C_z(t)z]}_{range} \quad (2.8)$$

Multiple scattering centers will be represented via the index  $m$  applied to each scatterer's location and RCS as seen in Eq. 2.9 which represents the complete reflection coefficient of a target. The complex coefficient may be conveniently represented as in Eq. 2.10 where certain functional dependencies have been suppressed.

$$\gamma(f, t) = \sum_m A_m e^{-j\frac{4\pi f}{c} [C_x(t)x_m + C_y(t)y_m + C_z(t)z_m]} \quad (2.9)$$

$$\gamma(f) = \sum_m A_m e^{-j\frac{4\pi f}{c} r_m} \quad (2.10)$$

Spectral analysis may be used to find the range and RCS of each scatterer on the target from the collected data. This can be shown using a Fourier Transform pair[35]. First, the factor of two due to the round trip range can be separated from the  $4\pi$  as seen in Eq. 2.11.

$$\gamma(f) = \sum_m A_m e^{-j2\pi\frac{2f}{c} r_m} \quad (2.11)$$

Then, the factor involving frequency and speed of light can be replaced with a constant  $k$ .

$$k = \frac{2f}{c} \quad (2.12)$$

$$\gamma(k) = \sum_m A_m e^{-j2\pi k r_m} \quad (2.13)$$

A transform pair exists for  $\gamma(k)$ , showing that range to the  $m^{th}$  scatterer can be represented by a zero width pulse of amplitude  $A_m$ .

$$\mathcal{F}^{-1}\{\gamma(k)\} = \gamma(r) \quad (2.14)$$

$$\gamma(r) = \sum_m A_m \delta(r - r_m) \quad (2.15)$$

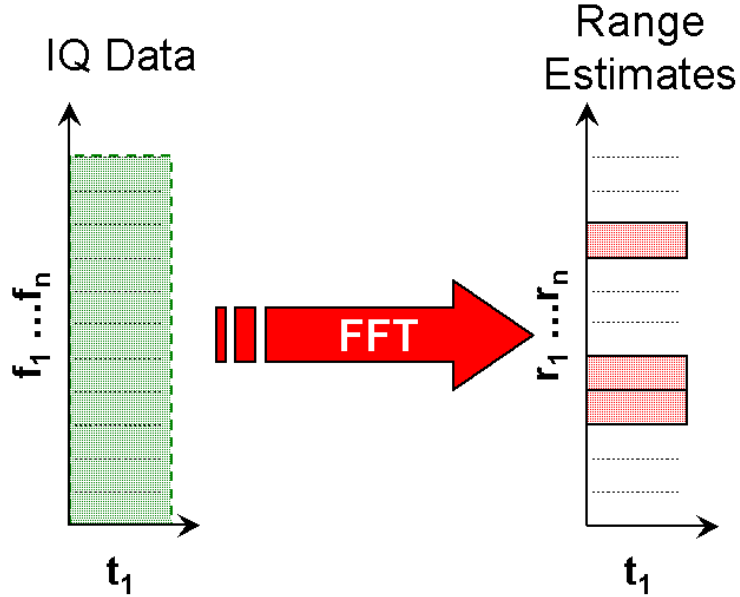


Figure 2.2: Radar Data and the FFT : Frequency samples collected about time instant  $t_1$  are transformed using the FFT into discrete range bins, where red bins indicate features scattering within given ranges

Spectral analysis, for the purpose of Radar Imaging, is traditionally performed using the Fast Fourier Transform (FFT). Fig. 2.2 depicts an example of applying the FFT to data collected for a target with three scattering centers to form discrete range values for the data collected in a single pulse centered at time  $t_1$  to yield one time-slice of an RTI. This method is appropriate when speed is required, as great attention has been spent on this algorithm to achieve that end. Unfortunately, its range resolution is limited to a predetermined bin size, and “spectral leakage” occurs when a scattering center is not centered in one Fourier bin.

There are other spectral analysis methods classified as Modern Spectral Analysis (MSA), or super-resolution methods, that offer benefits which are unattainable when using classical spectral analysis techniques such as the FFT. Some of these methods support super-resolution estimation of range, phase, and frequency dependencies of each scatterer[19, 40]. The tractability of the exponential model estimation problem was determined by Golub and Pereyra[16], who identified a general form of problems known as separable nonlinear least squares of which MSA is a special case. This allows the problem to be separated into

nonlinear estimation in a few parameters, followed by linear estimation of those remaining.

Precise knowledge of these scattering properties aid in multidimensional constructions, tracking, and overall discrimination. A comparison of the outcomes of applying Fourier processing and a particular MSA algorithm may be seen in Fig. 2.3. The Fourier results are seen on the left side of the figure whereas the MSA results on seen on the right. This figure shows RTI plots in which the time coordinate has been converted into the underlying angular coordinates relating to the object's aspect angle with respect to the Radar line of sight vector. The side-lobes in the Fourier plot hide the true scattering ranges, whereas the MSA plot displays highly resolved scattering center ranges.

### 2.2.1 State Space Technique

A particular form of range estimation that is used throughout this work is based upon mathematics that was developed in the context of linear control theory[29]. Referred to as a state-space technique, it is relatively concise to describe and produces the super-resolved range estimates. This section will briefly describe the state space processing of the collected data to obtain the ranges to each discrete scattering center. The  $n$  complex reflection coefficients shall be represented as  $\gamma_i$ , where  $i = 1..n$ .

$$\gamma_i = \gamma(f_i, t) \quad (2.16)$$

They represent data collected using interrogation frequencies  $f_i$ .

$$f_i = f_1 + (i - 1) \cdot \Delta f \quad (2.17)$$

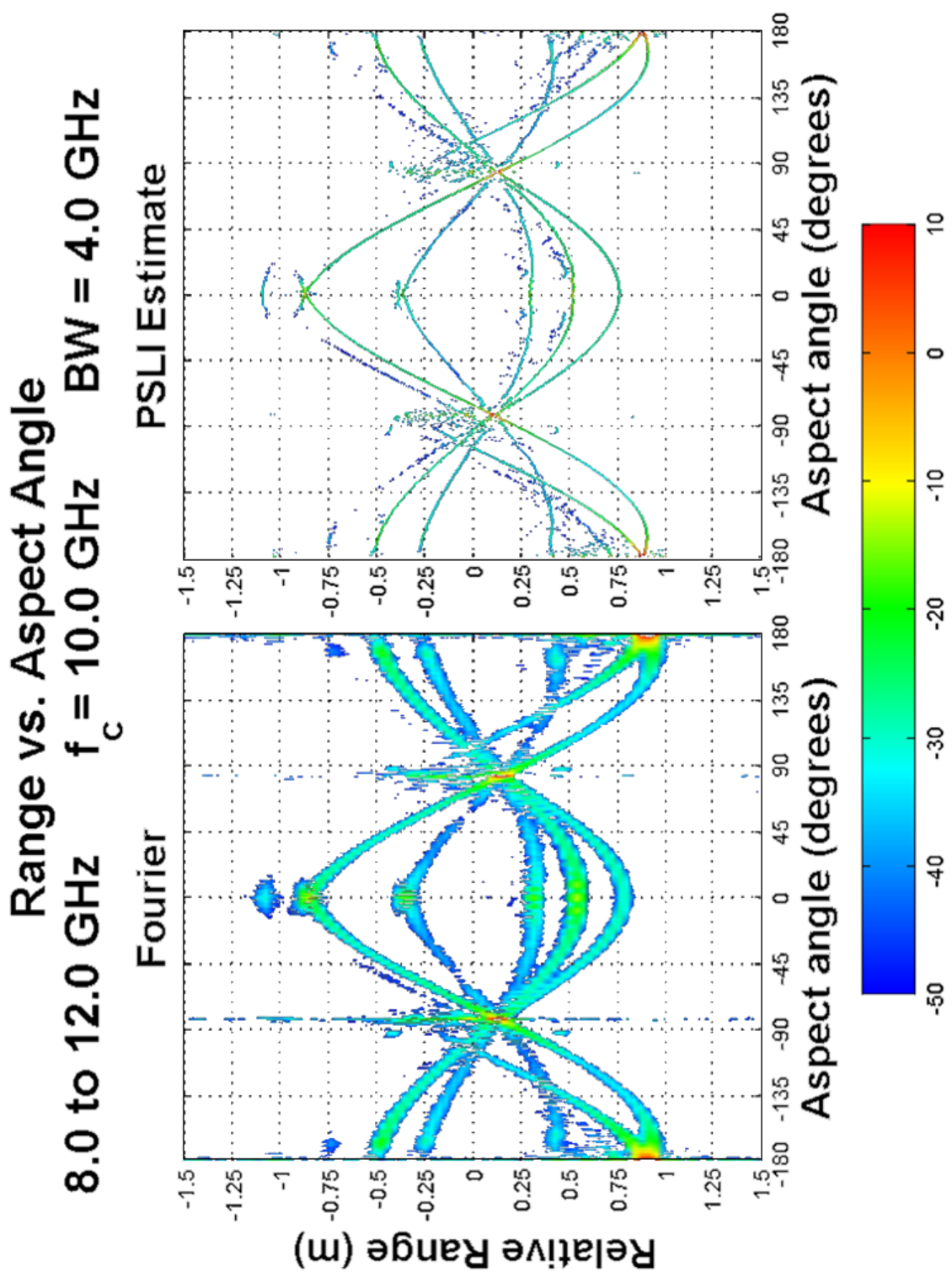


Figure 2.3: Example RTI plots comparing Fourier Analysis and Modern Spectral Analysis outcomes. Fourier Result on the left shows significant blurring as compared to MSA result on the right. Color indicates scattering intensity in dB. Each aspect angle is processed independently to find the scatterer ranges.

For convenience, we will use  $F$  to denote a vector composed of  $f_i \forall i \in (1, n)$ , and  $\Gamma$  for the vector composed of  $\gamma_i \forall i \in (1, n)$ .

$$F = \begin{bmatrix} f_1 \\ \vdots \\ f_n \end{bmatrix} \quad (2.18)$$

$$\Gamma = \begin{bmatrix} \gamma_1 \\ \vdots \\ \gamma_n \end{bmatrix} \quad (2.19)$$

The state-space estimator algorithm first forms the collected reflection coefficients,  $\gamma_i$ , into a rectangular Hankel  $a \times b$  matrix,  $H$ , as shown in Eq. 2.20.

$$H = \begin{bmatrix} \gamma_1 & \gamma_2 & \cdots & \gamma_b \\ \gamma_2 & \gamma_3 & & \gamma_{b+1} \\ \vdots & & \ddots & \vdots \\ \gamma_a & \gamma_{a+1} & \cdots & \gamma_{a+b-1} \end{bmatrix} \quad (2.20)$$

The rank  $N$  of this data matrix in the noiseless case is the number of signals, that is, the number of scatterers, in the system. The rank of the system may be determined by analyzing the singular-value spectrum of  $H$ [15]. As seen in Eq. 2.22, the diagonal elements of  $\Sigma$  represent this spectrum.

If there is an estimate of the SNR for the overall Radar signal, one may find  $N$  by

counting the number of singular values  $\sigma$  that lie above the SNR threshold.

$$svd\{H\} = U\Sigma V^H \quad (2.21)$$

$$= U \begin{bmatrix} \sigma_1 & 0 & 0 & 0 & 0 & 0 \\ 0 & \sigma_2 & 0 & 0 & 0 & 0 \\ 0 & 0 & \ddots & 0 & 0 & 0 \\ 0 & 0 & 0 & \sigma_j & 0 & 0 \\ 0 & 0 & 0 & 0 & 0 & 0 \\ 0 & 0 & 0 & 0 & 0 & 0 \end{bmatrix} V^H \quad (2.22)$$

The approach of the state space method is to find a State Transition Matrix (STM) that underlies the evolution of a linear state space model, for progressive interrogation frequencies, of the received signal. The modal matrix of this STM will directly describe the ranges of interest. Using this algorithm, we have a choice between two options for computing the STM. The first option is referred to as the Observability approach. The second option is referred to as the Controllability approach. The difference between these two options is that the first approach uses the Hankel matrix range space to compute the STM, while the second approach uses the null space. They provide similar results, and as such, either may be used.

For the following section, a shorthand notation of  $a : b$  will be used to signify the  $a^{th}$  row or column of a matrix to the  $b^{th}$  row or column following the MATLAB matrix processing language's method of designating submatrices. A colon without an  $a$  or  $b$  implies the selection of all rows or columns. For example,  $\zeta(1 : 3, :)$  selects the submatrix containing the first three rows of  $\zeta$ .

- Option 1: Observability Approach

1. Form the observability matrix,  $\mathcal{O}$ , from the  $U$  and  $\Sigma$  matrices obtained with the SVD.

$$\mathcal{O} = U(:, 1 : N) \cdot \sqrt{\Sigma}(1 : N, 1 : N) \quad (2.23)$$



2. Form  $\mathcal{O}_+$  and  $\mathcal{O}_-$  from  $\mathcal{O}$  by deleting the first and last row, respectively.

$$\mathcal{O}_+ = \mathcal{O}(2 : N, :) \quad (2.24)$$

$$\mathcal{O}_- = \mathcal{O}(1 : N - 1, :) \quad (2.25)$$

3. Create the STM from the product of the  $\mathcal{O}_-$  pseudo-inverse and  $\mathcal{O}_+$ .

$$STM = \mathcal{O}_-^\dagger \cdot \mathcal{O}_+ \quad (2.26)$$

- Option 2: Controllability Approach

1. Form the controllability matrix,  $\mathcal{C}$ , from the  $\Sigma$  and  $V$  matrices from the SVD.

$$\mathcal{C} = \sqrt{\Sigma}(1 : N, 1 : N) \cdot V(:, 1 : N)^H \quad (2.27)$$

2. Form  $\mathcal{C}_+$  and  $\mathcal{C}_-$  from  $\mathcal{C}$  by deleting the first and last columns, respectively.

$$\mathcal{C}_+ = \mathcal{C}(:, 2 : N) \quad (2.28)$$

$$\mathcal{C}_- = \mathcal{C}(:, 1 : N - 1) \quad (2.29)$$

3. Create the STM from the product of  $\mathcal{C}_+$  and the  $\mathcal{C}_-$  pseudo-inverse.

$$STM = \mathcal{C}_+ \cdot \mathcal{C}_-^\dagger \quad (2.30)$$

We may then use an eigenvalue decomposition[17] to find the state transition matrix complex eigenvalues,  $\lambda_i$ , and then multiply the polar angle of these eigenvalues,  $\angle\lambda_i$  in Eq. 2.32, with the scale factor  $k_s$  given in Eq. 2.31 to produce the range in meters to each scatterer.

$$k_s = -\frac{c}{4\pi \cdot \Delta f} \quad (2.31)$$

$$x(i) = k_s \cdot \angle\lambda_i \quad (2.32)$$

The complex amplitudes associated with each scatterer may then be found with little more computation by performing a least squares match of the model, now with known

eigenvalues, to the collected reflection coefficients. The row vector  $L$  contains the polar angles of the eigenvalues.

$$L = \begin{bmatrix} \angle\lambda_1 & \angle\lambda_2 & \dots & \angle\lambda_n \end{bmatrix} \quad (2.33)$$

The complex amplitude vector  $A$  is desired. It contains the RCS of each scatterer

$$A = \begin{bmatrix} A_1 \\ A_2 \\ \vdots \\ A_n \end{bmatrix} \quad (2.34)$$

A matrix decomposition of the reflection coefficients in terms of the eigenvalues may be seen in Eq. 3.124. The eigenvalue angles,  $L$ , and the frequencies,  $F$ , when fitted in a least squares sense to the reflection coefficients,  $\Gamma$ , produce the vector,  $A$ . This result is shown in Eq. 3.125.

$$\Gamma = e^{j\left(\frac{F}{\Delta F}L\right)} A \quad (2.35)$$

$$A = \left[ e^{j\left(\frac{F}{\Delta F}L\right)} \right]^\dagger \Gamma \quad (2.36)$$

If the magnitude of the RCS has a frequency dependence, an extended formulation may be used to acquire additional information regarding this dependence. Such a formulation is briefly explored in Appendix A.

## 2.3 Target Isolation and Feature Tracking

Two important uses of super-resolution methods shall now be briefly reviewed. The collected data may contain artifacts or other undesirable objects within the range window. This unwanted data can present itself in either of two significant forms. The simplest case to manage is that in which the artifacts are at ranges which do not interfere or cross over the object of interest. In this case, they may easily be selected and removed from the data.

The more difficult case, when the two objects cross at a series of ranges, as seen in Fig. 2.4, is specifically well suited to super-resolution methods. When isolating a target with Fourier methods, one may get as close as a single range bin, whereas a super-resolution method allows for sub-range gate resolution, thus allowing a closer and cleaner isolation[4]. If the analyst cannot determine if there is more than one object, but is able to track the scatterers, it is possible to form a matrix decomposition problem which can identify tracks undergoing different motions. Details of this novel algorithm developed during this research effort may be found in Appendix C.1.

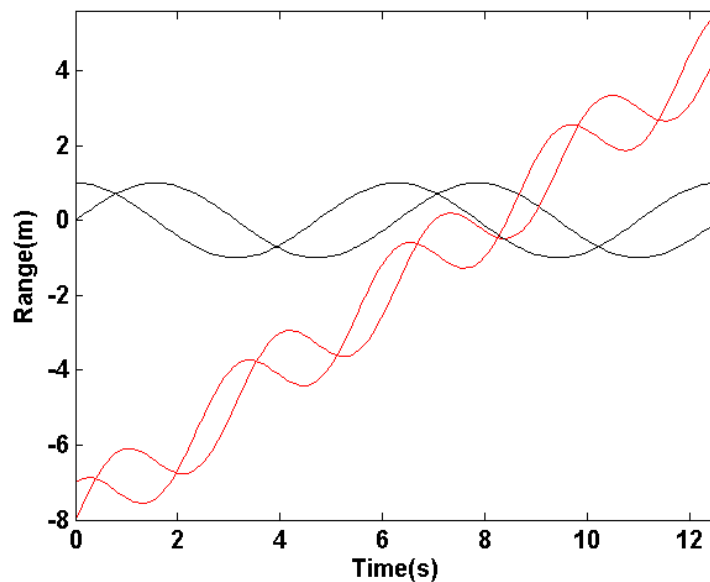


Figure 2.4: Isolation of Targets: The scene contains two targets, one red, one black. The targets cross at approximately 8 seconds causing signal interaction.

Another useful attribute of these methods is that each scattering center is represented as a single discrete range with an associated RCS, as opposed to an RCS value associated with a fixed range bin. This makes it easier to track, or tag, a scatterer using either an automated[5] or analyst assisted tracker. An example of scatterer tracking may be seen in Fig. 2.5 and Fig. 2.6. Fig. 2.5 displays a complex target with many scattering centers. After tracking selected features, untracked scatterers may be removed. Fig. 2.6 shows the tracked scatterers color coded by feature number.

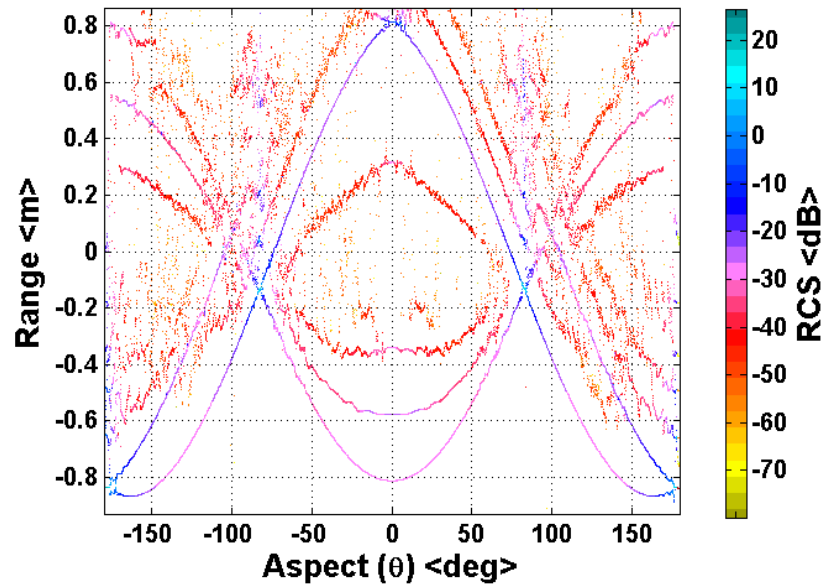


Figure 2.5: Example Target with many scattering features

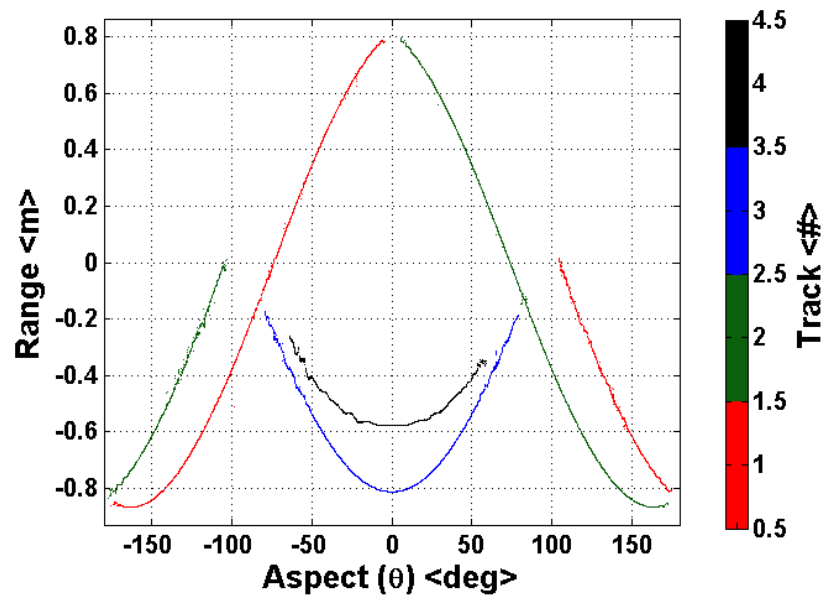


Figure 2.6: Four scatterers have been tracked and colored by feature: The nose tip (Blue), the leading base edge (Green), the trailing base edge (Red), and a groove (black). All other scatterers have been removed

## 2.4 Coherence Errors

There are two errors commonly referred to as “coherence” errors. The first error is related to the range. All of the scatterers found within a return may have a single range offset,  $\epsilon_r$ , which is a random variable with respect to the interrogation index.

The second error is in phase. A phase offset,  $\epsilon_\phi$ , may be shared for all scatterers which is again a random variable with respect to the interrogation index.

$$\gamma(f) = A(f)e^{-j\frac{4\pi f}{c}[r+\epsilon_r]}e^{j\epsilon_\phi} \quad (2.37)$$

One primary cause of range offsets,  $\epsilon_r$ , may be attributed to “tracker” error. A tracker in this case refers to the signal processing algorithm which keeps the target within the range window of the Radar. An example of tracking error may be seen in Fig. 2.7. Fig. 2.8 shows an example of an RTI for three scatterers rotating on a rigid body. The effects of the range offsets seen in Fig. 2.7 when applied to the data in Fig. 2.8 may be seen in Fig. 2.9. A tracker may attempt to follow a single dominant scatterer. The problem is that a scatterer is not necessarily fixed to any single point on the target. This is because the scatterer reflectivity is a function of interrogation angle and some scatterers have no apparent motion as the target rotates. Range offsets hinder scatterer tracking and obfuscate target rotations.

Phase offsets,  $\epsilon_\phi$ , may be attributed to the Radar system’s internal clock errors as well as atmospheric propagation delays. There are a few common phase correction methods [48]. They involve tracking phase evolution of the strongest scatterers, averaging over all range bins, or sub-image analysis. This work, in its current state, does not handle unaligned range estimates.

## 2.5 Rigid Body Constraint

In the following discussion, the scatterers of interest in the target scene are considered to be fixed to a rigid body. An example asymmetric body with diagrammatically indicated scatterers may be seen in Fig. 2.10. All points on the body undergo the same motion relative to a fixed point. This fixed point is defined as the Center of Gravity (CG). A rigid body is assumed to never change size or shape[44]. The visible contribution of this assumption

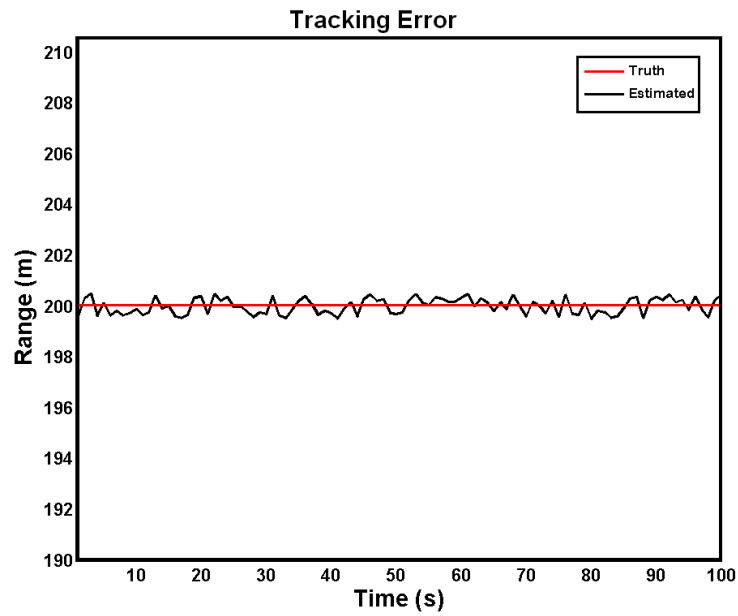


Figure 2.7: Truth Track (Red) compared with Estimated Track (Black): Error in estimation given difficulties with tracker

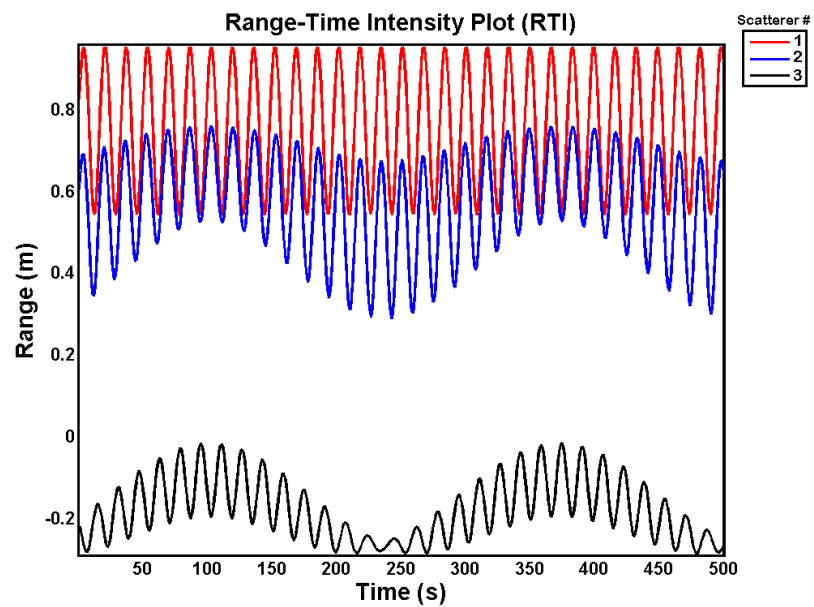


Figure 2.8: Synthetic RTI containing 3 scatterers. Periodic behavior is apparent. Color indicates feature number.

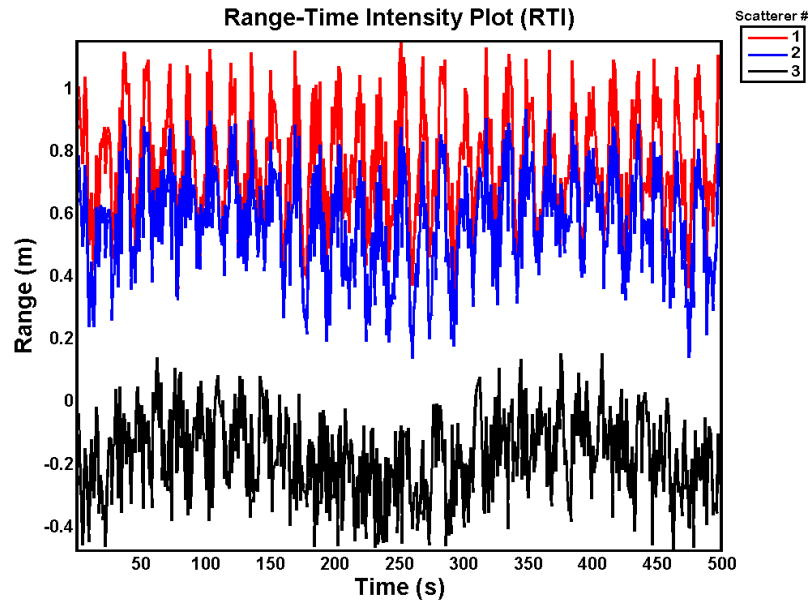


Figure 2.9: Synthetic RTI with tracking error applied. Periodic behavior is disguised. Color indicates feature number.

is that the relative distance from one point on the body to any other point will remain constant[25].

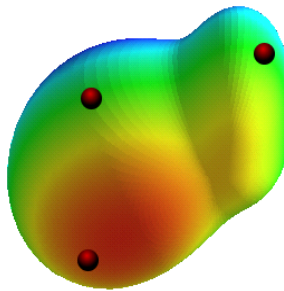


Figure 2.10: Rigid Body with fixed Scatterers: The shape of the target can be arbitrary

A point-mass  $m$  located at distance  $r$  from the axis of rotation has a resistance to rotational acceleration, or inertia, computed as the product of the mass and the distance squared, as seen in Eq. 2.38.

$$I = mr^2 \quad (2.38)$$

A rigid body may be viewed as a collection of infinitesimal masses  $dm$ , or a continuous mass distribution contained within a volume. The principle moments of inertia can thus be represented in terms of a volume integral of the distance  $r$  and the spatial density distribution  $\rho$  about three orthogonal axes in the cartesian coordinate system centered at the target's center of gravity. as seen in equations 2.39, 2.40, and 2.41.

$$I_x = \int (y^2 + z^2)\rho(x, y, z)dV \quad (2.39)$$

$$I_y = \int (x^2 + z^2)\rho(x, y, z)dV \quad (2.40)$$

$$I_z = \int (x^2 + y^2)\rho(x, y, z)dV \quad (2.41)$$

The inertia  $\bar{I}$ , seen in Eq. 2.42, is a symbolic representation of the principle moments of inertia,  $I_x, I_y, I_z$ .

$$\bar{I} = \begin{bmatrix} I_x & I_y & I_z \end{bmatrix} \quad (2.42)$$

For the purpose of the analysis, the relationship between the moments is defined as seen in Eq. 2.43. The target coordinate system can always be rotated, and axis designated, such that this expression is true.

$$I_x \geq I_y \geq I_z \quad (2.43)$$

The moments of inertia serve as the principle description of the parameters of a rigid body with respect to the description essential to dynamics of rotational motion.

### 2.5.1 Axial Symmetry

A special case arises when the first two moments are equivalent, as seen in Eq. 2.44. It is referred to as axial symmetry about the  $z$  - *axis*. It will be shown in Chapter 3 that this special case greatly simplifies the motion equations.

$$I_x = I_y \geq I_z \quad (2.44)$$

Table 2.2 presents inertia expressions[21] of some simple symmetric objects. In these equations  $m$ ,  $r$ , and  $h$  correspond to mass, radius and height respectively. All rotations are



assumed to be about the object’s CG. Table 2.3 presents example inertia values for a cone having a radius of 0.25 meters for various combinations of height and mass. An appreciation for the typical sizes of these values as shown in their table for dimensions and masses of objects that may be encountered as targets will prove useful for our later discussions.

Table 2.2: Example Moments of Inertia: Axially Symmetric Cone and Cylinder

	$I_x, I_y$	$I_z$
Cone	$\frac{1}{10}mh^2 + \frac{3}{20}mr^2$	$\frac{3}{10}mr^2$
Cylinder	$\frac{1}{12}mh^2 + \frac{1}{4}mr^2$	$\frac{1}{2}mr^2$

Table 2.3: Example Moments of Inertia. Each example uses a cone base radius of  $r = 0.25m$ .

Mass (kg)	Height (m)	$I_x, I_y$	$I_z$
100	1	10.9	1.9
250	1	27.4	4.7
500	1	54.7	9.4
100	1.5	23.5	1.9
250	1.5	58.6	4.7
500	1.5	117.2	9.4

## 2.6 Motion of a Force-Free Rigid Body

Without restrictions on allowable target motions, there may not be a way to achieve robust motion estimation or range offset correction. There are realistic assumptions we can apply to the specific case of a target in exo-atmospheric free fall. We assert two primary conditions. First, the target is a rigid body. This allows the application of a kinematic constraint that has been previously found useful to form target representations. Second, there are no external forces or torques acting upon the rigid body. This presents a previously unassumed dynamic constraint, which will allow a complete representation of the feature locations and their respective rotational motions.

These assertions dictate that the rotational motions are determined by classical dynamics of free bodies. Both Goldstein [14] and Wells [50] present some material helpful for understanding the variables in the “rigid body” motion problem. As it will be seen, the complete equations of motion for an asymmetric rigid target involve “Special Functions” in their solution, complicating the solution expressions [41].

### 2.6.1 Rigid Body Rotations & Geometry

An RTI is ideally a projection of the trajectory of a point on the target as it undergoes free body motion about its center of mass. The various rotations that apply to the target are now explored and then related to the target’s inertia, kinetic energy, and angular momentum.

First, we define the location of the  $m^{th}$  point scatterer, as seen in Eq. 2.45, located in a cartesian coordinate system fixed to the rigid body.

$$p_m = \begin{bmatrix} x_m \\ y_m \\ z_m \end{bmatrix} \quad (2.45)$$

An Euler Angle rotation scheme is used in this thesis[42]. We may define rotations about orthogonal axes y and z as seen in Eq. 2.46 and Eq. 2.47 which will be applied to the point scatterer.

$$R_y\{\varphi\} \triangleq \begin{bmatrix} \cos(\varphi) & 0 & -\sin(\varphi) \\ 0 & 1 & 0 \\ \sin(\varphi) & 0 & \cos(\varphi) \end{bmatrix} \quad (2.46)$$

$$R_z\{\varphi\} \triangleq \begin{bmatrix} \cos(\varphi) & \sin(\varphi) & 0 \\ -\sin(\varphi) & \cos(\varphi) & 0 \\ 0 & 0 & 1 \end{bmatrix} \quad (2.47)$$

As depicted in Fig. 2.11, the target's location at any given time may be decomposed into a spinning, nutating, and precessing motion completely described in terms of the rotations in Eq. 2.46 and Eq. 2.47. These rotations, coupled with a line of sight vector, will allow formation of the 1D projection of the scatterer's range path. The motion of the target within its own coordinate space may be represented by a series of rotations as seen in Eq. 2.48. This series of rotations is one of many possible choices. Conversions between this Euler rotations scheme ( $Z - Y - Z$ ) and various others ( $Z - X - Z$ ,  $X - Y - Z$ , etc.) may be found in [38].

$$R_T(t) = \underbrace{R_z\{-\phi(t)\}}_{\text{Precession}} \underbrace{R_y\{-\theta(t)\}}_{\text{Nutation}} \underbrace{R_z\{-\psi(t)\}}_{\text{Spin}} \quad (2.48)$$

All possible rigid body positions may be achieved with the rotations constrained as in Eq. 2.49 through Eq. 2.51[44].

$$0 \leq \psi \leq 2\pi \quad (2.49)$$

$$0 \leq \theta \leq \pi \quad (2.50)$$

$$0 \leq \phi \leq 2\pi \quad (2.51)$$

In this thesis, both  $\cos$  and  $\sin$  may be represented in condensed form as  $c$  and  $s$  respectively, as shown in Eq. 2.52 and Eq. 2.53.

$$c_x = \cos(x) \quad (2.52)$$

$$s_x = \sin(x) \quad (2.53)$$

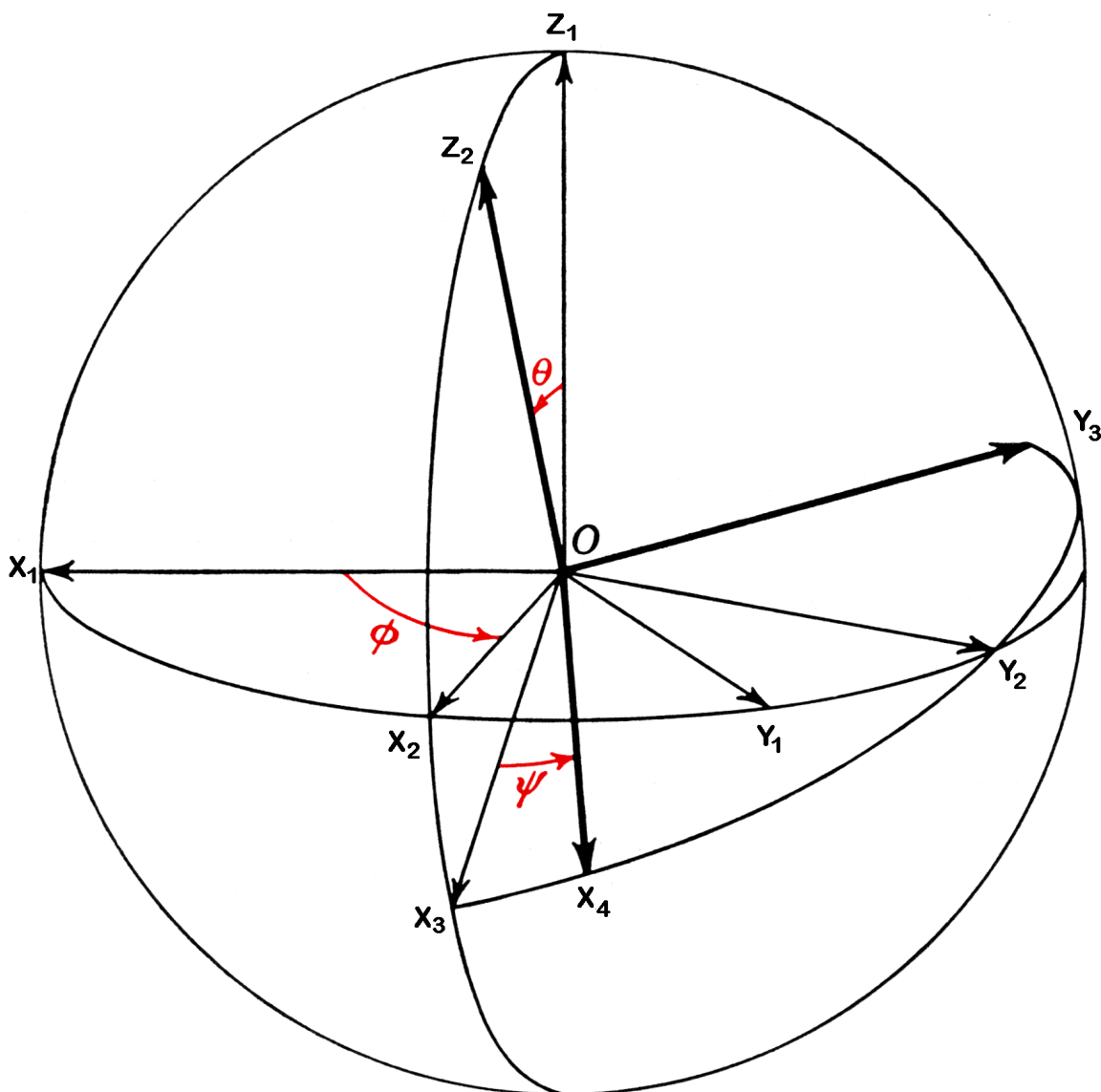


Figure 2.11: Precession, Nutation, and Spin: The scatterers on the target begin aligned to a coordinate frame of  $(x_1, y_1, z_1)$ . They then precess to  $(x_2, y_2, z_1)$ , nutate to  $(x_3, y_2, z_2)$ , and finally spin to  $(x_4, y_3, z_2)$ [44].

The complete spin, nutation, and precession rotation matrix may be seen in Eq. 2.54.

$$R_T(t) = \begin{bmatrix} c_\phi c_\theta c_\psi - s_\phi s_\psi & -c_\phi c_\theta s_\psi - s_\phi c_\psi & c_\phi s_\theta \\ s_\phi c_\theta c_\psi + c_\phi s_\psi & -s_\phi c_\theta s_\psi + c_\phi c_\psi & s_\phi s_\theta \\ -s_\theta c_\psi & s_\theta s_\psi & c_\theta \end{bmatrix} \quad (2.54)$$

The motion of the  $m^{th}$  point on the target at each moment in time is found forming the series of products between the motion matrix  $R_T$  and the points initial location  $p_m$ , shown in Eq. 2.55.

$$p_m(t) = R_T(t)p_m \quad (2.55)$$

Eq. 2.55 may be seen in full matrix form in Eq. 2.56. The matrix product is then computed and shown in Eq. 2.56. It presents a complete descriptor of a point scatterers position in a target-fixed coordinate system at each moment in time.

$$\begin{aligned} p_m(t) &= \begin{bmatrix} c_\phi c_\theta c_\psi - s_\phi s_\psi & -c_\phi c_\theta s_\psi - s_\phi c_\psi & c_\phi s_\theta \\ s_\phi c_\theta c_\psi + c_\phi s_\psi & -s_\phi c_\theta s_\psi + c_\phi c_\psi & s_\phi s_\theta \\ -s_\theta c_\psi & s_\theta s_\psi & c_\theta \end{bmatrix} \begin{bmatrix} x_m \\ y_m \\ z_m \end{bmatrix} \\ &= \begin{bmatrix} x_m(c_\phi c_\theta c_\psi - s_\phi s_\psi) + y_m(-c_\phi c_\theta s_\psi - s_\phi c_\psi) + z_m c_\phi s_\theta \\ x_m(s_\phi c_\theta c_\psi + c_\phi s_\psi) + y_m(-s_\phi c_\theta s_\psi + c_\phi c_\psi) + z_m s_\phi s_\theta \\ -x_m s_\theta c_\psi + y_m s_\theta s_\psi + z_m c_\theta \end{bmatrix} \quad (2.56) \end{aligned}$$

The data which the Radar observes is truly a 1D projection of this 3D motion with respect to an arbitrary axis determined by the Radar position with respect to the target, as seen in Fig. 2.12. As seen in this figure, the range to a particular scatterer is dependent upon the position of the target and the Radar line of sight. Different Radar positions produce different ranges for the same scatterers. It shows that for one position, the base scatterers are the closest, and for another position, they are the furthest away.

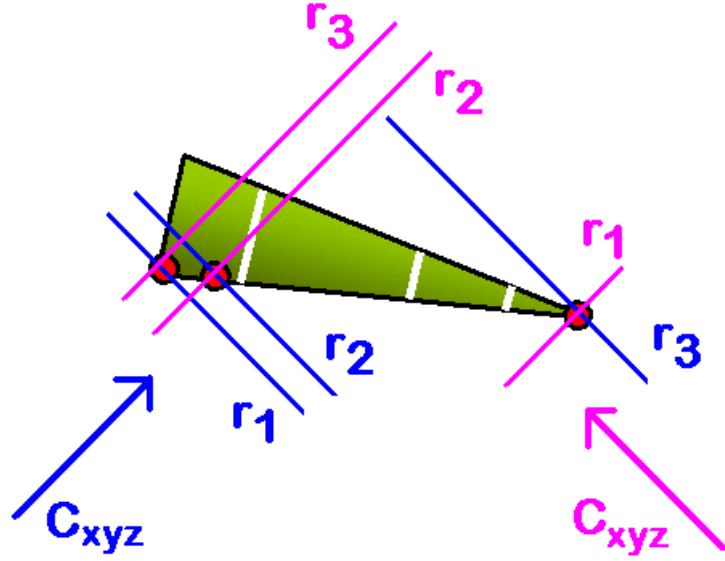


Figure 2.12: Projection of Target: The two rays labelled  $C_{xyz}$  represent Radars interrogating a target from two different line of sights. Each view resolves the same scatterers, but they appear at different ranges.

To achieve the projection we shall choose a direction cosine pointing towards the target down an arbitrary line of sight, as seen in Eq. 2.57. In the case of a moving Radar system or frame of reference,  $C_{xyz}$  may be a function of time.

$$r_m(t) = C_{xyz} \begin{bmatrix} x_m(c_\phi c_\theta c_\psi - s_\phi s_\psi) + y_m(-c_\phi c_\theta s_\psi - s_\phi c_\psi) + z_m c_\phi s_\theta \\ x_m(s_\phi c_\theta c_\psi + c_\phi s_\psi) + y_m(-s_\phi c_\theta s_\psi + c_\phi c_\psi) + z_m s_\phi s_\theta \\ -x_m s_\theta c_\psi + y_m s_\theta s_\psi + z_m c_\theta \end{bmatrix} \quad (2.57)$$

Evaluation of the matrix products in Eq. 2.57 produces Eq. 2.58.

$$\begin{aligned} r_m(t) = & C_x x_m c_\theta c_\psi c_\phi + C_y x_m c_\theta c_\psi s_\phi - C_z x_m c_\psi s_\theta - C_x x_m s_\psi s_\phi + C_y x_m s_\psi c_\phi \\ & - C_x y_m c_\theta s_\psi c_\phi - C_y y_m c_\theta s_\psi s_\phi + C_z y_m s_\theta s_\psi - C_x y_m c_\psi s_\phi + C_y y_m c_\psi c_\phi \\ & + C_x z_m s_\theta c_\phi + C_y z_m s_\theta s_\phi + C_z z_m c_\theta \end{aligned} \quad (2.58)$$

### 2.6.2 Precession, Nutation & Spin

Now, knowing the mathematics that describe's how the three rotations are applied to each scattering center, it is necessary to discuss the makeup of the rotation arguments.

Each time-dependent rotation function includes a constant,  $\kappa$ , accounting for initial conditions. These time functions are given in Eq. 2.59 through Eq. 2.61.

$$\phi(t) = f_\phi(t) + \kappa_\phi \quad (2.59)$$

$$\theta(t) = f_\theta(t) + \kappa_\theta \quad (2.60)$$

$$\psi(t) = f_\psi(t) + \kappa_\psi \quad (2.61)$$

Eq. 2.62 shows the  $m^{th}$  track in an RTI, or analytic range function, generated by the  $m^{th}$  scatterer composed of the original 3D scatterer locations, spin, nutation, precession, and the line of sight direction cosines related to the formation of the Radar's 1D projection.

$$r_m(t) = C_{xyz}^T R_z(-f_\phi(t) - \kappa_\phi) R_y(-f_\theta(t) - \kappa_\theta) R_z(-f_\psi(t) - \kappa_\psi) p_m \quad (2.62)$$

As seen in, Eq. 2.63, a rotation whose argument is the sum of two values may be equivalently represented as the product of rotations for each of those values. Furthermore, as seen in Eq. 2.64, rotations on the same axis by  $\varphi_a$  and  $\varphi_b$  commute.

$$R(\varphi_a + \varphi_b) = R(\varphi_a)R(\varphi_b) \quad (2.63)$$

$$= R(\varphi_b)R(\varphi_a) \quad (2.64)$$

Applying the property found in Eq. 2.63 to Eq. 2.62 produces Eq. 2.65.

$$r_m(t) = C_{xyz}^T R_z(-\kappa_\phi) R_z(-f_\phi(t)) R_y(-\kappa_\theta) R_y(-f_\theta(t)) R_z(-f_\psi(t)) R_z(-\kappa_\psi) p_m \quad (2.65)$$

The constant value  $\kappa_\psi$  is a time invariant rotation which we may take as operating to the left on the direction cosine vector  $C_{xyz}$ . Thus the two quantities may be grouped and viewed as a new Radar's line of sight. Similarly,  $\kappa_\phi$  is a time invariant rotation operating to the left on the initial scatterer positions  $p_m$ . So these quantities are grouped and viewed as a

rotation applied to the initial positions. Thus Eq. 2.66 will be reparameterized as shown in Eq. 2.67.

$$r_m(t) = \underbrace{C_{xyz}^T R_z(-\kappa_\phi)}_{C_{xyz}} R_z(-f_\phi(t)) R_y(-\kappa_\theta) R_y(f_\theta(t)) R_z(-f_\psi(t)) \underbrace{R_z(-\kappa_\psi)}_{p_m} p_m \quad (2.66)$$

$$= C_{xyz} R_z(-f_\phi(t)) R_y(-\kappa_\theta) R_y(f_\theta(t)) R_z(-f_\psi(t)) p_m \quad (2.67)$$

A rigid body's motion may be completely described given its principle moments of inertia and initial angular velocities. The case of an arbitrary asymmetric rigid body may be described using all three principle moments of inertia,  $\bar{I} = (I_x, I_y, I_z)$ , and three angular velocities,  $\bar{\omega} = (\omega_x, \omega_y, \omega_z)$  while an axially-symmetric rigid body is a simpler case. There are only two unique moments of inertia,  $I_x$  and  $I_z$  as  $I_y = I_x$ . The moments of inertia and the angular velocities are depicted in Fig. 2.13.

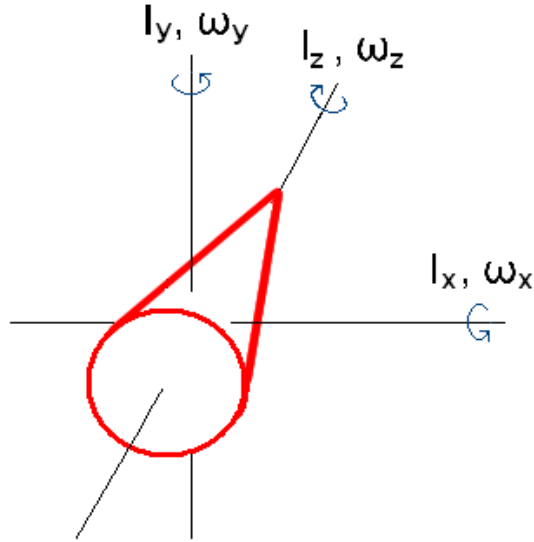


Figure 2.13: Principle Moments of inertia and angular velocities shown as vectors piercing an object through its center of gravity

The equations of motion for a rigid body are displayed in Eq. 2.68, Eq. 2.69, and Eq. 2.70. They involve the principle moments of inertia, the angular velocities, and the principle moments of all external forces,  $\bar{G} = (G_x, G_y, G_z)$ , about the center of gravity.



Fig. 2.14 depicts the major steps in the process of deriving the position of a point on a rigid body versus time. A summary of this process will now follow. Further details related to the origin of these equations may be found in Synge[44] and [13]. Information regarding effects of external perturbations or thrusts may be found in additional supporting documents[8, 46].

$$I_x \dot{\omega}_x(t) - (I_y - I_z) \omega_y(t) \omega_z(t) = G_x \quad (2.68)$$

$$I_y \dot{\omega}_y(t) - (I_z - I_x) \omega_z(t) \omega_x(t) = G_y \quad (2.69)$$

$$I_z \dot{\omega}_z(t) - (I_x - I_y) \omega_x(t) \omega_y(t) = G_z \quad (2.70)$$

Since the rigid body in our study is in free fall, external moments  $G_x, G_y$ , and  $G_z$  are all equal to zero. The integration of Eq. 2.71 through Eq. 2.73 may be found in Synge [pp.377 – 379].

$$I_x \dot{\omega}_x(t) - (I_y - I_z) \omega_y(t) \omega_z(t) = 0 \quad (2.71)$$

$$I_y \dot{\omega}_y(t) - (I_z - I_x) \omega_z(t) \omega_x(t) = 0 \quad (2.72)$$

$$I_z \dot{\omega}_z(t) - (I_x - I_y) \omega_x(t) \omega_y(t) = 0 \quad (2.73)$$

To simplify notation, the initial angular velocities may be defined as seen in Eq. 2.74 through Eq. 2.76. The initial angular velocities represent the body's angular velocity at time zero.

$$\omega_{ox} = \omega_x(0) \quad (2.74)$$

$$\omega_{oy} = \omega_y(0) \quad (2.75)$$

$$\omega_{oz} = \omega_z(0) \quad (2.76)$$

The kinetic energy, Eq. 2.77, and the total angular momentum, Eq. 2.78, may be defined in terms of the three inertias and the three angular velocities.

$$T = \frac{I_x \omega_{ox}^2 + I_y \omega_{oy}^2 + I_z \omega_{oz}^2}{2} \quad (2.77)$$

$$h = \sqrt{I_x^2 \omega_{ox}^2 + I_y^2 \omega_{oy}^2 + I_z^2 \omega_{oz}^2} \quad (2.78)$$

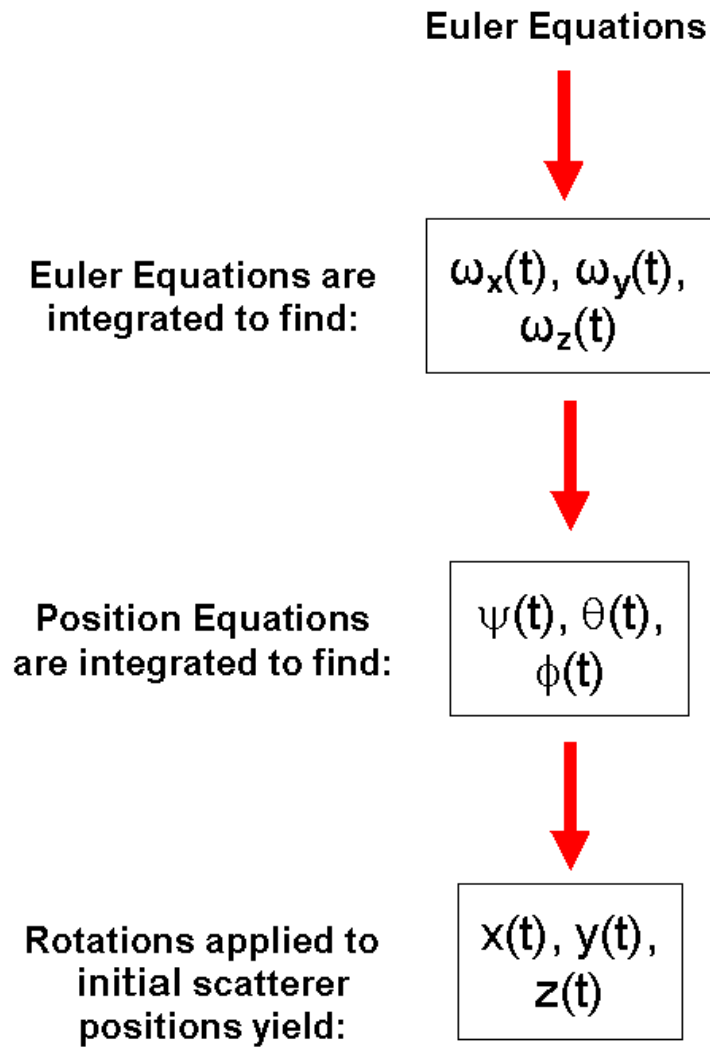


Figure 2.14: Derivation Flow: Time varying, orthogonal angular velocity rates are transformed into spin, nutation, and precessions ultimately yielding a points 3D position on a rigid body as time progresses.

There are two major cases, due to an integration constraint, which occur based upon relationships of the total angular momentum, kinetic energy and the second moment of inertia.

$$h^2 \overset{\text{Case I}}{\underset{>}{\frown}} 2I_y T \quad (2.79)$$

$$h^2 \underset{\text{Case II}}{\underset{<}{\frown}} 2I_y T \quad (2.80)$$

After integration, the angular velocities may be written in terms of Jacobi Elliptic Sine functions, total angular momentum and kinetic energy. All three elliptic sinusoids,  $sn$ ,  $cn$  and  $dn$ , may be defined in terms of trigonometric functions and  $A(u, k)$  where  $A$  is the Jacobi Amplitude function. Jacobi  $sn$  and  $dn$  are plotted in Fig. 2.15 for various elliptic moduli (the parameter  $k$  appearing in Eq. 2.81 through Eq. 2.83).

$$sn(u, k) = \sin(A(u, k)) \quad (2.81)$$

$$cn(u, k) = \cos(A(u, k)) \quad (2.82)$$

$$dn(u, k) = \frac{\partial A(u, k)}{\partial u} = \sqrt{1 - k^2 sn(u, k)^2} \quad (2.83)$$

The angular velocities that result upon solving the Euler equations may be seen in Table 2.4. The major difference in this second case versus the first case is the swapping of  $cn$  and  $dn$ .

Table 2.4: Angular Velocities of Orthogonal Axis

Angular Velocity	Case I	Case II
$\omega_x$	$\alpha dn(p_I t, k_I)$	$\alpha cn(p_{II} t, k_{II})$
$\omega_y$	$\beta_I sn(p_I t, k_I)$	$\beta_{II} sn(p_{II} t, k_{II})$
$\omega_z$	$\gamma cn(p_I t, k_I)$	$\gamma dn(p_{II} t, k_{II})$

The constants  $\alpha$ ,  $\beta$ , and  $\gamma$ , which appear in the expressions in Table 2.4, are defined in Eq. 2.84 through Eq. 2.87, and are defined solely in terms of the principle moments of

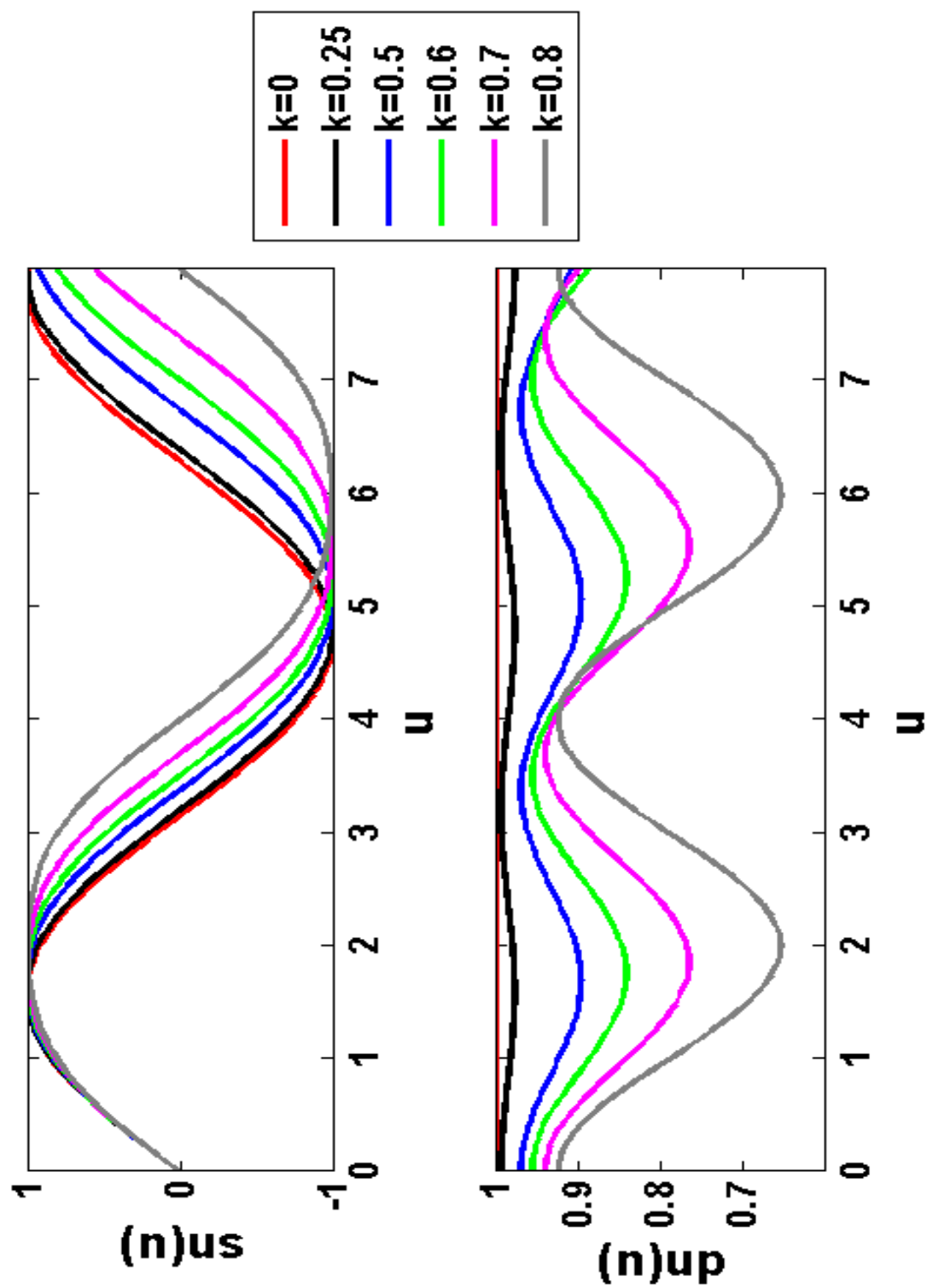


Figure 2.15: Jacobi Elliptic Sinusoids: The first order effect of an Elliptic Modulus  $k$  increase is an increase of the period.

inertia, the kinetic energy and the angular momentum.

$$\alpha = \sqrt{\frac{h^2 - 2I_z T}{I_x(I_x - I_z)}} \quad (2.84)$$

$$\gamma = \sqrt{\frac{2I_x T - h^2}{I_z(I_x - I_z)}} \quad (2.85)$$

$$\beta_I = \sqrt{\frac{2I_x T - h^2}{I_y(I_x - I_y)}} \quad (2.86)$$

$$\beta_{II} = \sqrt{\frac{h^2 - 2I_z T}{I_y(I_y - I_z)}} \quad (2.87)$$

The principle argument, or frequency, of the sinusoids are given in Eq. 2.88 and Eq. 2.89 for the two solution cases.

$$p_I = \sqrt{\frac{(h^2 - 2I_z T)(I_x - I_y)}{I_x I_y I_z}} \quad (2.88)$$

$$p_{II} = \sqrt{\frac{(2I_x T - h^2)(I_y - I_z)}{I_x I_y I_z}} \quad (2.89)$$

The  $k$  parameter, or elliptic modulus, determines the ellipticity of the Jacobi functions and is given by Eq. 2.90 and Eq. 2.91 for the two cases. When  $k$  becomes zero, the angular velocities degenerate to pure sinusoids.

$$k_I = \sqrt{\frac{(I_y - I_z)(2I_x T - h^2)}{(I_x - I_y)(h^2 - 2I_z T)}} \quad (2.90)$$

$$k_{II} = \sqrt{\frac{(I_x - I_y)(h^2 - 2I_z T)}{(I_y - I_z)(2I_x T - h^2)}} \quad (2.91)$$

We may now relate the angular velocity functions defined in Table 2.4 to the Euler rotation angles. This relationship is given by a system of differential equations whose partial solution is found in the literature.

$$\omega_x = \sin(\psi)\dot{\theta} - \sin(\theta)\cos(\psi)\dot{\phi} \quad (2.92)$$

$$\omega_y = \cos(\psi)\dot{\theta} - \sin(\theta)\sin(\psi)\dot{\phi} \quad (2.93)$$

$$\omega_z = \cos(\theta)\dot{\phi} + \dot{\psi} \quad (2.94)$$

Synge and Matsuni[33] show how this set of differential equations may be rearranged to acquire two of the rotation angles without integration, thus giving us nutation, Eq. 2.96,

and spin, Eq. 2.95. As part of our work we needed to integrate Eq. 2.97 to obtain an analytic solution for the precession angle.

$$\tan \psi = \frac{I_y \omega_y}{I_x \omega_x} \quad (2.95)$$

$$\cos \theta = \frac{I_z \omega_z}{h} \quad (2.96)$$

$$\dot{\phi} = \frac{\omega_y \sin \psi - \omega_x \cos \psi}{\sin \theta} \quad (2.97)$$

There are some difficulties in this integration. The equations for  $\omega_x$  and  $\omega_y$  contain Jacobi Elliptic sinusoids, which although they are well defined special functions, when integrated yield Elliptic Integrals. Throughout the literature, the precession is found by numerical quadrature[44] using the known nutation and spin or in terms of theta function series expansions[51]. However, in our case an analytic solution is essential to the asymmetry analysis.

### 2.6.3 Integration of the Precession Function

For completeness, the two possible cases for time-varying angular velocities must both be considered in the process of finding the precession.

$$\psi_I = \tan^{-1} \left( -\frac{I_y(\beta_1 \operatorname{sn}(p_1, k_1))}{I_x(\alpha \operatorname{dn}(p_1, k_1))} \right) \quad (2.98)$$

$$\theta_I = \cos^{-1} \left( \frac{I_z \gamma \operatorname{cn}(p_1, k_1)}{h} \right) \quad (2.99)$$

$$\psi_{II} = \tan^{-1} \left( -\frac{I_y(\beta_2 \operatorname{sn}(p_2, k_2))}{I_x(\alpha \operatorname{cn}(p_2, k_2))} \right) \quad (2.100)$$

$$\theta_{II} = \cos^{-1} \left( \frac{I_z \gamma \operatorname{dn}(p_2, k_2)}{h} \right) \quad (2.101)$$

The first step in our effort to integrate Eq. 2.97 is to replace all of the Jacobi Elliptic  $\operatorname{cn}$  and  $\operatorname{dn}$  functions with the  $\operatorname{sn}$  function using their trigonometric-similar properties as listed in [18]. The symbolic mathematics software package MAPLE was used to assist in this simplification to produce Eq. 2.103 and Eq. 2.104 from Eq. 2.102.

$$\dot{\phi}(t) = \frac{\omega_y \sin \psi - \omega_x \cos \psi}{\sin \theta} \quad (2.102)$$

$$\dot{\phi}_I(t) = \frac{-h(2T \operatorname{sn}(pt, k)^2 I_x - 2I_z T - \operatorname{sn}(pt, k)^2 h^2 + h^2)}{(2\operatorname{sn}(pt, k)^2 I_x T I_z - 2I_x T I_z + h^2 I_x - \operatorname{sn}(pt, k)^2 h^2 I_z)} \quad (2.103)$$

$$\dot{\phi}_{II}(t) = \frac{-h(-I_z + I_x \operatorname{sn}(pt, k)^2 + I_y - I_y \operatorname{sn}(pt, k)^2)}{(-I_y \operatorname{sn}(pt, k)^2 I_z + I_y I_x - I_x I_z + I_z I_x \operatorname{sn}(pt, k)^2)} \quad (2.104)$$

Further variable rearrangement produces Eq. 2.105. This equation may be used to represent both motion cases.

$$\dot{\phi}(t) = \frac{h(I_z - I_x \operatorname{sn}(pt, k)^2)}{I_x I_z (\operatorname{sn}(pt, k)^2 - 1)} \quad (2.105)$$

The only difference between the two motion cases is the parameter  $n$ , as shown in Eq. 2.106 and Eq. 2.107.

$$n_I = \frac{(2I_x T - h^2)I_z}{(2I_z T - h^2)I_x} \quad (2.106)$$

$$n_{II} = \frac{(I_y - I_x)I_z}{(I_y - I_z)I_x} \quad (2.107)$$

The next step is to perform a change of variables, replacing  $\operatorname{sn}(pt, k)$  with  $\nu$ [12].

$$\dot{\phi}(\nu) = \frac{h(I_x - I_z n \nu^2)}{I_x I_z (1 - n \nu^2)} \frac{1}{p \sqrt{1 - \nu^2} \sqrt{1 - k^2 \nu^2}} \quad (2.108)$$

Eq. 2.108 may be reorganized to form Eq. 2.109.

$$\dot{\phi}(\nu) = \frac{h(I_x - I_z)}{I_x I_z (1 - n \nu^2) p \sqrt{1 - \nu^2} \sqrt{1 - k^2 \nu^2}} - \frac{h}{I_z p \sqrt{1 - \nu^2} \sqrt{1 - k^2 \nu^2}} \quad (2.109)$$

This new function,  $\dot{\phi}(\nu)$ , may be integrated directly to find  $\phi(\nu)$ .

$$\phi(\nu) = \int \dot{\phi}(\nu) d\nu \quad (2.110)$$

$$\phi(\nu) = \frac{h(I_x - I_z)}{p I_x I_z} \mathbf{\Pi}(\nu, n, k) - \frac{h}{p I_z} \mathbf{F}(\nu, k) \quad (2.111)$$

A complete description of the mathematical properties of the Incomplete Elliptic Integrals of the First and Third kinds,  $\mathbf{F}(\mathbf{u}, \mathbf{k})$  and  $\mathbf{\Pi}(u, n, k)$  respectively, may be found in [18]. As seen in Eq. 2.112 and Eq. 2.113, they are each defined in terms of an indefinite integral.

$$\mathbf{F}(u, k) = \int_0^u \frac{1}{\sqrt{1 - t^2} \sqrt{1 - k^2 t^2}} dt \quad (2.112)$$

$$\mathbf{\Pi}(u, n, k) = \int_0^u \frac{1}{(1 - nt^2) \sqrt{1 - t^2} \sqrt{1 - k^2 t^2}} dt \quad (2.113)$$

One useful property of an Incomplete Elliptic Integral of the first kind was exploited to simplify the equation for precession. The function,  $\mathbf{F}(\mathbf{x}, \mathbf{k})$ , is the inverse of  $sn(x, k)$ . The final result is given by Eq. 2.114. A complete description of the three Euler rotations may be seen in Eq. 2.114, Eq. 2.115, and Eq. 2.116. These three functions,  $\psi$ ,  $\theta$  and  $\phi$  allow a complete analytic description of a rigid body's rotational motion.

$$\phi(t) = \frac{h(I_x - I_z)}{pI_x I_z} \mathbf{\Pi}(sn(pt, k), n, k) - \frac{ht}{I_z} \quad (2.114)$$

$$\theta(t) = \cos^{-1} \left( \frac{I_z \omega_z}{h} \right) \quad (2.115)$$

$$\psi(t) = \tan^{-1} \left( \frac{I_y \omega_y}{I_x \omega_x} \right) \quad (2.116)$$

An example of synthetically generated rotations given this motion model may be found in Fig. 2.16 and Fig. 2.17. Fig. 2.16 shows the rotations in radians. It shows a strong linearly increasing component in the spin and precession, while the nutation does not grow linearly with time. The target completes nearly 10 spin revolutions while precessing only 4 revolutions. Fig. 2.17 shows the rotational rates. These are only constant functions in the case of a symmetric target. Additional examples may be found in Appendix B.



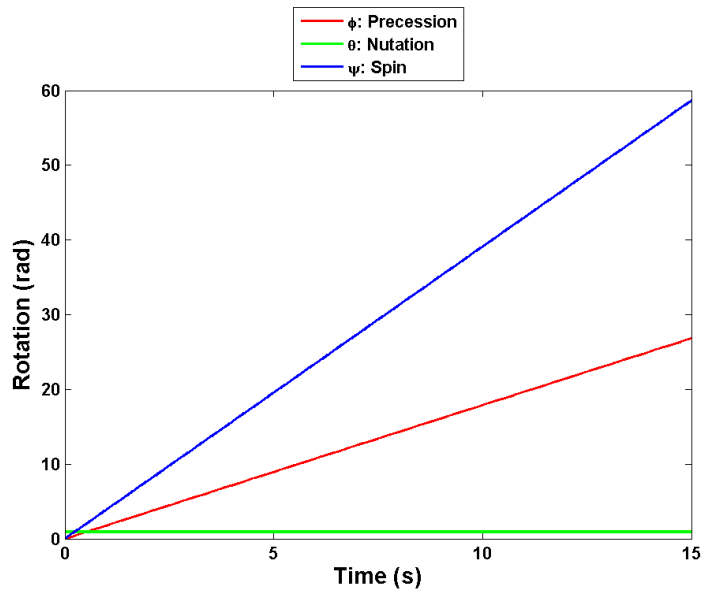


Figure 2.16: Spin, nutation and precession:  $\bar{I} = [150.0, 130.0, 30.0]$ ,  $\bar{\omega} = [1.0, 1.0, 5.0]$ . This plot shows the rotations of a target which is spinning faster than it is precessing.

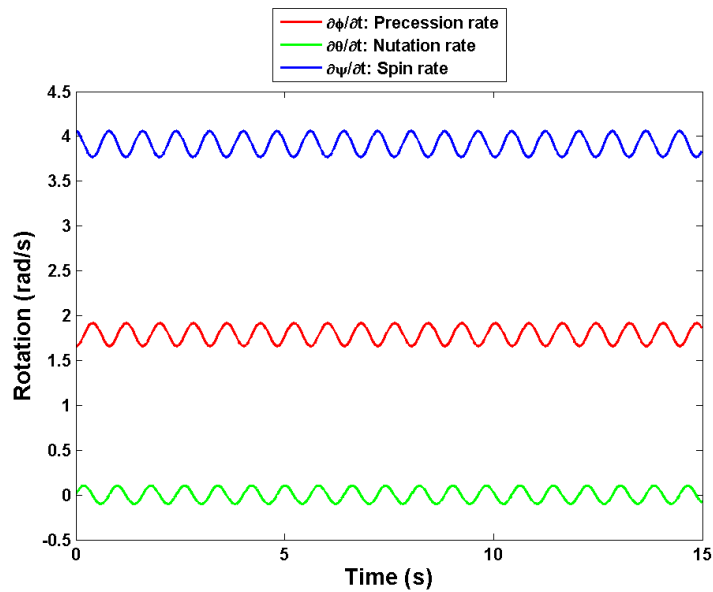


Figure 2.17: Spin, nutation and precession rates:  $\bar{I} = [150.0, 130.0, 30.0]$ ,  $\bar{\omega} = [1.0, 1.0, 5.0]$ . This plot shows the three rotational rates of an asymmetric target. The sinusoidal perturbation of each rate is due to the target's asymmetry. The nutation's average rate is zero.

## Chapter 3

# Asymmetry Analysis

This chapter explores how asymmetry and initial angular velocities affect a target's motion. Section 3.1 shows how initial conditions affect the motion case selection and the elliptic modulus,  $k$ . Section 3.2 shows the rotation simplifications that occur when the target is axially symmetric. Section 3.3 introduces rotation models for a nearly symmetric target. Section 3.4 presents a harmonic decomposition analysis of the target's angular frequency spectrum. Section ?? introduces a method for estimating the elliptic modulus of a nearly symmetric target.

### 3.1 Asymmetric Target

As discussed in section 2.6.2, there are two motion cases which may occur. The motion of a target is specified by similar, yet different, equations for each case. The rotation equations for these two cases are specified in Eq. 3.1 through Eq. 3.6. As seen in Eq. 3.1 and Eq. 3.2 the precession is composed of the same functions for the two motion cases, differing only by parameter values of,  $k$ ,  $n$  and  $p$ .

$$\phi_I(t) = \frac{h(I_x - I_z)}{p_I I_x I_z} \mathbf{\Pi}(sn(p_I t, k_I), n_I, k_I) - \frac{ht}{I_z} \quad (3.1)$$

$$\phi_{II}(t) = \frac{h(I_x - I_z)}{p_{II} I_x I_z} \mathbf{\Pi}(sn(p_{II} t, k_{II}), n_{II}, k_{II}) - \frac{ht}{I_z} \quad (3.2)$$

The primary difference for the nutation and spin is the swapping of the Jacobi  $cn$  and

$dn$  functions, as seen in Eq. 3.3 through Eq. 3.6.

$$\theta_I(t) = \cos^{-1} \left( \frac{I_z \gamma cn(p_I t, k_I)}{h} \right) \quad (3.3)$$

$$\theta_{II}(t) = \cos^{-1} \left( \frac{I_z \gamma dn(p_{II} t, k_{II})}{h} \right) \quad (3.4)$$

$$\psi_I(t) = \tan^{-1} \left( \frac{\beta_I sn(p_I t, k_I)}{\alpha dn(p_I t, k_I)} \right) \quad (3.5)$$

$$\psi_{II}(t) = \tan^{-1} \left( \frac{\beta_{II} sn(p_{II} t, k_{II})}{\alpha cn(p_{II} t, k_{II})} \right) \quad (3.6)$$

The transition between case  $I$  and case  $II$  occurs when Eq. 3.7 is satisfied.

$$h^2 = 2I_y T \quad (3.7)$$

This relationship can be expanded to include the angular momentum,  $h$ , and the kinetic energy,  $T$ , in terms of the inertia and initial angular velocities as shown in Eq. 3.8.

$$I_x^2 \omega_{ox}^2 + I_y^2 \omega_{oy}^2 + I_z^2 \omega_{oz}^2 = I_y (I_x \omega_{ox}^2 + I_y \omega_{oy}^2 + I_z \omega_{oz}^2) \quad (3.8)$$

Eq. 3.8 may be further simplified by expanding the  $I_y$  production on the right hand side and removing the  $I_y^2$  term from both sides as shown in Eq. 3.9 and Eq. 3.10.

$$I_x^2 \omega_{ox}^2 + I_y^2 \omega_{oy}^2 + I_z^2 \omega_{oz}^2 = I_x I_y \omega_{ox}^2 + I_y^2 \omega_{oy}^2 + I_y I_z \omega_{oz}^2 \quad (3.9)$$

$$I_x^2 \omega_{ox}^2 + I_z^2 \omega_{oz}^2 = I_x I_y \omega_{ox}^2 + I_y I_z \omega_{oz}^2 \quad (3.10)$$

Eq. 3.10 may then be solved for  $I_y$  as shown in Eq. 3.11 and Eq. 3.12. Note that the relationship shown in Eq. 3.12 does not include  $\omega_{oy}$ .

$$I_x^2 \omega_{ox}^2 + I_z^2 \omega_{oz}^2 = I_y (I_x \omega_{ox}^2 + I_z \omega_{oz}^2) \quad (3.11)$$

$$I_y = \frac{I_x^2 \omega_{ox}^2 + I_z^2 \omega_{oz}^2}{I_x \omega_{ox}^2 + I_z \omega_{oz}^2} \quad (3.12)$$

As shown in Eq. 3.13 through Eq. 3.15,  $I_y$  and  $I_z$  may be expressed as fractional values of  $I_x$ . This proves useful for illustrating the transition point between the motion cases.

$$\frac{I_x - I_y}{I_x} = \frac{\left( I_x - \frac{I_x^2 \omega_{ox}^2 + I_z^2 \omega_{oz}^2}{I_x \omega_{ox}^2 + \frac{I_z I_x \omega_{oz}^2}{I_x}} \right)}{I_x} \quad (3.13)$$

$$\frac{I_x - I_y}{I_x} = \frac{I_z \omega_{oz}^2 (I_x - I_z)}{I_x (I_x \omega_{ox}^2 + I_z \omega_{oz}^2)} \quad (3.14)$$

$$\frac{I_x - I_y}{I_x} = \frac{\frac{I_z}{I_x} \omega_{oz}^2 \left(1 - \frac{I_z}{I_x}\right)}{\omega_{ox}^2 + \frac{I_z}{I_x} \omega_{oz}^2} \quad (3.15)$$

Eq. 3.15 may be plotted as in Fig. 3.1 for various inertia values with respect to  $I_x$  and initial angular velocities. The axes values pertain to the fractional value of inertia with respect to  $I_x$ . The  $x$  axis is the ratio of  $I_z$  to  $I_x$ , while the  $y$  axis is the ratio of the deviation of  $I_y$  from  $I_x$  ( $\epsilon$ ) with respect to  $I_x$ . The region above each curve corresponds to  $h^2 > 2I_y T$  whereas the region below corresponds to  $h^2 < 2I_y T$ .

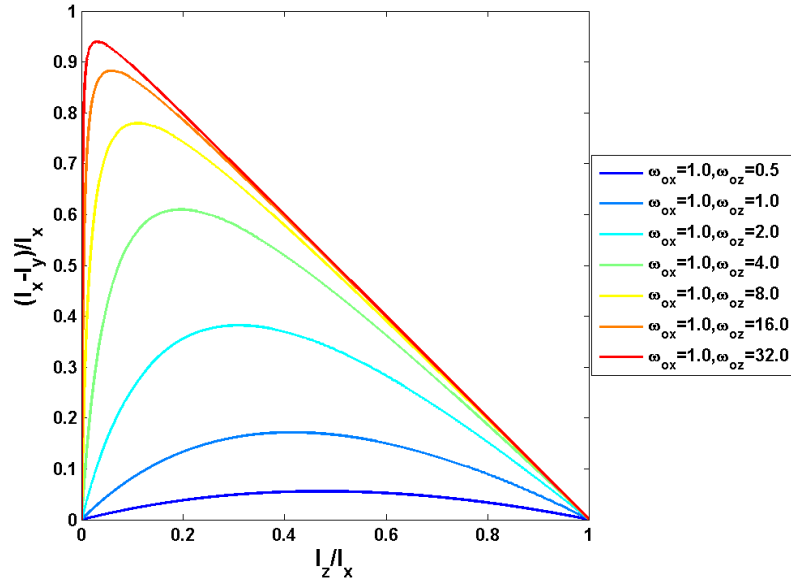


Figure 3.1: Motion case transitions for various initial conditions. The region above a curve corresponds to inertia values leading to case *I* motion, whereas the region below corresponds to inertia values leading to case *II* motion. As  $\frac{\omega_z}{\omega_x}$  increases, the region of inertia values covered by case *II* increases.

The elliptic modulus,  $k$ , performs a strong role in the specification of the rotational motion of the target. Surface plots for the elliptic modulus for various inertia values with respect to  $I_x$  and initial angular velocities may be seen in Fig. 3.2 through Fig. 3.4. The values of  $k$  for various faster spinning targets may be seen in Fig. 3.2. The color blue corresponds to a small elliptic modulus, whereas green corresponds to a modulus of 0.5 and the yellow to red colors a large modulus. The upper triangular region is empty due to the

constraint that  $I_y$  must be greater than or equal to  $I_z$ .

Fig. 3.3 shows the modulus for targets whose  $\omega_z$  is at half the rate of that found in Fig. 3.2. It shows that the range of inertia values producing a small  $k$  has reduced. Whereas in Fig. 3.2 it was possible to have an elliptic modulus below 0.5 with an  $I_y$  deviation being nearly 60% of  $I_x$ , this deviation may now only be as large as 40%. The final elliptic modulus example, seen in Fig. 3.4, shows that for a slowly spinning target the modulus quickly spikes to large value for small target deviations of  $I_y$  from  $I_x$ . In all three examples,  $k$  approaches 1 at the case transition point. These examples show that the angular velocities have an important impact in defining the modulus for a given moment of inertia.

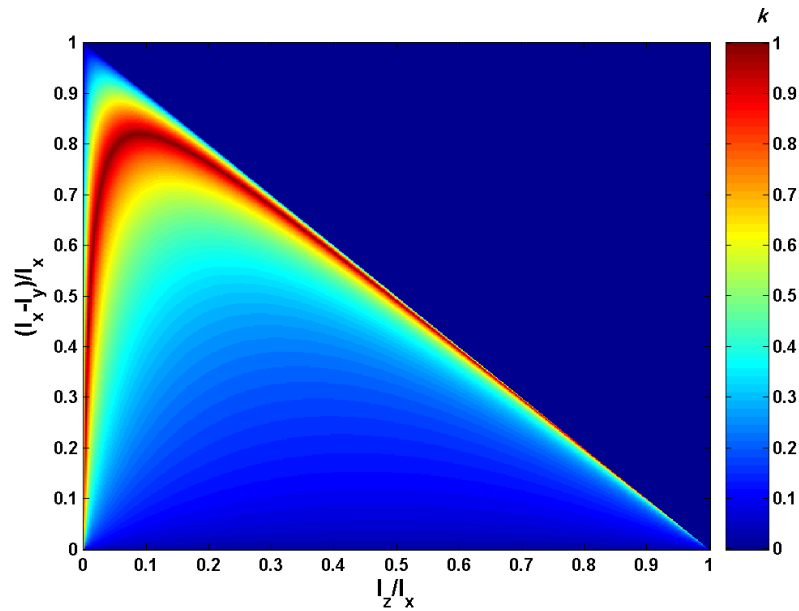


Figure 3.2: Values of  $k$  for  $\bar{\omega} = [1, 1, 10]$

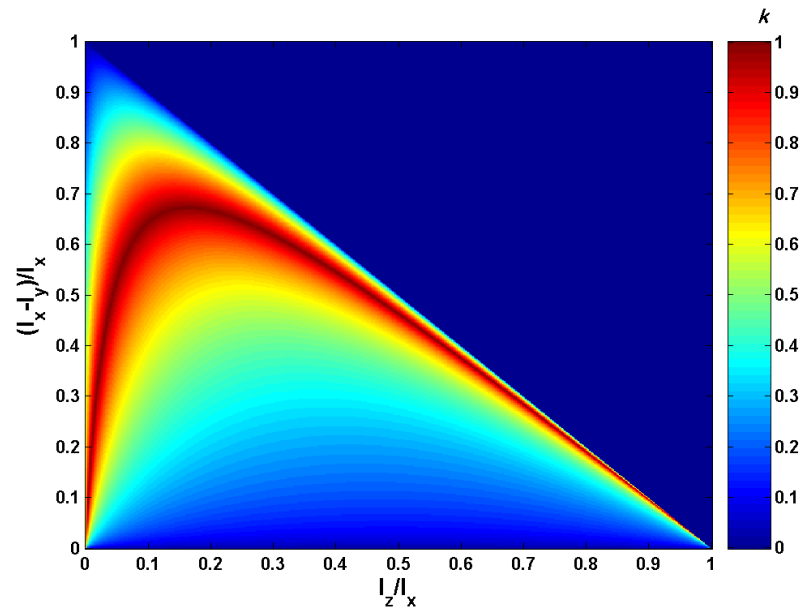


Figure 3.3: Values of  $k$  for  $\bar{\omega} = [1, 1, 5]$

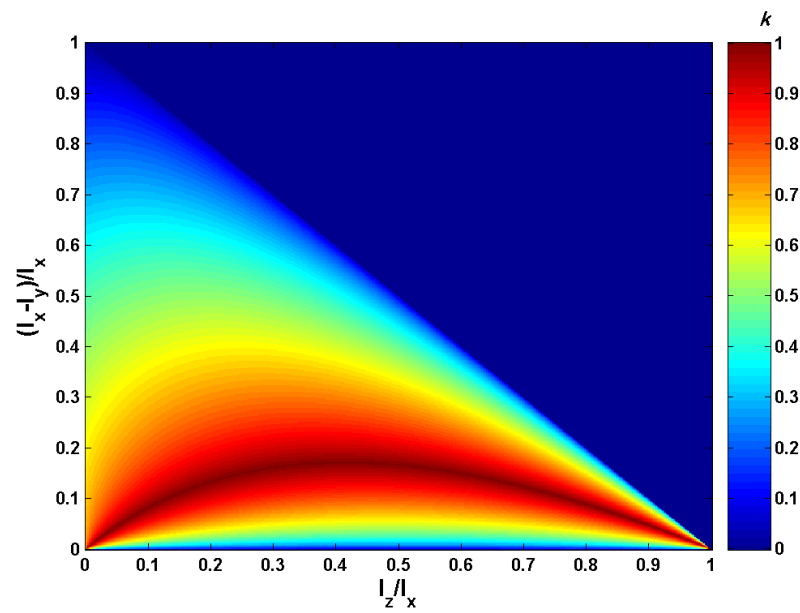


Figure 3.4: Values of  $k$  for  $\bar{\omega} = [1, 1, 1]$

### 3.2 Axially Symmetric Target

If the assumption can be made that the target is axis-symmetric,  $I_x = I_y$ , the equations can be reduced to much simpler functions of time, the inertial vector, angular momentum and the kinetic energy [25][37]. In the angular velocities, the Jacobi elliptic functions  $sn$ ,  $cn$ , and  $dn$ , are simplified to standard trigonometric functions, as seen in Eq. 3.16 through Eq. 3.18.

$$sn(u, 0) = \sin(u) \quad (3.16)$$

$$cn(u, 0) = \cos(u) \quad (3.17)$$

$$dn(u, 0) = 1 \quad (3.18)$$

Also, the Incomplete Elliptic Integral of the third kind becomes an inverse sine.

$$\mathbf{\Pi}(u, 0, 0) = \sin^{-1}(u) \quad (3.19)$$

An axially symmetric target is always governed by the case  $II$  motion equations. This can be verified using the case  $II$  relationship found in Eq. 3.20.

$$h^2 < 2I_y T \quad (3.20)$$

$$I_x^2 \omega_{ox}^2 + I_y^2 \omega_{oy}^2 + I_z^2 \omega_{oz}^2 \leq I_y (I_x \omega_{ox}^2 + I_y \omega_{oy}^2 + I_z \omega_{oz}^2) \quad (3.21)$$

A short proof begins by asserting the axial symmetry condition shown in Eq. 3.22 and Eq. 3.23.

$$I_y = I_x \quad (3.22)$$

$$I_x^2 \omega_{ox}^2 + I_x^2 \omega_{oy}^2 + I_z^2 \omega_{oz}^2 < I_x (I_x \omega_{ox}^2 + I_x \omega_{oy}^2 + I_z \omega_{oz}^2) \quad (3.23)$$

Eq. 3.23 may be simplified by grouping  $\omega_{ox}$  and  $\omega_{oy}$ .

$$I_x^2 (\omega_{ox}^2 + \omega_{oy}^2) + I_z^2 \omega_{oz}^2 < I_x^2 (\omega_{ox}^2 + \omega_{oy}^2) + I_x I_z \omega_{oz}^2 \quad (3.24)$$

Dividing both sides by the expression on the right hand side of Eq. 3.24 forms Eq. 3.25. The quantity on the left hand side is always less than one since  $I_z^2$  is always less than  $I_x I_z$ .

$$\frac{I_x^2 (\omega_{ox}^2 + \omega_{oy}^2) + I_z^2 \omega_{oz}^2}{I_x^2 (\omega_{ox}^2 + \omega_{oy}^2) + I_x I_z \omega_{oz}^2} < 1 \quad (3.25)$$

The case  $II$  equations may be simplified using Eq. 3.16 through Eq. 3.19. Note that in Eq. 3.30,  $\theta$  is a constant, while in Eq. 3.28 and Eq. 3.33 both  $\phi$  and  $\psi$  are linear functions of time.

$$\phi(t) = \frac{h(I_x - I_z)}{pI_x I_z} \mathbf{\Pi}(sn(pt, k), n, k) - \frac{ht}{I_z} \quad (3.26)$$

$$= \frac{ht(I_x - I_z)}{I_x I_z} - \frac{ht}{I_z} \quad (3.27)$$

$$= \frac{-ht}{I_x} \quad (3.28)$$

$$\theta(t) = \cos^{-1} \left( \frac{I_z \gamma dn(pt, k)}{h} \right) \quad (3.29)$$

$$= \cos^{-1} \left( \frac{I_z \gamma}{h} \right) \quad (3.30)$$

$$\psi(t) = \tan^{-1} \left( \frac{\beta sn(pt, k)}{\alpha cn(pt, k)} \right) \quad (3.31)$$

$$= \tan^{-1} \left( \frac{\sin(pt)}{\cos(pt)} \right) \quad (3.32)$$

$$= pt \quad (3.33)$$

With the elimination of the elliptic functions, there are now clear rates to be found. The precession and spin rates may be seen in Eq. 3.34 and Eq. 3.35 respectively.

$$\omega_\phi = \frac{h}{I_x} \quad (3.34)$$

$$\omega_\psi = p \quad (3.35)$$

As seen in Eq. 3.36 through Eq. 3.38, the rotation time functions (Eq. 2.59 to Eq. 2.61) are simpler in the axially symmetric case.

$$f_\phi(t) = \omega_\phi t \quad (3.36)$$

$$f_\theta(t) = 0 \quad (3.37)$$

$$f_\psi(t) = \omega_\psi t \quad (3.38)$$

This allows for a reorganization of terms in Eq. 3.39, resulting in Eq. 3.40.

$$R_T = \underbrace{R_z(-f_\phi(t))}_{\text{Precession}} \underbrace{R_y(-f_\theta(t) - \kappa_\theta)}_{\text{Nutation}} \underbrace{R_z(-f_\psi(t))}_{\text{Spin}} \quad (3.39)$$

$$= R_z(-\omega_\phi t) R_y(-\kappa_\theta) R_z(-\omega_\psi t) \quad (3.40)$$



This leads a simplified range function shown in Eq. 3.41. It shows that the RTI for an axially symmetric target may be expressed by a precession rate, a fixed nutation angle, a spin rate, and a projection down some axis.

$$r_m(t) = C_{xyz} R_z(-\omega_\phi t) R_y(-\kappa_\theta) R_z(-\omega_\psi t) p_m \quad (3.41)$$

### 3.3 Nearly Symmetric Target

The complexity of a full asymmetric motion model may not be needed to represent the signature of a near axially symmetric target sufficiently well to provide useful information to the analyst. Instead, a model that extends the solutions from the axially symmetric case for perturbative deviations of  $I_y$  from  $I_x$  may be a sufficient representation. Some parameters in the complete motion model may be written in terms of a power series expansion about symmetry while other functions may be modelled using simpler functions.

A nearly symmetric target shall be defined as a one having initial conditions such that the case  $II$  motion equations are invoked, as found with the symmetric target, with an elliptic modulus,  $k$ , smaller than 0.5. The inertial deviation from symmetry may be expressed in terms of  $\epsilon$ , as defined in Eq. 3.42.

$$I_y = I_x - \epsilon \quad (3.42)$$

It will be shown that each rotation may be expressed as the sum of a linear term stemming from the target symmetry, some linear perturbation, and some sinusoidal perturbation. This new model reduces the dependency upon Jacobi Elliptic functions. These new models present an intuitive view of the development of target motion behavior as the target deviates from axial symmetry.

The first equations to review for the asymmetric motion simplification development are the Jacobi elliptic sinusoids, (Eq. 3.43 and Eq. 3.44). The  $sn$  and  $dn$  functions can be equivalently represented as sin and cos of an Elliptic Amplitude function  $A(u, k)$ .

$$sn(u, k) = \sin(A(u, k)) \quad (3.43)$$

$$cn(u, k) = \cos(A(u, k)) \quad (3.44)$$

In the instances where a function is approximated by a model, relative error shall be used to evaluate the accuracy of the model. Percent relative error is defined as shown in Eq. 3.45 where  $f$  is the function of interest and  $\tilde{f}$  is the model.

$$error = 100 \frac{|f - \tilde{f}|}{f} \quad (3.45)$$

A model of the Jacobi Amplitude function may be expressed in terms of  $\mathbf{K}$ , the Complete Elliptic Integral of the first kind.

$$\mathbf{K}(k) = \int_0^1 \frac{1}{\sqrt{1-t^2}\sqrt{1-k^2t^2}} dt \quad (3.46)$$

The parametric model for the Jacobi function we will introduce is based on its mean value and the recognition that  $A(u, k)$  has a periodic component which is nearly sinusoidal. We modelled it by the sum of a linear term (with respect to  $u$ ) and a single sinusoid as seen in Eq. 3.47 and found the coefficients  $c_0$ ,  $c_1$  and  $c_2$  to achieve the best match. As seen in Eq. 3.48, approximating the function in this manner shows its internal structure in simpler, more meaningful terms compared to its exact integral formulation.

$$\tilde{A}(u, k) = c_0 u + c_1 \sin(c_2 u) \quad (3.47)$$

$$= \frac{u\pi}{2\mathbf{K}(k)} + \frac{(2\mathbf{K}(k) - \pi)}{2\pi} \sin\left(\frac{u\pi}{\mathbf{K}(k)}\right) \quad (3.48)$$

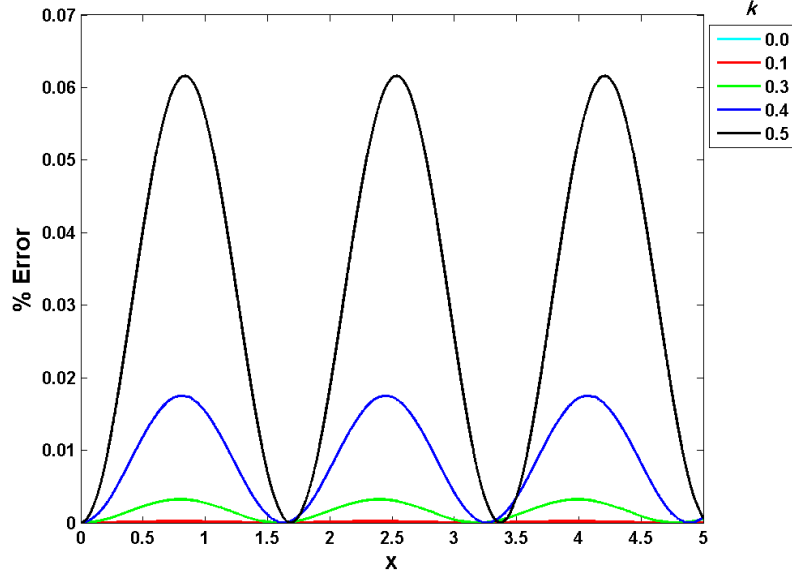
This amplitude model shows that the function contains a dominant linear term in  $u$  and a perturbing sinusoid. As  $k$  approaches zero, the sinusoid amplitude approaches zero and the linear term becomes simply the argument  $u$ . This model, when used with the  $sn$  and  $cn$  functions, forms an approximation with a maximum relative error of 0.062% for  $k = 0.5$ . Relative error for various other elliptic modulus values may be seen in Fig. 3.5.

The  $dn$  function may be written in exact form as the derivative of  $A$ , as seen in Eq. 3.50.

$$dn(u, k) = \frac{\partial(A(u, k))}{\partial u} \quad (3.49)$$

$$= \sqrt{1 - k^2 sn(u, k)^2} \quad (3.50)$$

For the purpose of our derivation, it is convenient to have it in the form of a linear term plus a periodic term. This is due to the ultimately desired three term rotation formulations.

Figure 3.5: Error in  $sn$  Model

This may be accomplished by instead taking the derivative of  $\tilde{A}$ , as seen in Eq. 3.52.

$$dn(u, k) \simeq \frac{\partial(\tilde{A}(u, k))}{\partial u} \quad (3.51)$$

$$\simeq \frac{\pi}{2\mathbf{K}(k)} + \frac{(2\mathbf{K}(k) - \pi)}{2\mathbf{K}(k)} \cos\left(\frac{u\pi}{\mathbf{K}(k)}\right) \quad (3.52)$$

The approximate Jacobi sinusoids used for the remainder of this work may be seen in Eq. 3.53, Eq. 3.54, and Eq. 3.55.

$$\tilde{s}n(u, k) = \sin\left(\frac{u\pi}{2\mathbf{K}(k)} + \frac{(2\mathbf{K}(k) - \pi)}{2\pi} \sin\left(\frac{u\pi}{\mathbf{K}(k)}\right)\right) \quad (3.53)$$

$$\tilde{c}n(u, k) = \sin\left(\frac{u\pi}{2\mathbf{K}(k)} + \frac{(2\mathbf{K}(k) - \pi)}{2\pi} \sin\left(\frac{u\pi}{\mathbf{K}(k)}\right)\right) \quad (3.54)$$

$$\tilde{d}n(u, k) = \frac{\pi}{2\mathbf{K}(k)} + \frac{(2\mathbf{K}(k) - \pi)}{2\mathbf{K}(k)} \cos\left(\frac{u\pi}{\mathbf{K}(k)}\right) \quad (3.55)$$

If a representation without any Jacobi functions is desired,  $\mathbf{K}$  may be approximated as a low order polynomial for small  $k$ . The relative error versus  $k$  for various orders of the  $\mathbf{K}$  function may be seen in Fig. 3.6.

$$\tilde{\mathbf{K}}(k) = \frac{\pi}{2} \left[ 1 + \frac{1}{4}k^2 + \frac{9}{64}k^4 + \frac{25}{256}k^6 + \frac{1225}{16384}k^8 + \dots \right] \quad (3.56)$$

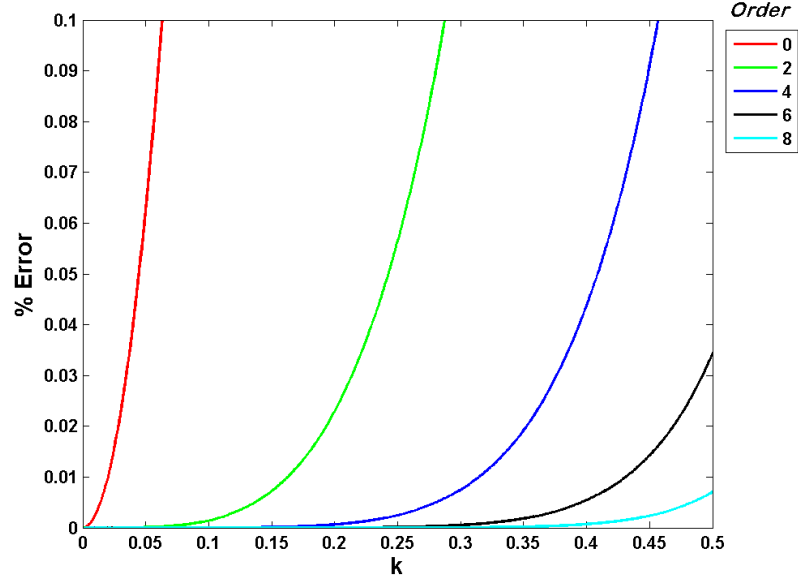


Figure 3.6: Error in  $\mathbf{K}(k)$  model,  $\tilde{\mathbf{K}}(k)$

### 3.3.1 Precession $\phi(t)$ Model

The precession, Eq. 3.57, may be written in the three term representation without an Elliptic Integral. The first step is to rearrange the terms such that it is in the form of the term generated by an axially symmetric body plus the nonlinear Elliptic term, as seen in Eq. 3.58. Subtraction of  $pt$  allows the reorganization of terms such that term  $\frac{ht}{I_x}$  stands alone instead of  $\frac{ht}{I_z}$ .

$$\phi(t) = \frac{h(I_x - I_z)}{pI_x I_z} \mathbf{\Pi}(sn(pt, k), n, k) - \frac{ht}{I_z} \quad (3.57)$$

$$= \frac{-ht}{I_x} + \frac{h(I_x - I_z)}{pI_x I_z} (\mathbf{\Pi}(sn(pt, k), n, k) - pt) \quad (3.58)$$

The second step is to replace the integral with a linear term and a periodic term. The Elliptic Integral of the Third Kind,  $\mathbf{\Pi}$ , may be written in this simpler form given small values of  $n$  and  $k$ . This can be done using a multivariate Taylor expansion. Values of  $n$  for various moments of inertia may be seen in Fig. 3.7. The integral degenerates into a scaled

inverse sine function with an additional nonlinear portion defined in the real domain for  $-1 \leq u \leq 1$ . The error in this elliptic integral model for various order expansions for small  $n$  and  $k$  may be seen in Fig. 3.8.

$$\Pi(u, n, k) \simeq \sin^{-1}(u) (1 + r) - \left( r + \frac{3k^4 u^2}{32} \right) u \sqrt{1 - u^2} \quad (3.59)$$

$$r = \frac{9k^4}{64} + \frac{k^2}{4} + \frac{n}{2} \quad (3.60)$$

The contribution of  $n$  to the precession may also be interpreted through its contribution

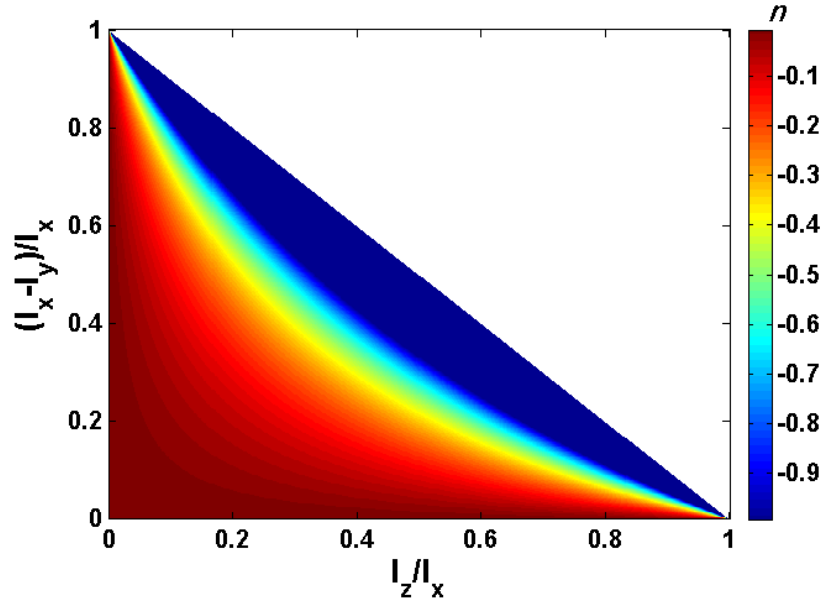


Figure 3.7:  $\Pi$ :  $n$  Values for various Inertia. Most values of interest are smaller in magnitude than 0.2.

to  $r$ , as seen in Fig. 3.9.

The domain restriction is not an issue, since as seen in Eq. 3.58 the argument  $u$  becomes a Jacobi sinusoid whose values are always within the required bounds. The elliptic integral with the Jacobi sinusoid argument may be seen in Eq. 3.61. Maximum relative error in the model for various  $n$  and  $k$  values may be seen in Fig. 3.10.

$$\begin{aligned} \tilde{\Pi}(\tilde{s}n(u, k), n, k) &= u(1 + r) \frac{\pi}{2\mathbf{K}(k)} + (1 + r) \frac{(2\mathbf{K}(k) - \pi)}{2\pi} \sin\left(\frac{u\pi}{\mathbf{K}(k)}\right) \\ &\quad - \left( r + \frac{3k^4 sn^2(u, k)}{32} \right) sn(u, k) cn(u, k) \end{aligned} \quad (3.61)$$

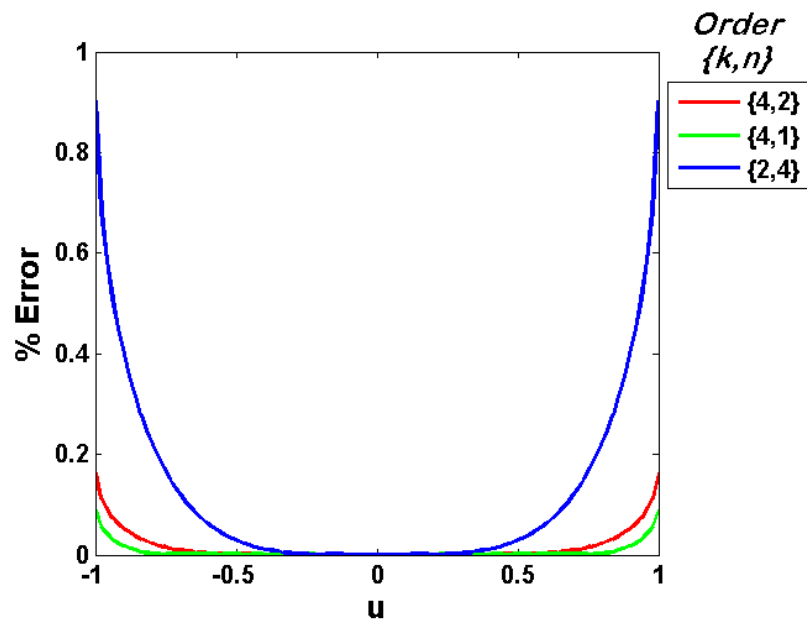


Figure 3.8: Error in  $\Pi(u, n = -0.2, k = 0.5)$  for Various Order Approximations

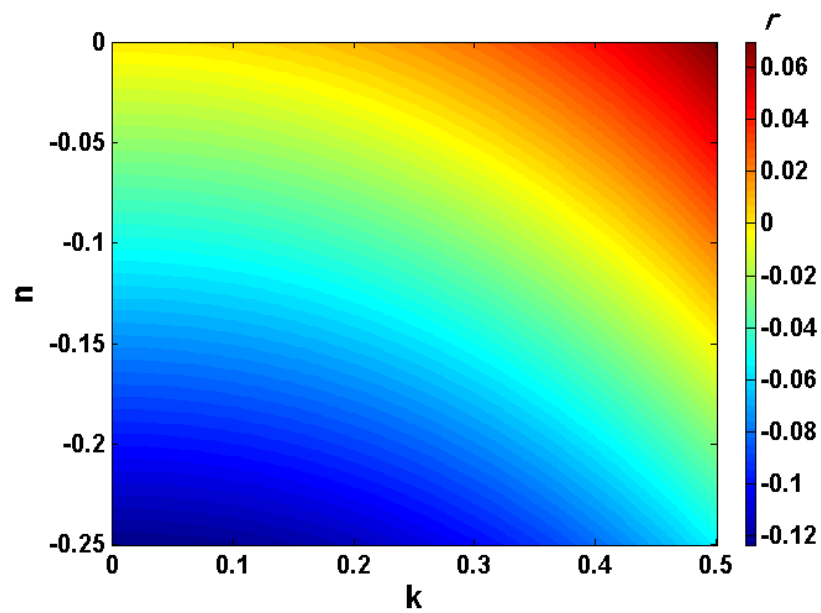


Figure 3.9: Values of  $r$  for various  $n$  and  $k$

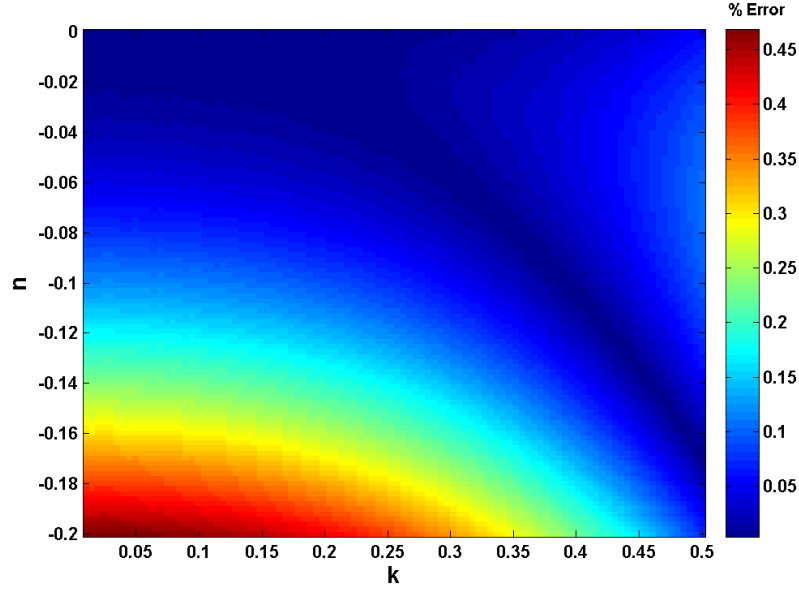


Figure 3.10: Error in  $\mathbf{\Pi}(sn(u), n, k)$  model,  $\tilde{\mathbf{\Pi}}(\tilde{sn}(u), n, k)$ , for Various  $n$  and  $k$

The substitution of Eq. 3.61 into Eq. 3.57 leads to a model of the precession function without a time varying Elliptic Integral, as seen in Eq. 3.62.

$$\begin{aligned} \tilde{\phi}(t) = & \frac{-ht}{I_x} + \frac{h(I_x - I_z)}{pI_x I_z} \left( \frac{pt\pi(1+r)}{2\mathbf{K}(k)} - pt + (1+r) \frac{(2\mathbf{K}(k) - \pi)}{2\pi} \sin\left(\frac{pt\pi}{\mathbf{K}(k)}\right) \right) \\ & + \frac{h(I_x - I_z)}{pI_x I_z} \left( r + \frac{3k^4 sn^2(pt, k)}{32} \right) sn(pt, k) cn(pt, k) \end{aligned} \quad (3.62)$$

The function in a simpler form may be seen in Eq. 3.63. This function contains the component a symmetrical body would generate, a small linear term, and an even smaller periodic term inversely proportional to the spin rate. The introduction of asymmetry adds a small sinusoidal “wobble”. The extent of the wobble is controlled by the amplitudes of

the periodic terms.

$$\begin{aligned} \tilde{\phi}(t) = & \underbrace{\frac{-ht}{I_x}}_{I_x=I_y} + \underbrace{\frac{h(I_x - I_z)(\pi + \pi r - 2\mathbf{K}(k))t}{2I_x I_z \mathbf{K}(k)}}_{\text{linear}} + \underbrace{\frac{h(I_x - I_z)}{pI_x I_z}(1 + r) \frac{(2\mathbf{K}(k) - \pi)}{2\pi} \sin\left(\frac{pt\pi}{\mathbf{K}(k)}\right)}_{\text{periodic}} \\ & + \underbrace{\frac{h(I_x - I_z)}{pI_x I_z} \left(r + \frac{3k^4 \text{sn}^2(pt, k)}{32}\right) \text{sn}(pt, k) \text{cn}(pt, k)}_{\text{periodic}} \end{aligned} \quad (3.63)$$

### 3.3.2 Nutation $\theta(t)$ Model

The first step in reorganizing the nutation is to replace the Jacobi  $dn$  function found in Eq. 3.64.

$$\cos(\theta(t)) = \frac{I_z \gamma dn(pt, k)}{h} \quad (3.64)$$

Substituting Eq. 3.55 into Eq. 3.64 makes clear the contribution of the  $dn$  function. It adds a constant offset and a periodic term.

$$\cos(\tilde{\theta}(t)) = \frac{I_z \gamma}{h} \left( \frac{\pi}{2\mathbf{K}(k)} + \frac{(2\mathbf{K}(k) - \pi)}{2\mathbf{K}(k)} \cos\left(\frac{pt\pi}{\mathbf{K}(k)}\right) \right) \quad (3.65)$$

To arrange the nutation function in the three term representation, the component generated by an axially symmetric body,  $\frac{I_z \gamma}{h}$ , needs to be a factor standing on its own. The  $\frac{1}{\mathbf{K}(k)}$  term may be viewed as a deviation from the value of  $\frac{2}{\pi}$  for small  $k$ , so the Taylor series expansion may be taken about  $k = 0$ . The relative error versus  $k$  for various orders of the this expansion may be seen in Fig. 3.11.

$$\frac{1}{\mathbf{K}(k)} = \frac{2}{\pi} - \frac{k^2}{2\pi} - \frac{5k^4}{32\pi} - \frac{11k^6}{128\pi} - \frac{469k^8}{8192\pi} - \dots \quad (3.66)$$

Substituting the model from Eq. 3.66 into Eq. 3.65 produces the desired form found in Eq. 3.68. This function contains the component an axially symmetric body would generate, a small constant term, and a periodic term.

$$\cos(\tilde{\theta}(t)) = \frac{I_z \gamma}{h} \left[ \frac{\pi}{2} \left( \frac{2}{\pi} - \frac{k^2}{2\pi} - \frac{5k^4}{32\pi} - \dots \right) + \frac{(2\mathbf{K}(k) - \pi)}{2\mathbf{K}(k)} \cos\left(\frac{pt\pi}{\mathbf{K}(k)}\right) \right] \quad (3.67)$$

$$= \underbrace{\frac{I_z \gamma}{h}}_{I_x=I_y} - \underbrace{\frac{I_z \gamma}{h} \left( \frac{k^2}{4} + \frac{5k^6}{64} + \dots \right)}_{\text{constant}} + \underbrace{\frac{I_z \gamma (2\mathbf{K}(k) - \pi)}{h \cdot 2\mathbf{K}(k)} \cos\left(\frac{pt\pi}{\mathbf{K}(k)}\right)}_{\text{periodic}} \quad (3.68)$$



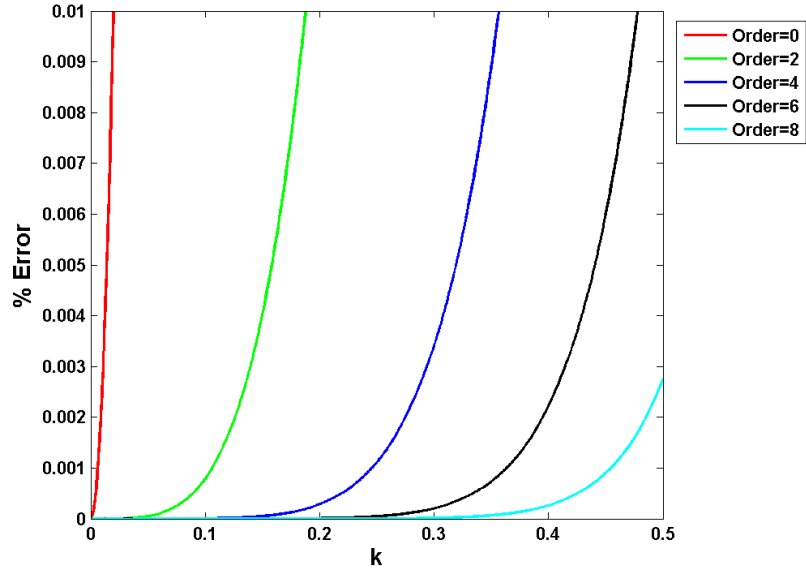


Figure 3.11: Error in  $\frac{1}{\mathbf{K}(k)}$  model

### 3.3.3 Spin $\psi(t)$ Model

The final rotation parameter function to simplify is the spin, given in Eq. 3.69.

$$\psi(t) = \tan^{-1} \left( \frac{I_y \beta \operatorname{sn}(pt, k)}{I_x \alpha \operatorname{cn}(pt, k)} \right) \quad (3.69)$$

The expression in  $\epsilon$  for  $I_y$ , from Eq. 3.42, may be substituted in to Eq. 3.69 to obtain Eq. 3.70 as the first step towards expressing the spin in terms of deviation from symmetry.

$$\psi(t) = \tan^{-1} \left( \frac{(I_x - \epsilon) \beta \operatorname{sn}(pt, k)}{I_x \alpha \operatorname{cn}(pt, k)} \right) \quad (3.70)$$

Only one of the three angular velocity scalars,  $\beta$ , contains  $I_y$  and as such it is the only one which requires an expansion. As shown in Eq. 3.73,  $\beta$  degenerates to  $\alpha$  when  $\epsilon = 0$ . Each

successive term in the expansion may be written as a product with  $\alpha$ .

$$\alpha = \sqrt{\frac{h^2 - 2I_z T}{I_x(I_x - I_z)}} \quad (3.71)$$

$$\beta = \sqrt{\frac{h^2 - 2I_z T}{I_y(I_y - I_z)}} \quad (3.72)$$

$$= \alpha \left[ 1 + \frac{2I_x - I_z}{2I_x(I_x - I_z)} \epsilon + \frac{8I_x^2 - 8I_x I_z + 3I_z^2}{8I_x^2(I_x - I_z)^2} \epsilon^2 + \dots \right] \quad (3.73)$$

Substituting Eq. 3.73 into Eq. 3.70 produces Eq. 3.74.

$$\tilde{\psi}(t) = \tan^{-1} \left( \frac{(I_x - \epsilon)}{I_x} \frac{\alpha \left[ 1 + \frac{2I_x - I_z}{2I_x(I_x - I_z)} \epsilon + \dots \right]}{\alpha} \frac{sn(pt, k)}{cn(pt, k)} \right) \quad (3.74)$$

As seen in Eq. 3.75,  $\alpha$  cancels itself out of the equation leaving only the  $\epsilon$  expansion terms.

$$\tilde{\psi}(t) = \tan^{-1} \left( \frac{(I_x - \epsilon)}{I_x} \left[ 1 + \frac{2I_x - I_z}{2I_x(I_x - I_z)} \epsilon + \dots \right] \frac{sn(pt, k)}{cn(pt, k)} \right) \quad (3.75)$$

The spin may be further simplified by introducing an inverse tangent model. The inverse tangent of a tangent is simply the argument of the tangent. The inverse tangent of a constant multiplying a tangent may be represented as the argument and an infinite sum of sinusoid products, as seen in Eq. 3.76.

$$\begin{aligned} \tan^{-1}(\tan(x)c) &= x + \sin(x)\cos(x)(c-1) - \sin(x)^3\cos(x)(c-1)^2 \\ &\quad - \frac{1}{3}\sin(x)^3\cos(x)(4\cos(x)^2-3)(c-1)^3 + \dots \end{aligned} \quad (3.76)$$

Example values of  $c$  may be seen in Fig. 3.12. When the value of the constant is near one, the sum need only contain a small number of terms to express the function with a minimal degree of error, as seen in Fig. 3.13. The value of the constant in this case is seen in Eq. 3.77.

Note how the value of  $c$  is solely dependent upon the inertia.

$$c = \frac{I_y \beta}{I_x \alpha} \quad (3.77)$$

$$= \frac{I_x - \epsilon}{I_x} \left[ 1 + \frac{2I_x - I_z}{2I_x(I_x - I_z)} \epsilon + \dots \right] \quad (3.78)$$

Applying the inverse tangent model to Eq. 3.74 forms Eq. 3.79.

$$\tilde{\psi}(t) = \tan^{-1} \left( \frac{sn(pt, k)}{cn(pt, k)} \right) + sn(pt, k)cn(pt, k)(c-1) + \dots \quad (3.79)$$

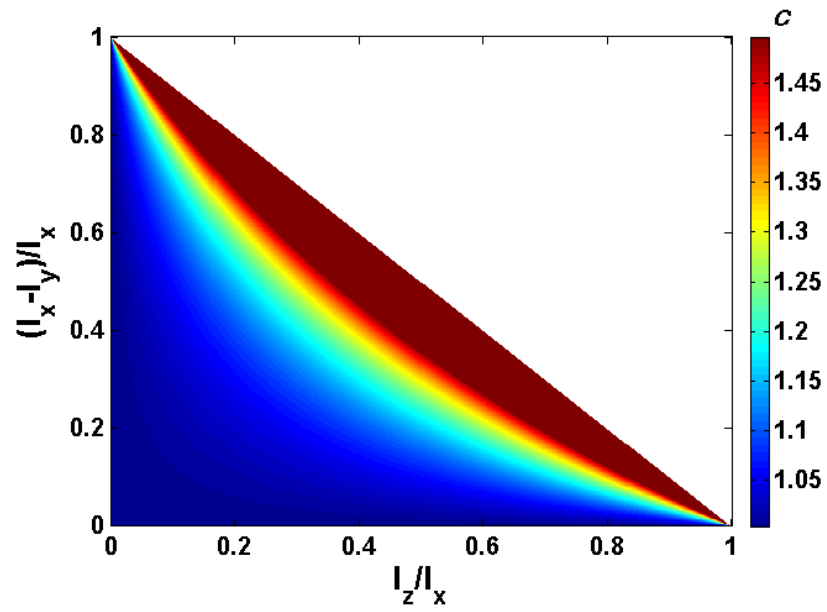


Figure 3.12: Values of  $c$  for various inertia. Most values of interest lie between 1 and 1.1

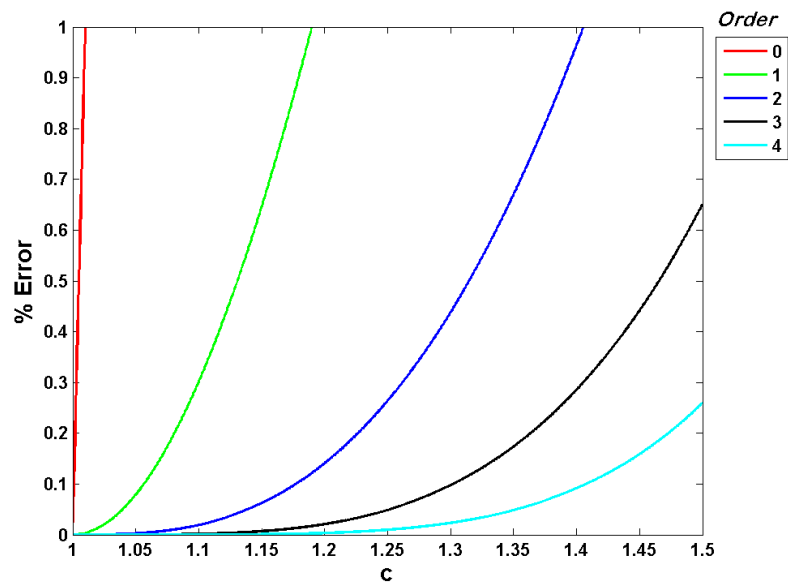


Figure 3.13: Error in  $\tan^{-1}$  model

As seen in Eq. 3.80, The inverse tangent of the Jacobi sinusoid ratio returns its argument, the Jacobi Amplitude function.

$$\begin{aligned} \tilde{\psi}(t) &= \tilde{A}(pt, k) \\ &+ \tilde{s}\tilde{n}(pt, k)\tilde{c}\tilde{n}(pt, k) \left( \frac{(I_x - \epsilon)}{I_x} \left[ 1 + \frac{2I_x - I_z}{2I_x(I_x - I_z)}\epsilon + \dots \right] - 1 \right) + \dots \end{aligned} \quad (3.80)$$

To see the three term representation, the Jacobi Amplitude function's linear portion may again be expanded about  $\frac{1}{\mathbf{K}(k)}$  for small  $k$ , as we did to arrive at Eq. 3.66. This function contains the component an axially symmetric body would generate, a small linear term, and a periodic term split into two components. The first component was contributed by the Jacobi Amplitude function, while the second component was contributed by the inverse tangent model.

$$\begin{aligned} \tilde{\psi}(t) &= \underbrace{\underbrace{pt}_{I_x=I_y}}_{\text{linear}} - \underbrace{pt \left( \frac{k^2}{4} + \frac{5k^6}{64} + \dots \right)}_{\text{linear}} + \underbrace{\frac{(2\mathbf{K}(k) - \pi)}{2\pi} \sin \left( \frac{pt\pi}{\mathbf{K}(k)} \right)}_{\text{periodic}} \\ &+ \underbrace{\tilde{s}\tilde{n}(pt, k)\tilde{c}\tilde{n}(pt, k) \left( \frac{(I_x - \epsilon)}{I_x} \left[ 1 + \frac{2I_x - I_z}{2I_x(I_x - I_z)}\epsilon + \dots \right] - 1 \right)}_{\text{periodic}} + \dots \end{aligned} \quad (3.81)$$

There is still a dominant linear term in the rotations contributing to average rotation rates. These average precession and spin rates may be seen in Eq. 3.82 and Eq. 3.83 respectively.

$$\omega_\phi = \frac{h}{I_x} - \frac{h(I_x - I_z)(\pi + \pi r - 2\mathbf{K}(k))}{2I_x I_z \mathbf{K}(k)} \quad (3.82)$$

$$\omega_\psi = \frac{p\pi}{2\mathbf{K}(k)} \quad (3.83)$$

### 3.4 Modulation Structure

The range function of a tracked scatterer may be analyzed using frequency decomposition techniques. One finds that the asymmetric free body range functions have the structure of an amplitude and frequency modulated signal. Furthermore, when the target has axially symmetry there exists only the structure of an amplitude modulated (AM) signal. This section will first present the simpler signal analysis of an axially symmetric target, followed by the analysis of an asymmetric target.

### 3.4.1 Axially Symmetric Target

The range function  $r_k$  generated by a scatterer on a force-free, rotating, axially symmetric target may be expressed in terms of an AM signal. The sinusoid functions may be reorganized to make clear the contributions of each frequency found in the spectrum. An example RTI and angular frequency spectrum may be seen in Fig. 3.14 and Fig. 3.15 respectively. The motion of the scatterers in the RTI was generated using the motion equations developed in Chapter 2. This angular frequency spectrum is of the tracked scatterer  $r_3$ . The spectrum plots contain values of the amplitude of a FFT with blue lines connecting the points. A rectangle window was applied to the range function data before spectral analysis. Only the positive frequencies are shown as the negative frequencies are simply their conjugated values mirrored about DC. Modern Spectral Analysis amplitude estimates are overlaid on the plot as red dots.

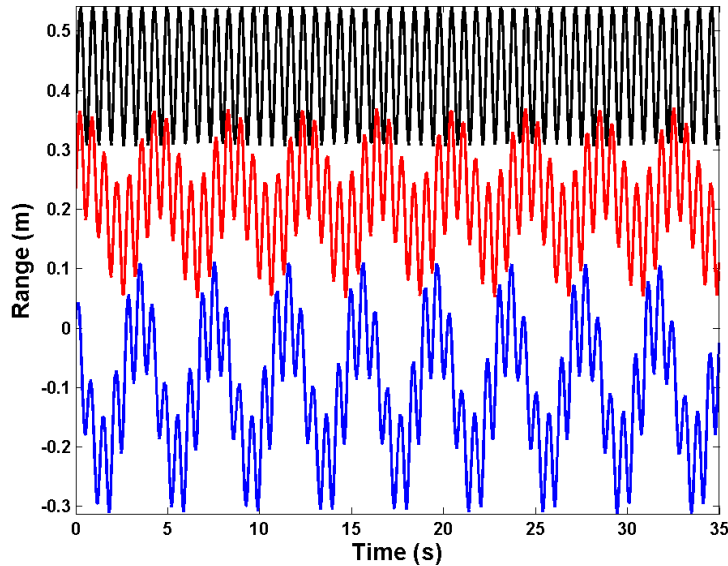


Figure 3.14: RTI:  $\bar{I} = [150.0, 150.0, 10.0]$ ,  $\bar{\omega} = [1.0, 1.0, 10.0]$ ,  $p_1 = [0.00, 0.00, 1.00]$  (black),  $p_2 = [0.05, 0.05, 0.50]$  (red),  $p_3 = [0.10, -0.10, -0.25]$  (blue)

The range function of the  $m^{th}$  scatterer may be seen in Eq. 3.84. The precession  $\phi$  and

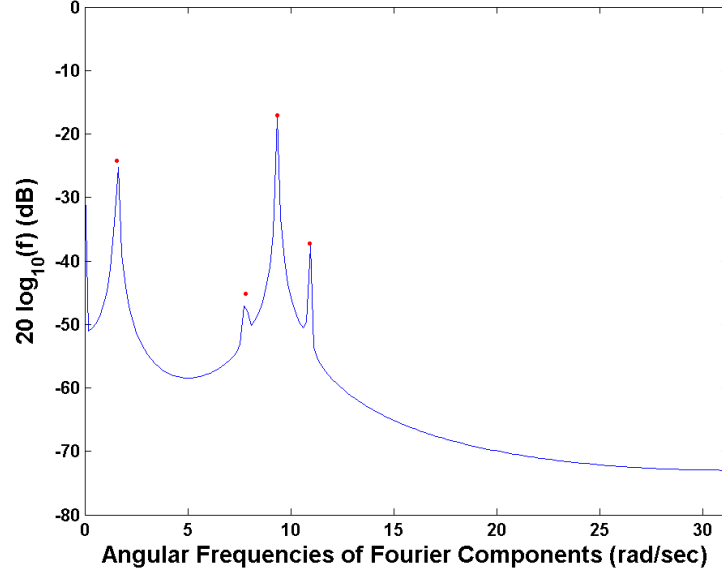


Figure 3.15: Angular Frequency Spectrum of  $r_3(t)$  :  $\bar{I} = [150.0, 150.0, 10.0]$ ,  $\bar{\omega} = [1.0, 1.0, 10.0]$ . The red dots are the MSA result; the blue curve is the Fourier Result.

spin  $\psi$  are linear functions of time, whereas the nutation  $\theta$  is a constant.

$$\begin{aligned}
 r_m(t) = & (C_x x_m c_\theta c_\phi + C_y y_m c_\phi + C_y x_m c_\theta s_\phi - C_x y_m s_\phi) c_\psi \\
 & + (-C_x y_m c_\theta c_\phi + C_y x_m c_\phi - C_y y_m c_\theta s_\phi - C_x x_m s_\phi) s_\psi \\
 & - C_z x_m s_\theta c_\psi + C_z y_m s_\theta s_\psi + C_x z_m s_\theta c_\phi + C_y z_m s_\theta s_\phi + C_z z_m c_\theta \quad (3.84)
 \end{aligned}$$

As seen in Eq. 3.85, the range of the  $m^{\text{th}}$  scatterer may be written in terms of scaled sine and cosine components.

$$\begin{aligned}
 r_m(t) = & (\kappa_0 c_\phi + \kappa_1 s_\phi) c_\psi + (\kappa_2 c_\phi + \kappa_3 s_\phi) s_\psi \\
 & + \kappa_4 c_\psi + \kappa_5 s_\psi + \kappa_6 c_\phi + \kappa_7 s_\phi + \kappa_8 \quad (3.85)
 \end{aligned}$$

Each of the scale factors, shown in Eq. 3.86 through Eq. 3.94, may be written in terms of the scatterer position  $(x_m, y_m, z_m)$ , the Radar LoS vector  $(C_x, C_y, C_z)$  and the fixed nutation

angle ( $\theta$ ).

$$\kappa_0 = C_x x_m c_\theta + C_y y_m \quad (3.86)$$

$$\kappa_1 = C_y x_m c_\theta - C_x y_m \quad (3.87)$$

$$\kappa_2 = -C_x y_m c_\theta + C_y x_m \quad (3.88)$$

$$\kappa_3 = -C_y y_m c_\theta - C_x x_m \quad (3.89)$$

$$\kappa_4 = -C_z x_m s_\theta \quad (3.90)$$

$$\kappa_5 = C_z y_m s_\theta \quad (3.91)$$

$$\kappa_6 = C_x z_m s_\theta \quad (3.92)$$

$$\kappa_7 = C_y z_m s_\theta \quad (3.93)$$

$$\kappa_8 = C_z z_m c_\theta \quad (3.94)$$

$$(3.95)$$

The sine and cosine functions may be transformed into cosines with phase shifts using a trigonometry property shown in Eq. 3.96[30].

$$A \cos(x) + B \sin(x) = \sqrt{A^2 + B^2} \cos\left(x - \tan^{-1}\left(\frac{B}{A}\right)\right) \quad (3.96)$$

Applying this property to Eq. 3.85 produces Eq. 3.97.

$$\begin{aligned} r_m(t) &= \sqrt{\kappa_0^2 + \kappa_1^2} \cos\left(\phi(t) - \tan^{-1}\left(\frac{\kappa_1}{\kappa_0}\right)\right) \cos(\psi(t)) \\ &+ \sqrt{\kappa_2^2 + \kappa_3^2} \cos\left(\phi(t) - \tan^{-1}\left(\frac{\kappa_3}{\kappa_2}\right)\right) \sin(\psi(t)) \\ &+ \sqrt{\kappa_4^2 + \kappa_5^2} \cos\left(\phi(t) - \tan^{-1}\left(\frac{\kappa_5}{\kappa_4}\right)\right) \\ &+ \sqrt{\kappa_6^2 + \kappa_7^2} \cos\left(\psi(t) - \tan^{-1}\left(\frac{\kappa_7}{\kappa_6}\right)\right) + \kappa_8 \end{aligned} \quad (3.97)$$

The final result is in the form of an Amplitude Modulated (AM) signal with additional unmodulated carrier signals,  $\cos(\psi(t))$  and  $\cos(\phi(t))$ , and a DC component,  $\kappa_8$ .

$$\begin{aligned} r_m(t) &= \kappa_{01} \cos(\phi(t) + \varphi_{01}) \cos(\psi(t)) \\ &+ \kappa_{23} \cos(\phi(t) + \varphi_{23}) \sin(\psi(t)) \end{aligned} \quad (3.98)$$

$$\begin{aligned} &+ \kappa_{45} \cos(\phi(t) + \varphi_{45}) \\ &+ \kappa_{67} \cos(\psi(t) + \varphi_{67}) + \kappa_8 \end{aligned} \quad (3.99)$$

Eq. 3.100 through Eq. 3.107 show  $\kappa_{01}$ ,  $\kappa_{23}$ ,  $\kappa_{45}$  and  $\kappa_{67}$ .

$$\kappa_{01} = \sqrt{\kappa_0^2 + \kappa_1^2} \quad (3.100)$$

$$= \sqrt{(C_x x_m c_\theta + C_y y_m)^2 + (C_y x_m c_\theta - C_x y_m)^2} \quad (3.101)$$

$$\kappa_{23} = \sqrt{\kappa_2^2 + \kappa_3^2} \quad (3.102)$$

$$= \sqrt{(-C_x y_m c_\theta + C_y x_m)^2 + (-C_y y_m c_\theta - C_x x_m)^2} \quad (3.103)$$

$$\kappa_{45} = \sqrt{\kappa_4^2 + \kappa_5^2} \quad (3.104)$$

$$= \sqrt{(-C_z x_m s_\theta)^2 + (C_z y_m s_\theta)^2} \quad (3.105)$$

$$\kappa_{67} = \sqrt{\kappa_6^2 + \kappa_7^2} \quad (3.106)$$

$$= \sqrt{(C_x z_m s_\theta)^2 + (C_y z_m s_\theta)^2} \quad (3.107)$$

Eq. 3.108 through Eq. 3.117 show simplifications of  $\varphi_{01}$ ,  $\varphi_{23}$ ,  $\varphi_{45}$  and  $\varphi_{67}$ .

$$\varphi_{01} = -\tan^{-1} \left( \frac{\kappa_1}{\kappa_0} \right) \quad (3.108)$$

$$= -\tan^{-1} \left( \frac{C_y x_m c_\theta - C_x y_m}{C_x x_m c_\theta + C_y y_m} \right) \quad (3.109)$$

$$\varphi_{23} = -\tan^{-1} \left( \frac{\kappa_3}{\kappa_2} \right) \quad (3.110)$$

$$= -\tan^{-1} \left( \frac{-C_y y_m c_\theta - C_x x_m}{-C_x y_m c_\theta + C_y x_m} \right) \quad (3.111)$$

$$\varphi_{45} = -\tan^{-1} \left( \frac{\kappa_5}{\kappa_4} \right) \quad (3.112)$$

$$= -\tan^{-1} \left( \frac{C_z y_m s_\theta}{-C_z x_m s_\theta} \right) \quad (3.113)$$

$$= -\tan^{-1} \left( \frac{y_m}{-x_m} \right) \quad (3.114)$$

$$\varphi_{67} = -\tan^{-1} \left( \frac{\kappa_7}{\kappa_6} \right) \quad (3.115)$$

$$= -\tan^{-1} \left( \frac{C_y z_m s_\theta}{C_x z_m s_\theta} \right) \quad (3.116)$$

$$= -\tan^{-1} \left( \frac{C_y}{C_x} \right) \quad (3.117)$$



A trigonometric property shown in Eq. 3.118 and Eq. 3.120 illuminates the occurrence of two frequencies from the sinusoid products[31].

$$c_1 \cos(x) \cos(y) = \frac{c_1 \cos(x-y)}{2} + \frac{c_2 \cos(x+y)}{2} \quad (3.118)$$

$$= \frac{c_1}{4} e^{j(x+y)} + \frac{c_1}{4} e^{j(x-y)} + \frac{c_1}{4} e^{j(y-x)} + \frac{c_1}{4} e^{-j(x+y)} \quad (3.119)$$

$$c_2 \sin(x) \cos(y) = \frac{c_2 \sin(x-y)}{2} + \frac{c_2 \sin(x+y)}{2} \quad (3.120)$$

$$= \frac{c_2}{4j} e^{j(x+y)} + \frac{c_2}{4j} e^{j(x-y)} - \frac{c_2}{4j} e^{j(y-x)} - \frac{c_2}{4j} e^{-j(x+y)} \quad (3.121)$$

The sinusoid product portion of the signal produces a spectrum containing two positive frequencies as seen in Eq. 3.122 and Eq. 3.123, with amplitudes seen in Eq. 3.124 and Eq. 3.125.

$$\omega_1 = \omega_\psi - \omega_\phi \quad (3.122)$$

$$\omega_2 = \omega_\psi + \omega_\phi \quad (3.123)$$

$$A_1 = \frac{\sqrt{\kappa_{01}^2 + \kappa_{23}^2}}{4} e^{j(\varphi_{01} + \varphi_{23} - \tan^{-1}(\frac{\kappa_{23}}{\kappa_{01}}))} \quad (3.124)$$

$$A_2 = \frac{\sqrt{\kappa_{01}^2 + \kappa_{23}^2}}{4} e^{j(\varphi_{01} - \varphi_{23} - \tan^{-1}(\frac{\kappa_{23}}{\kappa_{01}}))} \quad (3.125)$$

The additional carriers produce positive frequencies found in Eq. 3.126 and Eq. 3.127, with amplitudes seen in Eq. 3.128 and Eq. 3.129

$$\omega_3 = \omega_\phi \quad (3.126)$$

$$\omega_4 = \omega_\psi \quad (3.127)$$

$$A_3 = \kappa_{45} e^{j\varphi_{45}} \quad (3.128)$$

$$A_4 = \kappa_{67} e^{j\varphi_{67}} \quad (3.129)$$

This characterization of the frequency spectrum is important because it allows us to identify amplitude contributions useful for parameter estimation. Example spectra may be seen in Fig. 3.16 and Fig. 3.17. Both spectra were created using the same axially symmetric target,  $\bar{I} = [150, 150, 10]$ , but with different initial angular velocities. Fig. 3.16 shows a spectrum with the target spinning six times faster than it is precessing, while Fig. 3.17 shows one with the target spinning only slightly faster than it is precessing.

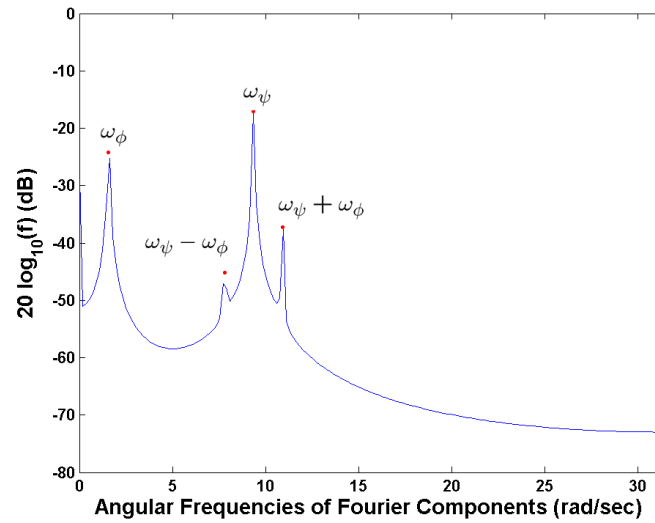


Figure 3.16: Angular Frequency Spectrum of  $r_3(t)$  :  $\bar{I} = [150.0, 150.0, 10.0]$ ,  $\bar{\omega} = [1.0, 1.0, 10.0]$ ,  $f_s = 10$ ,  $t = 35$ . The red dots are the MSA result; the blue curve is the FFT Result.

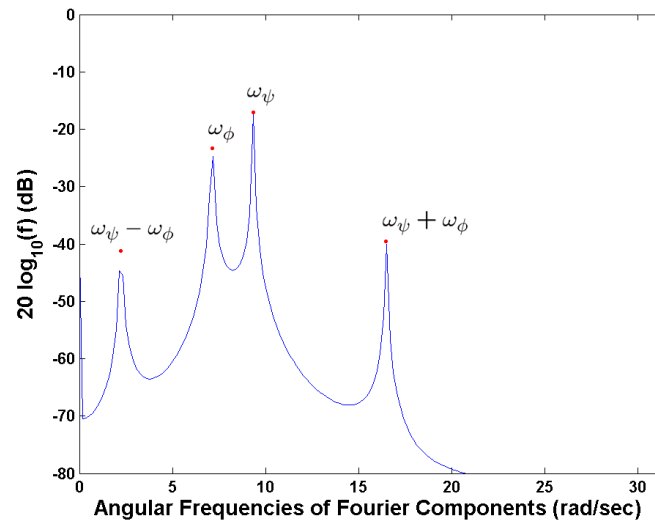


Figure 3.17: Angular Frequency Spectrum of  $r_3(t)$  :  $\bar{I} = [150.0, 150.0, 10.0]$ ,  $\bar{\omega} = [5.0, 5.0, 10.0]$ ,  $f_s = 10$ ,  $t = 35$ . The red dots are the MSA result; the blue curve is the FFT Result.

### 3.4.2 Nearly Symmetric Target

The periodic rotation components of the nearly symmetric model contribute additional frequency components when evaluated in the range function of Eq. 3.130. The time dependency of  $\psi$ ,  $\phi$ , and  $\theta$  is suppressed to shorten the notation.

$$\begin{aligned}
r_m(t) = & C_x x_m c_\theta c_\psi c_\phi + C_y x_m c_\theta c_\psi s_\phi - C_z x_m c_\psi s_\theta - C_x x_m s_\psi s_\phi + C_y x_m s_\psi c_\phi \\
& - C_x y_m c_\theta s_\psi c_\phi - C_y y_m c_\theta s_\psi s_\phi + C_z y_m s_\theta s_\psi - C_x y_m c_\psi s_\phi + C_y y_m c_\psi c_\phi \\
& + C_x z_m s_\theta c_\phi + C_y z_m s_\theta s_\phi + C_z z_m c_\theta
\end{aligned} \tag{3.130}$$

Each additional sinusoidal component and its frequency can be traced back to the particular terms and functions in Eq. 3.130 which generated it. To aid in the identification process, similar terms in the rotation function are assigned a number, as found in Eq. 3.131 and Table 3.1. Each number represents a particular combination of spin, nutation, and precession sinusoid evaluations. For the purpose of illustrating the frequency contribution independent of the Radar line of sight and scatterer positions, the scalars in each rotation component, identified in Table 3.1, shall suppressed.

$$\begin{aligned}
r_m(t) = & C_y y_m c_\psi c_\phi - C_x y_m c_\psi s_\phi + C_y x_m s_\psi c_\phi - C_x x_m s_\psi s_\phi \longrightarrow 1 \\
& + C_x x_m c_\theta c_\psi c_\phi + C_y x_m c_\theta c_\psi s_\phi - C_x y_m c_\theta s_\psi c_\phi - C_y y_m c_\theta s_\psi s_\phi \longrightarrow 2 \\
& - C_z x_m s_\theta c_\psi + C_z y_m s_\theta s_\psi \longrightarrow 3 \\
& + C_x z_m s_\theta c_\phi + C_y z_m s_\theta s_\phi \longrightarrow 4 \\
& + C_z z_m c_\theta \longrightarrow 5
\end{aligned}$$

The examples in this section show angular velocity spectra of signals which have been sampled for an extended time period to fully resolve each frequency component. The signals were constructed to have a spin rate  $\omega_\psi$  of  $10 \frac{rad}{s}$  and a precession rate  $\omega_\phi$  of  $1 \frac{rad}{s}$ . Various other motion parameters used for the examples in this section may be seen in Eq. 3.131 through Eq. 3.133.

$$\kappa_\theta = 0.5 \tag{3.131}$$

$$c = 1.25 \tag{3.132}$$

$$r = -0.08 \tag{3.133}$$

Table 3.1: Rotation Terms

Term #	Scalars	Sinusoid Products
1	$+C_y y_m$	$c_\psi c_\phi$
	$-C_x y_m$	$c_\psi s_\phi$
	$+C_y x_m$	$s_\psi c_\phi$
	$-C_x x_m$	$s_\psi s_\phi$
2	$+C_x x_m$	$c_\theta c_\psi c_\phi$
	$+C_y x_m$	$c_\theta c_\psi s_\phi$
	$-C_x y_m$	$c_\theta s_\psi c_\phi$
	$-C_y y_m$	$c_\theta s_\psi s_\phi$
3	$-C_z x_m$	$s_\theta c_\psi$
	$+C_z y_m$	$s_\theta s_\psi$
4	$+C_x z_m$	$s_\theta c_\phi$
	$+C_y z_m$	$s_\theta s_\phi$
5	$+C_z z_m$	$c_\theta$

Fig. 3.18 shows a plot of the angular frequency spectrum for this target. Note that in addition to the four positive frequencies found in the case of an axially symmetric target, there are seventeen additional positive frequencies found in this example. It is the intention of the following sections to identify the origin of each of these additional frequencies.

### Frequency Modulation Formulation

Before proceeding to the frequency identification, the precession and spin may be written in a form that is appropriate for such analysis. They may each be written as linear rates with sinusoidal perturbations composed of harmonics of the spin rate. This means that the cosine and sine of these rotations take the form of Frequency Modulated (FM) signals. The reorganization of each function required to obtain this form is now performed.

The first step to reorganizing the precession, as seen in Eq. 3.134, to fit this form involves

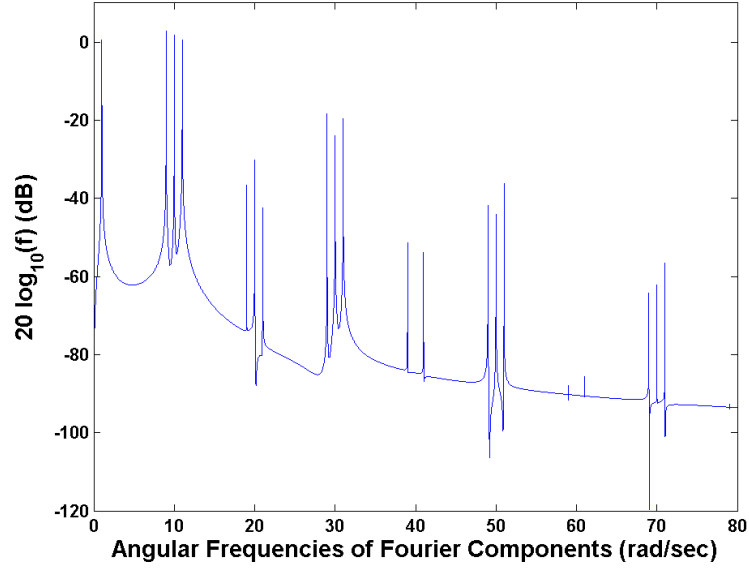


Figure 3.18: Angular Frequency Spectrum: All terms,  $\omega_\psi = 10$ ,  $\omega_\phi = 1$ ,  $f_s = 80$ ,  $t = 2000$

revisiting the elliptic integral approximation.

$$\phi(t) = \frac{h(I_x - I_z)}{pI_x I_z} \mathbf{\Pi}(sn(pt, k), n, k) - \frac{ht}{I_z} \quad (3.134)$$

To simplify notation, the scalars to the left of the elliptic integral will be grouped as one variable,  $a_0$ .

$$a_0 = \frac{h(I_x - I_z)}{pI_x I_z} \quad (3.135)$$

$$\phi(t) = a_0 \mathbf{\Pi}(sn(pt, k), n, k) - \frac{ht}{I_z} \quad (3.136)$$

The elliptic integral approximation of Eq. 3.137 may be expanded to form Eq. 3.138.

$$\begin{aligned} \tilde{\mathbf{\Pi}}(\tilde{sn}(u, k), n, k) &= u(1+r) \frac{\pi}{2\mathbf{K}(k)} + (1+r) \frac{(2\mathbf{K}(k) - \pi)}{2\pi} \sin\left(\frac{u\pi}{\mathbf{K}(k)}\right) \\ &\quad - \left(r + \frac{3k^4 sn^2(u, k)}{32}\right) sn(u, k) cn(u, k) \end{aligned} \quad (3.137)$$

$$\begin{aligned} &= u(1+r) \frac{\pi}{2\mathbf{K}(k)} + (1+r) \frac{(2\mathbf{K}(k) - \pi)}{2\pi} \sin\left(\frac{u\pi}{\mathbf{K}(k)}\right) \\ &\quad - r sn(u, k) cn(u, k) - \frac{3k^4}{32} sn(u, k)^3 cn(u, k) \end{aligned} \quad (3.138)$$

The spin rate,  $\omega_\psi$ , will be used to simplify notation.

$$\omega_\psi = \frac{p\pi}{2\mathbf{K}(k)} \quad (3.139)$$

Due to its negligible impact on the frequency spectrum, the sinusoidal perturbation factor found within the Jacobi sinusoids is suppressed.

$$sn(pt, k) = \sin\left(\omega_\psi t + \frac{2\mathbf{K}(k) - \pi}{2\pi} \sin(2\omega_\psi t)\right) \quad (3.140)$$

$$= \sin(\omega_\psi t) \quad (3.141)$$

Applying the changes of Eq. 3.138 and Eq. 3.141 to Eq. 3.134 forms Eq. 3.142.

$$\begin{aligned} \tilde{\phi}(t) &= \frac{-ht}{I_z} + a_0\omega_\psi t(1+r) \\ &+ a_0((1+r)\frac{(2\mathbf{K}(k) - \pi)}{2\pi} \sin(2\omega_\psi t)) \\ &- a_0(r \sin(\omega_\psi t) \cos(\omega_\psi t) - \frac{3k^4}{32} \sin(\omega_\psi t)^3 \cos(\omega_\psi t)) \end{aligned} \quad (3.142)$$

The sinusoid products found in Eq. 3.142 may be simplified using the trigonometric properties found in Eq. 3.143 and Eq. 3.144.

$$\sin(x) \cos(x) = \frac{\sin(2x)}{2} \quad (3.143)$$

$$\sin(x)^3 \cos(x) = \frac{\sin(2x)}{4} - \frac{\sin(4x)}{8} \quad (3.144)$$

For simplified notation, the precession rate may be written as seen in Eq. 3.145

$$\omega_\phi = \frac{-h}{I_z} + \frac{h\pi(I_x - I_z)(1+r)}{2I_x I_z \mathbf{K}(k)} \quad (3.145)$$

The scalars which multiply the sinusoidal components may be represented as  $\beta_{\phi_0}$  and  $\beta_{\phi_1}$  such that  $\tilde{\phi}(t)$  may be represented in the simplified form of Eq. 3.146.

$$\tilde{\phi}(t) = \omega_\phi t + \beta_{\phi_0} \sin(2\omega_\psi t) + \beta_{\phi_1} \sin(4\omega_\psi t) \quad (3.146)$$

$$\beta_{\phi_0} = \frac{h(I_x - I_z)}{pI_x I_z} \left( \frac{(2\mathbf{K}(k) - \pi)(1+r)}{2\pi} - \frac{3k^4}{128} \right) \quad (3.147)$$

$$\beta_{\phi_1} = \frac{h(I_x - I_z)}{pI_x I_z} \left( \frac{-r}{2} + \frac{3k^4}{256} \right) \quad (3.148)$$

The functions seen in Eq. 3.149 and Eq. 3.150 are both in the form of frequency modulated signals with a carrier frequency of  $\omega_\phi$ , modulation frequencies of  $2\omega_\psi$  and  $4\omega_\psi$ , and modulation indices of  $\beta_0$  and  $\beta_1$ .

$$\sin(\tilde{\phi}(t)) = \sin(\omega_\phi t + \beta_{\phi_0} \sin(2\omega_\psi t) + \beta_{\phi_1} \sin(4\omega_\psi t)) \quad (3.149)$$

$$\cos(\tilde{\phi}(t)) = \cos(\omega_\phi t + \beta_{\phi_0} \sin(2\omega_\psi t) + \beta_{\phi_1} \sin(4\omega_\psi t)) \quad (3.150)$$

The spin, as seen in Eq. 3.151, may be reorganized into the desired FM form by revisiting the inverse tangent approximation.

$$\begin{aligned} \tilde{\psi}(t) &= \tilde{A}(pt, k) \\ &+ \tilde{s}\tilde{n}(pt, k)\tilde{c}\tilde{n}(pt, k) \left( \frac{(I_x - \epsilon)}{I_x} \left[ 1 + \frac{2I_x - I_z}{2I_x(I_x - I_z)}\epsilon + \dots \right] - 1 \right) + \dots \end{aligned} \quad (3.151)$$

The sinusoid products of Eq. 3.152 may be rewritten as sums of scaled sinusoids at different frequencies. This is illustrated by applying the trigonometric properties of Eq. 3.143 and Eq. 3.144 to Eq. 3.152 thus forming Eq. 3.153.

$$\begin{aligned} \tan^{-1}(\tan(x)c) &= x + \sin(x)\cos(x)(c-1) - \sin(x)^3\cos(x)(c-1)^2 \\ &\quad - \frac{1}{3}\sin(x)^3\cos(x)(4\cos(x)^2 - 3)(c-1)^3 + \dots \quad (3.152) \\ &= x + \frac{\sin(2x)(c-1)}{2} \\ &\quad + \frac{(-2\sin(2x) + \sin(4x))(c-1)^2}{8} \\ &\quad + \frac{(3\sin(2x) - 3\sin(4x) + \sin(6x))(c-1)^3}{24} + \dots \quad (3.153) \end{aligned}$$

As shown in Eq. 3.154, Eq. 3.153 may be written in a form that emphasizes each of the sinusoid components occurring at unique frequencies.

$$\begin{aligned} \tan^{-1}(\tan(x)c) &= x + \left( \frac{(c-1)}{2} - \frac{(c-1)^2}{4} + \frac{(c-1)^3}{8} + \dots \right) \sin(2x) \\ &\quad + \left( \frac{(c-1)^2}{8} + \frac{(c-1)^3}{8} + \dots \right) \sin(4x) \\ &\quad + \left( \frac{(c-1)^3}{24} + \dots \right) \sin(6x) + \dots \quad (3.154) \end{aligned}$$

This formulation of the inverse tangent may be substituted into the spin function to

produce Eq. 3.154.

$$\begin{aligned}
\psi(t) &= \omega_\psi t + \frac{2\mathbf{K}(k) - \pi}{2\pi} \sin(2\omega_\psi t) \\
&+ \left( \frac{(c-1)}{2} - \frac{(c-1)^2}{4} + \frac{(c-1)^3}{8} + \dots \right) \sin \left( 2\omega_\psi t + \frac{2\mathbf{K}(k) - \pi}{2\pi} \sin(4\omega_\psi t) \right) \\
&+ \left( \frac{(c-1)^2}{8} + \frac{(c-1)^3}{8} + \dots \right) \sin \left( 4\omega_\psi t + \frac{2\mathbf{K}(k) - \pi}{2\pi} \sin(8\omega_\psi t) \right) \\
&+ \left( \frac{(c-1)^3}{24} + \dots \right) \sin \left( 6\omega_\psi t + \frac{2\mathbf{K}(k) - \pi}{2\pi} \sin(12\omega_\psi t) \right) + \dots
\end{aligned} \tag{3.155}$$

For a nearly symmetric target, the value of  $c$  is below 1.5. Thus, for the purpose of the modulation analysis, an order 3 inverse tangent approximation will be used. The analysis may be done with higher order terms without introducing additional complexity, although the number of modulation frequencies becomes cumbersome. Again, due to its negligible impact on the frequency spectrum, the sinusoidal perturbation factor found within the Jacobi sinusoids is suppressed. The simplified result may be seen in Eq. 3.156.

$$\begin{aligned}
\tilde{\psi}(t) &= \omega_\psi t + \frac{2\mathbf{K}(k) - \pi}{2\pi} \sin(2\omega_\psi t) \\
&+ \left( \frac{(c-1)}{2} - \frac{(c-1)^2}{4} + \frac{(c-1)^3}{8} \right) \sin(2\omega_\psi t) \\
&+ \left( \frac{(c-1)^2}{8} + \frac{(c-1)^3}{8} \right) \sin(4\omega_\psi t) \\
&+ \left( \frac{(c-1)^3}{24} \right) \sin(6\omega_\psi t)
\end{aligned} \tag{3.156}$$

Similarly to the precession case, the scalars which multiply the FM components may be represented as  $\beta_{\psi_0}$ ,  $\beta_{\psi_1}$ , and  $\beta_{\psi_2}$  such that  $\tilde{\psi}(t)$  may be represented in the simplified form of Eq. 3.157.

$$\tilde{\psi}(t) = \omega_\psi t + \beta_{\psi_0} \sin(2\omega_\psi t) + \beta_{\psi_1} \sin(4\omega_\psi t) + \beta_{\psi_2} \sin(6\omega_\psi t) \tag{3.157}$$

$$\beta_{\psi_0} = \frac{2\mathbf{K}(k) - \pi}{2\pi} + \frac{(c-1)}{2} - \frac{(c-1)^2}{4} + \frac{(c-1)^3}{8} \tag{3.158}$$

$$\beta_{\psi_1} = \frac{(c-1)^2}{8} + \frac{(c-1)^3}{8} \tag{3.159}$$

$$\beta_{\psi_2} = \frac{(c-1)^3}{24} \tag{3.160}$$

The functions seen in Eq. 3.161 and Eq. 3.162 are both in the form of frequency modulated signals with a carrier frequency of  $\omega_\psi$  and modulation frequencies of  $2\omega_\psi$ ,  $4\omega_\psi$ , and



$6\omega_\psi$ .

$$\sin(\tilde{\psi}(t)) = \sin(\omega_\psi t + \beta_{\psi_0} \sin(2\omega_\psi t) + \beta_{\psi_1} \sin(4\omega_\psi t) + \beta_{\psi_2} \sin(6\omega_\psi t)) \quad (3.161)$$

$$\cos(\tilde{\psi}(t)) = \cos(\omega_\psi t + \beta_{\psi_0} \sin(2\omega_\psi t) + \beta_{\psi_1} \sin(4\omega_\psi t) + \beta_{\psi_2} \sin(6\omega_\psi t)) \quad (3.162)$$

Bessel functions may be introduced to represent the spin and precession as traditional FM signals[30]. Eq. 3.163 shows a FM signal, with a carrier frequency  $\omega_c$  and a modulation frequency  $\omega_0$ . The formulation of this function in terms of Bessel functions may be seen in Eq. 3.164. The  $n^{th}$  integer harmonic generated by this modulation has an amplitude specified by the Bessel function for a given  $\beta$  and index  $n$ . Fig. 3.19 shows the Bessel function evaluated for various input parameters. Note how as  $\beta$  decreases, the value near  $n = 0$  increases and the value for large  $n$  decreases.

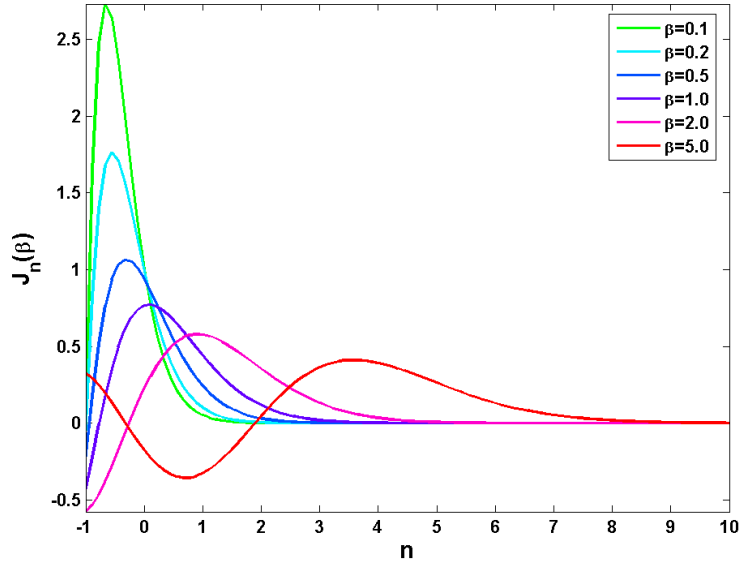


Figure 3.19: Bessel function of the first kind evaluated for various  $n$  and  $\beta$

$$e^{jf_1(t)} = e^{j(\omega_c t + \beta \sin(\omega_0 t))} \quad (3.163)$$

$$= \sum_{n=-\infty}^{\infty} J_n(\beta) e^{j(\omega_c t + n\omega_0 t)} \quad (3.164)$$

The Fourier Transform of Eq. 3.164, found in Eq. 3.165, possesses an infinite number of spectral line components located at  $\omega_c + n\omega_m$ .

$$\mathcal{F}\left\{e^{jf_1(t)}\right\} = 2\pi \sum_{n=-\infty}^{\infty} J_n(\beta) \delta(\omega - (\omega_c + n\omega_m)) \quad (3.165)$$

When there are multiple modulation frequencies, the signal may still be represented using Bessel functions. Each modulation frequency introduces an additional summation and modulation index constant  $\beta$ . An example with two modulation frequencies may be seen in Eq. 3.166 and Eq. 3.167

$$e^{jf_2(t)} = e^{j(\omega_c t + \beta_0 \sin(\omega_0 t) + \beta_1 \sin(\omega_1 t))} \quad (3.166)$$

$$= \sum_{n_0=-\infty}^{\infty} \sum_{n_1=-\infty}^{\infty} J_{n_0}(\beta_0) J_{n_1}(\beta_1) e^{j(\omega_c t + n_0 \omega_0 t + n_1 \omega_1 t)} \quad (3.167)$$

The Fourier Transform of Eq. 3.167, found in Eq. 3.168, possesses an infinite number of spectral line components located at  $\omega_c + n_0\omega_0 + n_1\omega_1$ .

$$\mathcal{F}\left\{e^{jf_2(t)}\right\} = 2\pi \sum_{n_0=-\infty}^{\infty} \sum_{n_1=-\infty}^{\infty} \alpha(n_0, n_1) \delta(\omega - (\omega_c + n_0\omega_0 + n_1\omega_1)) \quad (3.168)$$

$$\alpha(n_0, n_1) = J_{n_0}(\beta_0) J_{n_1}(\beta_1) \quad (3.169)$$

### Linear Rotation Components

The four positive frequency components generated by a rotating axially symmetric target are also found when analyzing a rotating asymmetric target. If the periodic portions of each rotation function are suppressed, these are the only visible frequency components. This can be seen in Fig. 3.20 where the four frequencies corresponding to the linear components are shown as a red trace overlaid on top of the complete spectrum in blue. Table 3.2 shows which sinusoid products contribute to the four frequencies. It associates a particular set or sets of these products as the generating function for each frequency or series of frequencies. The first column denotes which rotation term is contributing the frequency components. The first row denotes the frequency components of interest. An *X* denotes that the term in that row contributes a frequency component in that column.

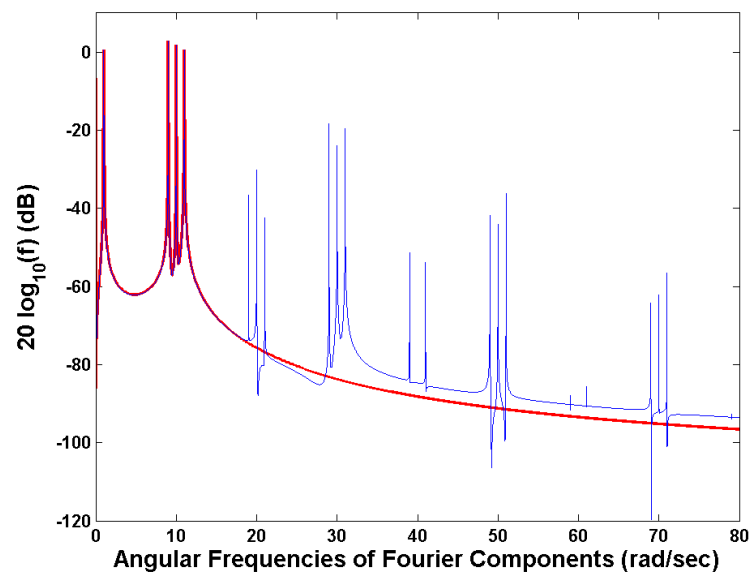


Figure 3.20: Angular Frequency Spectrum: Linear Components Only,  $\omega_\psi = 10$ ,  $\omega_\phi = 1$ ,  $f_s = 80$ ,  $t = 2000$ . The red trace is the linear component, the blue trace is composed of both linear and suppressed components. Frequencies are found at  $\omega_\phi$ ,  $\omega_\psi - \omega_\phi$ ,  $\omega_\psi$ , and  $\omega_\psi + \omega_\phi$

Table 3.2: Linear Component Angular Frequency Spectrum Contributions

	$\omega_\phi$	$\omega_\psi$	$\omega_\psi \pm \omega_\phi$	$DC$
1			X	
2			X	
3		X		
4	X			
5				X

### Precession Periodic Component

As seen in Fig. 3.21, the precession periodic component contributes harmonics of the spin rate plus or minus the precession rate. The generation of these components can be

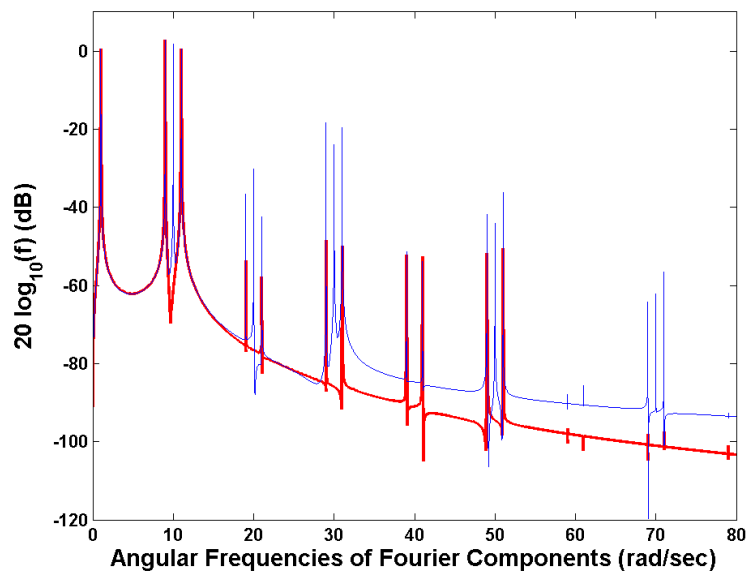


Figure 3.21: Angular Frequency Spectrum: Precession periodic component,  $r_m^{1,2,4}$ ,  $\omega_\psi = 10$ ,  $\omega_\phi = 1$ ,  $f_s = 80$ ,  $t = 2000$ . The precession periodic component adds frequencies at  $n\omega_\psi \pm \omega_\phi$

better understood by reviewing the contributing terms in greater detail. The superscripts  $1 \rightarrow 5$  signify the terms from the rotation function included from the range function  $r_m$ .

The 4<sup>th</sup> term, seen in Eq. 3.170 can be rewritten as having a single cosine of  $\phi(t)$ .

$$r_m^4(t) = C_x z_m s_\theta c_\phi + C_y z_m s_\theta s_\phi \quad (3.170)$$

$$= \kappa_{\phi_3} \cos(\phi(t)) + \kappa_{\phi_4} \sin(\phi(t)) \quad (3.171)$$

$$= \sqrt{\kappa_{\phi_3}^2 + \kappa_{\phi_4}^2} \cos\left(\phi(t) - \tan^{-1}\left(\frac{\kappa_{\phi_4}}{\kappa_{\phi_3}}\right)\right) \quad (3.172)$$

$$= \kappa_{\phi_{34}} \cos(\phi(t) + \varphi_{34}) \quad (3.173)$$

The amplitude and phase associated with the scalars of term 4 may be seen in Eq. 3.174 through Eq. 3.181.

$$\kappa_{\phi_3} = C_x z_m s_\theta \quad (3.174)$$

$$\kappa_{\phi_4} = C_y z_m s_\theta \quad (3.175)$$

$$\kappa_{\phi_{34}} = \sqrt{\kappa_{\phi_3}^2 + \kappa_{\phi_4}^2} \quad (3.176)$$

$$= \sqrt{(C_x z_m s_\theta)^2 + (C_y z_m s_\theta)^2} \quad (3.177)$$

$$= \sqrt{z_m^2 s_\theta^2 (C_x^2 + C_y^2)} \quad (3.178)$$

$$\varphi_{\phi_{34}} = -\tan^{-1}\left(\frac{\kappa_{\phi_4}}{\kappa_{\phi_3}}\right) \quad (3.179)$$

$$= -\tan^{-1}\left(\frac{C_y z_m s_\theta}{C_x z_m s_\theta}\right) \quad (3.180)$$

$$= -\tan^{-1}\left(\frac{C_y}{C_x}\right) \quad (3.181)$$

The additional components can be seen by expanding Eq. 3.173 to include  $\phi(t)$ .

$$r_m^4(t) = \kappa_{\phi_{34}} \cos(\phi(t) + \varphi_{34}) \quad (3.182)$$

$$= \kappa_{\phi_{34}} \cos(\omega_\phi t + \beta_{\phi_0} \sin(2\omega_\psi t) + \beta_{\phi_1} \sin(4\omega_\psi t) + \varphi_{34}) \quad (3.183)$$

The Fourier Transform of Eq. 3.183 may be seen in Eq. 3.184.

$$\mathcal{F}\{r_m^3(t)\} = \kappa_{\phi_{34}} \pi \sum_{n_0=-\infty}^{\infty} \sum_{n_1=-\infty}^{\infty} \alpha_\phi(n_0, n_1) \delta_\phi(n_0, n_1) \quad (3.184)$$

$$\alpha_\phi(n_0, n_1) = J_{n_0}(\beta_{\phi_0}) J_{n_1}(\beta_{\phi_0}) \quad (3.185)$$

$$\begin{aligned} \delta_\phi(n_0, n_1) &= e^{-j\varphi_{34}} \delta(\omega + \omega_\phi + 2n_0\omega_\psi + 4n_1\omega_\psi) \\ &\quad + e^{j\varphi_{34}} \delta(\omega - (\omega_\phi + 2n_0\omega_\psi + 4n_1\omega_\psi)) \end{aligned} \quad (3.186)$$

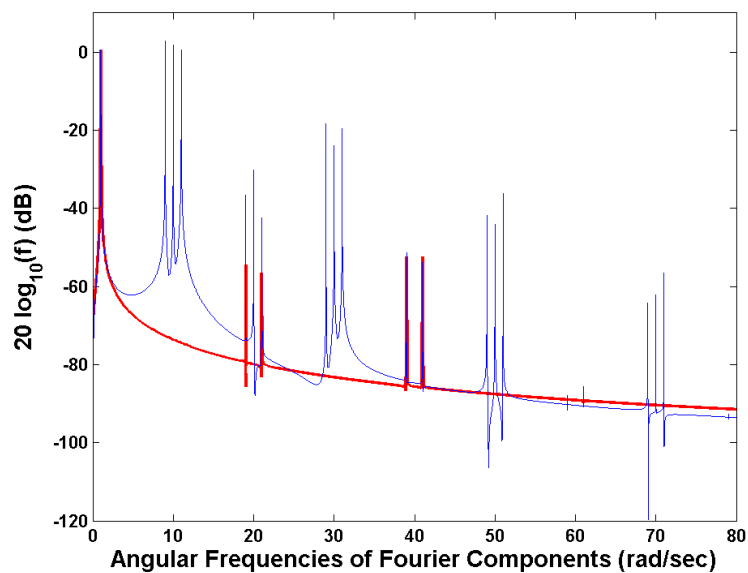


Figure 3.22: Angular Frequency Spectrum: Precession periodic component,  $r_m^4$ ,  $\omega_\psi = 10$ ,  $\omega_\phi = 1$ ,  $f_s = 80$ ,  $t = 2000$ . Additional frequencies:  $\omega_\phi(n_0 = 0, n_1 = 0)$ ,  $-\omega_\phi + 2\omega_\psi(n_0 = -1, n_1 = 0)$ ,  $\omega_\phi + 2\omega_\psi(n_0 = 1, n_1 = 0)$ ,  $-\omega_\phi + 4\omega_\psi(n_0 = -2, n_1 = 0; n_0 = 0, n_1 = -1)$ ,  $\omega_\phi + 4\omega_\psi(n_0 = 2, n_1 = 0; n_0 = 0, n_1 = 1)$ , etc.

The harmonics contributed by the precession FM component in term 4 may be seen in Fig. 3.22.

The first and second terms may be seen in Eq. 3.187.

$$\begin{aligned} r_m^{1,2}(t) = & -C_x y_m c_\psi s_\phi + C_y y_m c_\psi c_\phi - C_x x_m s_\psi s_\phi + C_y x_m s_\psi c_\phi \\ & + C_x x_m c_\theta c_\psi c_\phi + C_y x_m c_\theta c_\psi s_\phi - C_x y_m c_\theta s_\psi c_\phi - C_y y_m c_\theta s_\psi s_\phi \end{aligned} \quad (3.187)$$

As seen in Eq. 3.188, the scalars of each sinusoid product may be collected such that there are only four sinusoid products.

$$\begin{aligned} r_m^{1,2}(t) = & (C_y y_m - C_x x_m c_\theta) c_\psi c_\phi + (-C_x y_m + C_y x_m c_\theta) c_\psi s_\phi \\ & + (C_y x_m - C_x y_m c_\theta) s_\psi c_\phi + (-C_x x_m + C_y y_m c_\theta) s_\psi s_\phi \end{aligned} \quad (3.188)$$

The scalars may be represented in compressed notation as shown in Eq. 3.189 through Eq. 3.192.

$$\kappa_{p0} = (C_y y_m - C_x x_m c_\theta) \quad (3.189)$$

$$\kappa_{p1} = (-C_x y_m + C_y x_m c_\theta) \quad (3.190)$$

$$\kappa_{p2} = (C_y x_m - C_x y_m c_\theta) \quad (3.191)$$

$$\kappa_{p3} = (-C_x x_m + C_y y_m c_\theta) \quad (3.192)$$

Applying this notation to Eq. 3.188 produces Eq. 3.193.

$$\begin{aligned} r_m^{1,2}(t) = & \kappa_{p0} \cos(\psi(t)) \cos(\phi(t)) + \kappa_{p1} \cos(\psi(t)) \sin(\phi(t)) \\ & + \kappa_{p2} \sin(\psi(t)) \cos(\phi(t)) + \kappa_{p3} \sin(\psi(t)) \sin(\phi(t)) \end{aligned} \quad (3.193)$$

Expanding Eq. 3.193 to reveal the spin and precession terms produces Eq. 3.194.

$$\begin{aligned} r_m^{1,2}(t) = & \kappa_{p0} \cos(\omega_\phi t + \beta_{\phi_0} \sin(2\omega_\psi t) + \beta_{\phi_1} \sin(4\omega_\psi t)) \cos(\omega_\psi t) \\ & + \kappa_{p1} \sin(\omega_\phi t + \beta_{\phi_0} \sin(2\omega_\psi t) + \beta_{\phi_1} \sin(4\omega_\psi t)) \cos(\omega_\psi t) \\ & + \kappa_{p2} \cos(\omega_\phi t + \beta_{\phi_0} \sin(2\omega_\psi t) + \beta_{\phi_1} \sin(4\omega_\psi t)) \sin(\omega_\psi t) \\ & + \kappa_{p3} \sin(\omega_\phi t + \beta_{\phi_0} \sin(2\omega_\psi t) + \beta_{\phi_1} \sin(4\omega_\psi t)) \sin(\omega_\psi t) \end{aligned} \quad (3.194)$$

The frequency components of Eq. 3.194 may then be found by applying the Fourier Transform. The result may be seen in Eq. 3.195. It produces an infinite number of line contributions at the odd spin rate harmonic frequencies plus and minus the precession rate harmonic frequencies. The harmonics contributed by the precession FM component in terms 1 and 2 may be seen in Fig. 3.23.

$$\mathcal{F}\{r_m^{12}(t)\} = \frac{\pi}{2} \sum_{n_0=-\infty}^{\infty} \sum_{n_1=-\infty}^{\infty} \alpha_{\phi 12}(n_0, n_1) \delta_{\phi 12}(n_0, n_1) \quad (3.195)$$

$$\alpha_{\phi 12}(n_0, n_1) = J_{n_0}(\beta_{\phi_0}) J_{n_1}(\beta_{\phi_1}) \quad (3.196)$$

$$\begin{aligned} \delta_{\phi 12}(n_0, n_1) = & (\kappa_{p0} + j\kappa_{p1} + j\kappa_{p2} - \kappa_{p3}) \delta(\omega + \omega_{\psi} + \omega_{\phi} + 2n_0\omega_{\psi} + 4n_1\omega_{\psi}) \\ & (\kappa_{p0} - j\kappa_{p1} - j\kappa_{p2} - \kappa_{p3}) \delta(\omega - \omega_{\psi} - (\omega_{\phi} + 2n_0\omega_{\psi} + 4n_1\omega_{\psi})) \\ & (\kappa_{p0} - j\kappa_{p1} + j\kappa_{p2} + \kappa_{p3}) \delta(\omega - \omega_{\psi} + \omega_{\phi} + 2n_0\omega_{\psi} + 4n_1\omega_{\psi}) \\ & (\kappa_{p0} + j\kappa_{p1} - j\kappa_{p2} + \kappa_{p3}) \delta(\omega + \omega_{\psi} - (\omega_{\phi} + 2n_0\omega_{\psi} + 4n_1\omega_{\psi})) \end{aligned} \quad (3.197)$$

These harmonics and their generating functions are summarized in Table 3.3.

Table 3.3: Precession Periodic Component Angular Frequency Spectrum Contributions

	N/A	$[1, 3 \dots]\omega_{\psi} \pm \omega_{\phi}$	$[0, 2, \dots]\omega_{\psi} \pm \omega_{\phi}$
1		X	
2		X	
3	X		
4			X
5	X		



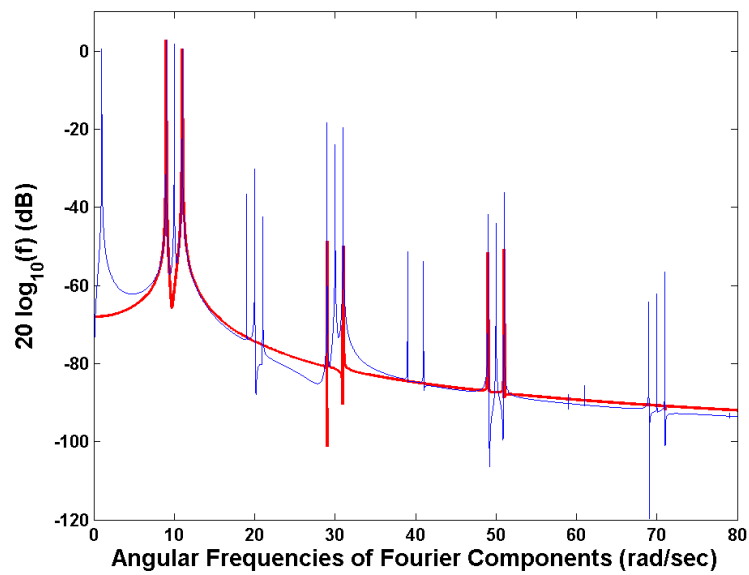


Figure 3.23: Angular Frequency Spectrum: Precession periodic component,  $r_m^{1,2}$ ,  $\omega_\psi = 10$ ,  $\omega_\phi = 1$ ,  $f_s = 80$ ,  $t = 2000$ , Additional frequencies:  $-\omega_\phi + \omega_\psi$ ,  $\omega_\phi + \omega_\psi$ ,  $-\omega_\phi + 2\omega_\psi + \omega_\psi$ ,  $\omega_\phi + 2\omega_\psi + \omega_\psi$ ,  $-\omega_\phi + 4\omega_\psi + \omega_\psi$ ,  $\omega_\phi + 4\omega_\psi + \omega_\psi$ , etc.

### Spin Periodic Component

The spin periodic component contributes two different sets of harmonics. The first harmonics are generated by term three. They occur at odd integer multiples of the spin rate. The other harmonics are generated by terms one and two. They occur at integer multiples of the spin rate plus and minus the precession rate. These harmonics may be seen in Fig. 3.24.

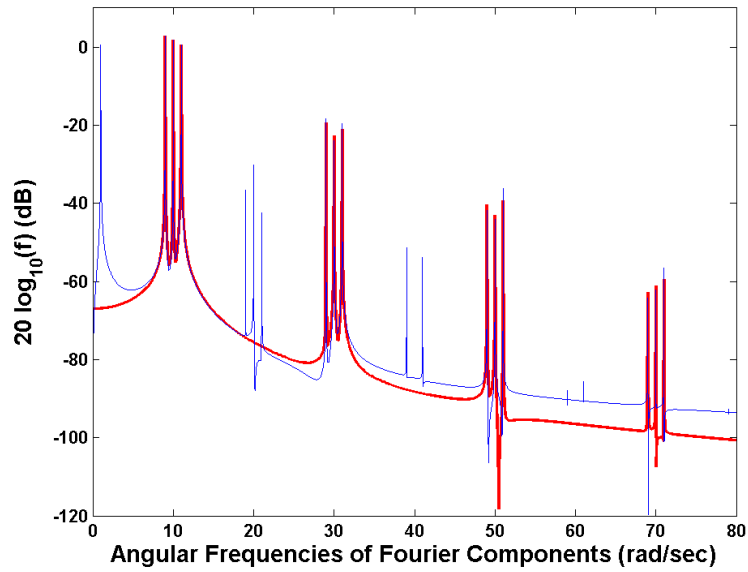


Figure 3.24: Angular Frequency Spectrum: Spin periodic component,  $r_m^{1,2,3}$ ,  $\omega_\psi = 10$ ,  $\omega_\phi = 1$ ,  $f_s = 80$ ,  $t = 2000$

The  $3^{rd}$  term, seen in Eq. 3.198 can be rewritten as having a single cosine of  $\psi(t)$ .

$$r_m^3(t) = -C_z x_m s_\theta c_\psi + C_z y_m s_\theta s_\psi \quad (3.198)$$

$$= \kappa_{\phi_5} \cos(\psi(t)) + \kappa_{\phi_6} \sin(\psi(t)) \quad (3.199)$$

$$= \sqrt{\kappa_{\phi_5}^2 + \kappa_{\phi_6}^2} \cos\left(\phi(t) - \tan^{-1}\left(\frac{\kappa_{\phi_6}}{\kappa_{\phi_5}}\right)\right) \quad (3.200)$$

$$= \kappa_{\phi_{56}} \cos(\phi(t) + \varphi_{56}) \quad (3.201)$$

The amplitude and phase associated with the scalars of term 4 may be seen in Eq. 3.202

through Eq. 3.209.

$$\kappa_{\phi_5} = -C_z x_m s_\theta \quad (3.202)$$

$$\kappa_{\phi_6} = C_z y_m s_\theta \quad (3.203)$$

$$\kappa_{\phi_{56}} = \sqrt{\kappa_{\phi_5}^2 + \kappa_{\phi_6}^2} \quad (3.204)$$

$$= \sqrt{(C_z x_m s_\theta)^2 + (C_z y_m s_\theta)^2} \quad (3.205)$$

$$= \sqrt{C_z^2 s_\theta^2 (x_m^2 + y_m^2)} \quad (3.206)$$

$$\varphi_{\phi_{56}} = -\tan^{-1} \left( \frac{\kappa_{\phi_6}}{\kappa_{\phi_5}} \right) \quad (3.207)$$

$$= -\tan^{-1} \left( \frac{C_z y_m s_\theta}{-C_z x_m s_\theta} \right) \quad (3.208)$$

$$= -\tan^{-1} \left( \frac{y_m}{-x_m} \right) \quad (3.209)$$

The additional frequencies can be seen by expanding Eq. 3.210 to include  $\psi(t)$ .

$$r_m^3(t) = \kappa_{\phi_{56}} \cos(\phi(t) + \varphi_{56}) \quad (3.210)$$

$$= \kappa_{\phi_{56}} \cos(\omega_\psi t + f_{\psi_{FM}}(t) + \varphi_{56}) \quad (3.211)$$

$$\begin{aligned} f_{\psi_{FM}}(t) &= \beta_{\psi_0} \sin(2\omega_\psi t) + \beta_{\psi_1} \sin(4\omega_\psi t) + \beta_{\psi_1} \sin(4\omega_\psi t) \beta_{\phi_1} \sin(4\omega_\psi t) \\ &\quad + \beta_{\psi_2} \sin(6\omega_\psi t) \end{aligned} \quad (3.212)$$

The Fourier Transform of Eq. 3.211 may be seen in Eq. 3.213.

$$\mathcal{F}\{r_m^4(t)\} = \kappa_{\phi_{56}} \pi \sum_{n_0=-\infty}^{\infty} \sum_{n_1=-\infty}^{\infty} \sum_{n_2=-\infty}^{\infty} \alpha_\psi(n_0, n_1, n_2) \delta_\psi(n_0, n_1, n_2) \quad (3.213)$$

$$\alpha_\psi(n_0, n_1, n_2) = J_{n_0}(\beta_{\psi_0}) J_{n_1}(\beta_{\psi_0}) J_{n_2}(\beta_{\psi_2}) \quad (3.214)$$

$$\begin{aligned} \delta_\psi(n_0, n_1, n_2) &= e^{-j\varphi_{56}} \delta(\omega + \omega_\psi + 2n_0\omega_\psi + 4n_1\omega_\psi + 6n_2\omega_\psi) \\ &\quad + e^{j\varphi_{56}} \delta(\omega - (\omega_\psi + 2n_0\omega_\psi + 4n_1\omega_\psi + 6n_2\omega_\psi)) \end{aligned} \quad (3.215)$$

The harmonics contributed by the spin FM component in term 3 may be seen in Fig. 3.25.

The analysis of the spin periodic components contribution to terms one and two is identical to the analysis of the precession periodic contribution from Eq. 3.170 to Eq. 3.193.

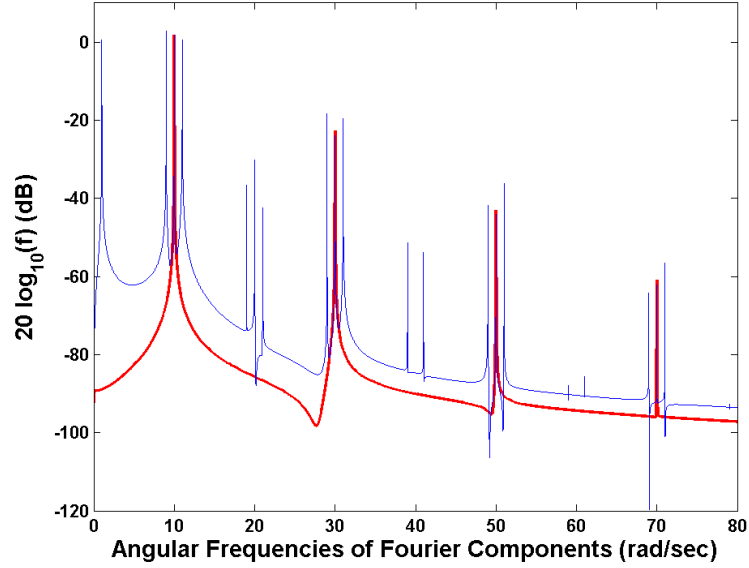


Figure 3.25: Angular Frequency Spectrum: Spin periodic component,  $r_m^3$ ,  $\omega_\psi = 10$ ,  $\omega_\phi = 1$ ,  $f_s = 80$ ,  $t = 2000$ , Additional frequencies:  $\omega_\psi(n_0 = 0, n_1 = 0)$ ,  $\omega_\psi + 2\omega_\psi(n_0 = 1, n_1 = 0)$ ,  $\omega_\psi + 4\omega_\psi(n_0 = 2, n_1 = 0; n_0 = 0, n_1 = 1)$ , etc.

Expanding Eq. 3.193 to contain the spin and precession terms produces Eq. 3.216.

$$\begin{aligned}
 r_m^{1,2}(t) = & \kappa_{p0} \cos(\omega_\phi t) \cos(\omega_\psi t + f_{\psi FM}(t)) \\
 & + \kappa_{p1} \cos(\omega_\phi t) \sin(\omega_\psi t + f_{\psi FM}(t)) \\
 & + \kappa_{p2} \sin(\omega_\phi t) \cos(\omega_\psi t + f_{\psi FM}(t)) \\
 & + \kappa_{p3} \sin(\omega_\phi t) \sin(\omega_\psi t + f_{\psi FM}(t))
 \end{aligned} \tag{3.216}$$

The frequency components of Eq. 3.216 may then be found by applying the Fourier Transform. The result may be seen in Eq. 3.217. Similarly to the precession periodic contribution, it produces an infinite number of line contributions at the odd spin rate harmonic frequencies plus and minus the precession rate harmonic frequencies. The difference between the two contributions is the amplitudes at each harmonic. The frequency contributions are summarized in Table 3.4. The harmonics contributed by the precession FM component in

Table 3.4: Spin Periodic Component Angular Frequency Spectrum Contributions

	N/A	$[1, 3, \dots]\omega_\psi$	$[1, 3 \dots]\omega_\psi \pm \omega_\phi$
1			X
2			X
3		X	
4	X		
5	X		

terms 1 and 2 may be seen in Fig. 3.26.

$$\mathcal{F}\{r_m^{12}(t)\} = \frac{\pi}{2} \sum_{n_0=-\infty}^{\infty} \sum_{n_1=-\infty}^{\infty} \sum_{n_2=-\infty}^{\infty} \alpha_{\psi 12}(n_0, n_1, n_2) \delta_{\psi 12}(n_0, n_1, n_2) \quad (3.217)$$

$$\alpha_{\psi 12}(n_0, n_1, n_2) = J_{n_0}(\beta_{\psi 0}) J_{n_1}(\beta_{\psi 1}) J_{n_2}(\beta_{\psi 2}) \quad (3.218)$$

$$\begin{aligned} \delta_{\psi 12}(n_0, n_1, n_2) = & (\kappa_{p0} + j\kappa_{p1} + j\kappa_{p2} - \kappa_{p3}) \delta(\omega + \omega_\phi + \omega_\psi + 2n_0\omega_\psi + 4n_1\omega_\psi + 6n_1\omega_\psi) \\ & (\kappa_{p0} - j\kappa_{p1} - j\kappa_{p2} - \kappa_{p3}) \delta(\omega - \omega_\phi - (\omega_\psi + 2n_0\omega_\psi + 4n_1\omega_\psi + 6n_1\omega_\psi)) \\ & (\kappa_{p0} - j\kappa_{p1} + j\kappa_{p2} + \kappa_{p3}) \delta(\omega + \omega_\phi - (\omega_\psi + 2n_0\omega_\psi + 4n_1\omega_\psi + 6n_1\omega_\psi)) \\ & (\kappa_{p0} + j\kappa_{p1} - j\kappa_{p2} + \kappa_{p3}) \delta(\omega - \omega_\phi + \omega_\psi + 2n_0\omega_\psi + 4n_1\omega_\psi + 6n_1\omega_\psi) \end{aligned} \quad (3.219)$$

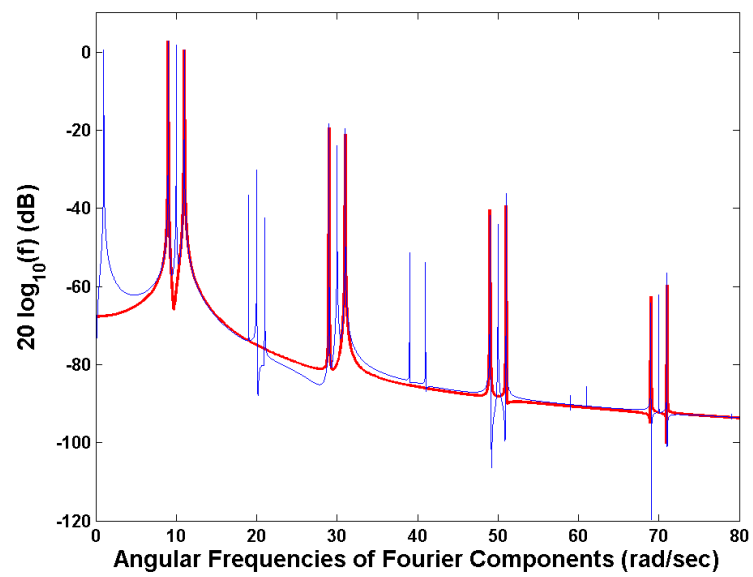


Figure 3.26: Angular Frequency Spectrum: Spin periodic component,  $r_m^{1,2}$ ,  $\omega_\psi = 10$ ,  $\omega_\phi = 1$ ,  $f_s = 80$ ,  $t = 2000$

### Nutation Periodic component

Since the nutation is defined in terms of an inverse cosine, the contribution to the frequency spectrum by the periodic component may be analyzed in two steps. The first step is to analyze the case when the nutation is evaluated by a cosine, as seen in Eq. 3.220. This function contains a cosine whose frequency is twice the spin rate and the average nutation angle  $\kappa\theta$ .

$$\cos(\theta(t)) = \frac{I_z\gamma}{h} \left( \frac{\pi}{2\mathbf{K}(k)} + \frac{(2\mathbf{K}(k) - \pi)}{2\mathbf{K}(k)} \cos\left(\frac{pt\pi}{\mathbf{K}(k)}\right) \right) \quad (3.220)$$

The second step is to analyze the case when the nutation is evaluated by a sine, as seen in Eq. 3.221. This function is more complicated as it involves a square root.

$$\sin(\theta(t)) = \sqrt{1 - \left( \frac{I_z\gamma}{h} \left( \frac{\pi}{2\mathbf{K}(k)} + \frac{(2\mathbf{K}(k) - \pi)}{2\mathbf{K}(k)} \cos\left(\frac{pt\pi}{\mathbf{K}(k)}\right) \right) \right)^2} \quad (3.221)$$

The contributions of the nutation periodic component may be seen in Fig. 3.27.

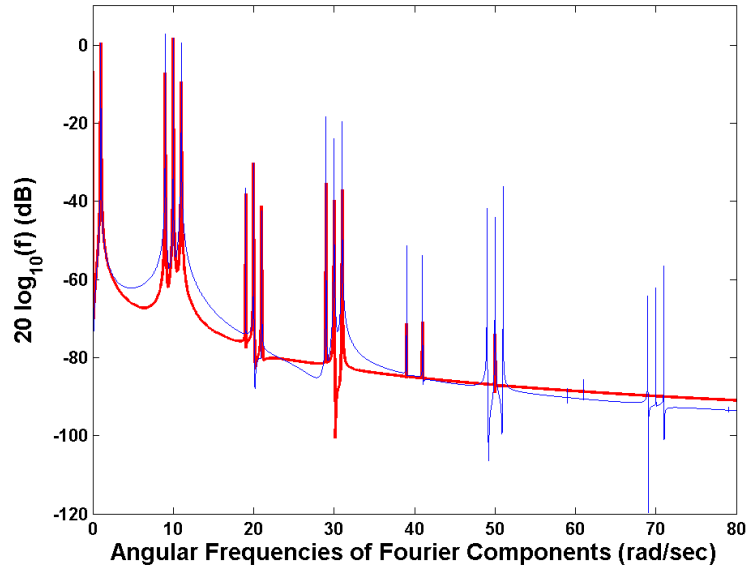


Figure 3.27: Angular Frequency Spectrum: Nutation periodic component,  $r_m^{2,3,4,5}$ ,  $\omega_\psi = 10$ ,  $\omega_\phi = 1$ ,  $f_s = 80$ ,  $t = 2000$

As seen in Eq. 3.222, the fifth term is the simplest term involving a cosine of the nutation

function.

$$r_m^5(t) = C_z z_m \cos \theta(t) \quad (3.222)$$

To make this relationship apparent, Eq. 3.222 must first be expanded to include  $\theta(t)$  as shown in Eq. 3.223 and Eq. 3.224.

$$= C_z z_m \frac{I_z \gamma}{h} \left( \frac{\pi}{2\mathbf{K}(k)} + \frac{(2\mathbf{K}(k) - \pi)}{2\mathbf{K}(k)} \cos \left( \frac{pt\pi}{\mathbf{K}(k)} \right) \right) \quad (3.223)$$

$$= C_z z_m \frac{I_z \gamma}{h} \frac{\pi}{2\mathbf{K}(k)} + C_z z_m \frac{I_z \gamma}{h} \frac{(2\mathbf{K}(k) - \pi)}{2\mathbf{K}(k)} \cos \left( \frac{pt\pi}{\mathbf{K}(k)} \right) \quad (3.224)$$

To simplify notation, the average nutation angle,  $\kappa_\theta$ , may be represented as seen in Eq. 3.225. Also, twice the spin rate may be represented as seen in Eq. 3.226.

$$\kappa_\theta = \frac{I_z \gamma}{h} \frac{\pi}{2\mathbf{K}(k)} \quad (3.225)$$

$$2\omega_\psi = \frac{pt\pi}{\mathbf{K}(k)} \quad (3.226)$$

Substituting the relationships found in Eq. 3.225 and Eq. 3.226 into Eq. 3.224 produces Eq. 3.227.

$$r_m^5(t) = C_z z_m \kappa_\theta + C_z z_m \kappa_\theta \frac{(2\mathbf{K}(k) - \pi)}{\pi} \cos(2\omega_\psi t) \quad (3.227)$$

The Fourier Transform of Eq. 3.227 may be seen in Eq. 3.228. It contains three spectral impulses located at 0,  $2\omega_\psi$ , and  $-2\omega_\psi$ . The single positive harmonic generated by the nutation periodic component in term five may be seen in Fig. 3.28.

$$\begin{aligned} \mathcal{F}\{r_m^5(t)\} &= 2C_z z_m \kappa_\theta \pi \delta(0) \\ &+ C_z z_m \kappa_\theta \frac{(2\mathbf{K}(k) - \pi)}{\pi} \pi \delta(\omega - 2\omega_\psi) \\ &+ C_z z_m \kappa_\theta \frac{(2\mathbf{K}(k) - \pi)}{\pi} \pi \delta(\omega + 2\omega_\psi) \end{aligned} \quad (3.228)$$

The other term involving a cosine of the nutation function, shown in Eq. 3.229, is term two.

$$r_m^2(t) = C_x x_m c_\theta c_\psi c_\phi + C_y x_m c_\theta c_\psi s_\phi - C_x y_m c_\theta s_\psi c_\phi - C_y y_m c_\theta s_\psi s_\phi \quad (3.229)$$



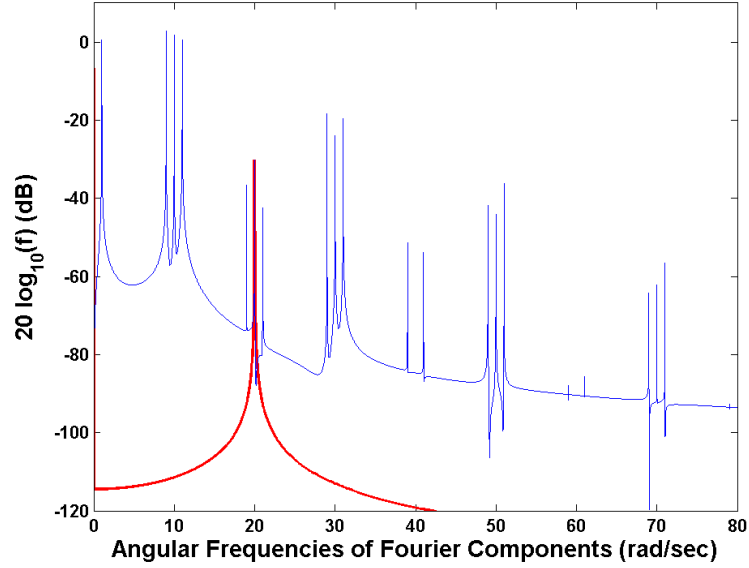


Figure 3.28: Angular Frequency Spectrum: Nutation periodic component,  $r_m^5$ ,  $\omega_\psi = 10$ ,  $\omega_\phi = 1$ ,  $f_s = 80$ ,  $t = 2000$

The relation found in Eq. 3.230 will be used to further compress the notation.

$$\kappa_{\theta k} = \kappa_\theta \frac{(2\mathbf{K}(k) - \pi)}{\pi} \quad (3.230)$$

Expanding Eq. 3.229 to include the nutation produces Eq. 3.231. Distributing the direction cosine and position scalar term into the parenthesis produces Eq. 3.232.

$$\begin{aligned} r_m^2(t) &= C_x x_m (\kappa_\theta + \kappa_{\theta k} \cos(2\omega_\psi t)) \cos(\omega_\phi t) \cos(\omega_\psi t) \\ &\quad + C_y x_m (\kappa_\theta + \kappa_{\theta k} \cos(2\omega_\psi t)) \cos(\omega_\phi t) \sin(\omega_\psi t) \\ &\quad - C_x y_m (\kappa_\theta + \kappa_{\theta k} \cos(2\omega_\psi t)) \sin(\omega_\phi t) \cos(\omega_\psi t) \\ &\quad - C_y y_m (\kappa_\theta + \kappa_{\theta k} \cos(2\omega_\psi t)) \sin(\omega_\phi t) \sin(\omega_\psi t) \end{aligned} \quad (3.231)$$

$$\begin{aligned} r_m^2(t) &= (C_x x_m \kappa_\theta + C_x x_m \kappa_{\theta k} \cos(2\omega_\psi t)) \cos(\omega_\phi t) \cos(\omega_\psi t) \\ &\quad (C_y x_m \kappa_\theta + C_y x_m \kappa_{\theta k} \cos(2\omega_\psi t)) \cos(\omega_\phi t) \sin(\omega_\psi t) \\ &\quad (-C_x y_m \kappa_\theta - C_x y_m \kappa_{\theta k} \cos(2\omega_\psi t)) \sin(\omega_\phi t) \cos(\omega_\psi t) \\ &\quad (-C_y y_m \kappa_\theta - C_y y_m \kappa_{\theta k} \cos(2\omega_\psi t)) \sin(\omega_\phi t) \sin(\omega_\psi t) \end{aligned} \quad (3.232)$$

The scalars may be collected as shown in Eq. 3.233 through Eq. 3.240.

$$\kappa_{t0} = C_x x_m \kappa_\theta \quad (3.233)$$

$$\kappa_{t1} = C_y x_m \kappa_\theta \quad (3.234)$$

$$\kappa_{t2} = -C_x y_m \kappa_\theta \quad (3.235)$$

$$\kappa_{t3} = -C_y y_m \kappa_\theta \quad (3.236)$$

$$\kappa_{t4} = C_x x_m \kappa_{\theta k} \quad (3.237)$$

$$\kappa_{t5} = C_y x_m \kappa_{\theta k} \quad (3.238)$$

$$\kappa_{t6} = -C_x y_m \kappa_{\theta k} \quad (3.239)$$

$$\kappa_{t7} = -C_y y_m \kappa_{\theta k} \quad (3.240)$$

Expanding Eq. 3.232 and replacing the scalars with the simplified terms of Eq. 3.233 through Eq. 3.240 produces Eq. 3.241.

$$\begin{aligned} r_m^2(t) = & \kappa_{t0} \cos(\omega_\phi t) \cos(\omega_\psi t) + \kappa_{t4} \cos(2\omega_\psi t) \cos(\omega_\phi t) \cos(\omega_\psi t) \\ & \kappa_{t2} \cos(\omega_\phi t) \sin(\omega_\psi t) + \kappa_{t5} \cos(2\omega_\psi t) \cos(\omega_\phi t) \sin(\omega_\psi t) \\ & \kappa_{t3} \sin(\omega_\phi t) \cos(\omega_\psi t) + \kappa_{t6} \cos(2\omega_\psi t) \sin(\omega_\phi t) \cos(\omega_\psi t) \\ & \kappa_{t4} \sin(\omega_\phi t) \sin(\omega_\psi t) + \kappa_{t7} \cos(2\omega_\psi t) \sin(\omega_\phi t) \sin(\omega_\psi t) \end{aligned} \quad (3.241)$$

The Fourier Transform of Eq. 3.241 reveals the frequencies to be found in the angular frequency spectrum. If  $\kappa_{t4}$  through  $\kappa_{t7}$  are zero, then Eq. 3.242 becomes a part of the symmetric target spectrum. The four positive frequencies may be seen in Fig. 3.29.

$$\begin{aligned} \mathcal{F}\{r_m^2(t)\} = & \frac{\pi}{4}(2\kappa_{t0} - 2\kappa_{t1} + 2j\kappa_{t2} + 2j\kappa_{t3} + \kappa_{t4} + j\kappa_{t5} + j\kappa_{t6} - \kappa_{t7}) \delta(\omega + \omega_\phi - \omega_\psi) \\ & + \frac{\pi}{4}(2\kappa_{t0} + 2j\kappa_{t1} - 2j\kappa_{t2} + 2\kappa_{t3} + \kappa_{t4} - \kappa_{t5} - j\kappa_{t6} - j\kappa_{t7}) \delta(\omega - \omega_\phi + \omega_\psi) \\ & + \frac{\pi}{4}(2\kappa_{t0} - 2j\kappa_{t2} - 2j\kappa_{t1} - 2\kappa_{t3} + \kappa_{t7} + \kappa_{t4} - j\kappa_{t6} + j\kappa_{t5}) \delta(\omega - \omega_\phi - \omega_\psi) \\ & + \frac{\pi}{4}(2\kappa_{t0} + 2j\kappa_{t1} + 2j\kappa_{t2} - 2\kappa_{t3} + \kappa_{t4} - j\kappa_{t5} + j\kappa_{t6} + \kappa_{t7}) \delta(\omega + \omega_\phi + \omega_\psi) \\ & + \frac{\pi}{4}(\kappa_{t4} + j\kappa_{t5} + j\kappa_{t6} - \kappa_{t7}) \delta(\omega + 3\omega_\psi + \omega_\phi) \\ & + \frac{\pi}{4}(\kappa_{t4} + j\kappa_{t5} - j\kappa_{t6} + \kappa_{t7}) \delta(\omega + 3\omega_\psi - \omega_\phi) \\ & + \frac{\pi}{4}(\kappa_{t4} - j\kappa_{t5} - \kappa_{t6} - j\kappa_{t7}) \delta(\omega - 3\omega_\psi - \omega_\phi) \\ & + \frac{\pi}{4}(\kappa_{t4} - j\kappa_{t5} + j\kappa_{t6} + \kappa_{t7}) \delta(\omega - 3\omega_\psi + \omega_\phi) \end{aligned} \quad (3.242)$$

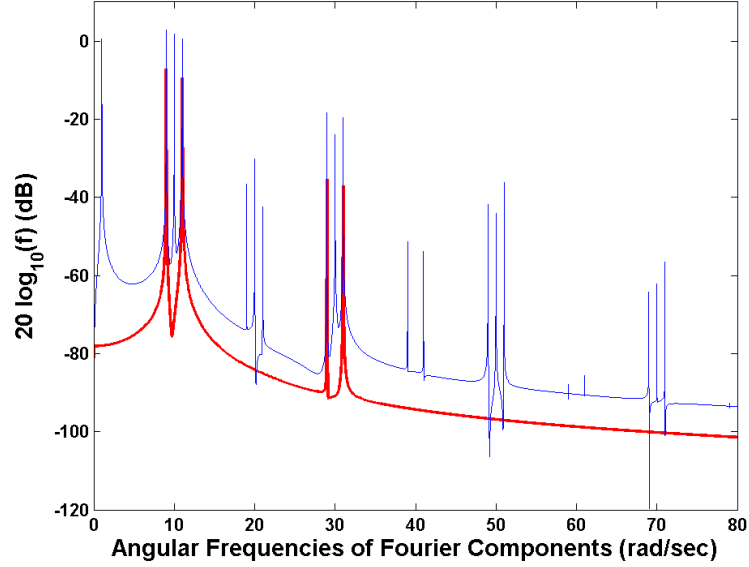


Figure 3.29: Angular Frequency Spectrum: Nutation periodic component,  $r_m^2$ ,  $\omega_\psi = 10$ ,  $\omega_\phi = 1$ ,  $f_s = 80$ ,  $t = 2000$

Terms three and four both involve evaluating the sine function with the nutation argument, as shown in Eq. 3.243.

$$\sin(\theta(t)) = \sqrt{1 - \left( \frac{I_z \gamma}{h} \left( \frac{\pi}{2\mathbf{K}(k)} + \frac{(2\mathbf{K}(k) - \pi)}{2\mathbf{K}(k)} \cos(2\omega_\psi) \right) \right)^2} \quad (3.243)$$

The computation of the Fourier Transform for Eq. 3.243 may be found in Appendix D. It is shown that the angular frequency spectrum is similar to that of an FM signal. The Fourier amplitudes,  $h_n$ , of the first seven spectral line components located at  $2n\omega_\psi$  are computed.

The third term may be seen in Eq. 3.244 through Eq. 3.246.

$$r_m^3(t) = -C_z x_m s_\theta c_\psi + C_z y_m s_\theta s_\psi \quad (3.244)$$

$$= (-C_z x_m c_\psi + C_z y_m s_\psi) s_\theta \quad (3.245)$$

$$= (\kappa_{sn2} c_\phi + \kappa_{sn3} s_\phi) s_\theta \quad (3.246)$$

The scalars of Eq. 3.246 are shown in Eq. 3.247 and Eq. 3.248.

$$\kappa_{sn2} = -C_z x_m \quad (3.247)$$

$$\kappa_{sn3} = C_z y_m \quad (3.248)$$

The frequency components of Eq. 3.246 may then be found by applying the Fourier Transform. The result may be seen in Eq. 3.249. It produces an infinite number of line contributions at the odd spin rate harmonic frequencies. The harmonics contributed by the nutation FM component in term 3 may be seen in Fig. 3.30. The frequency contributions of the nutation periodic component are summarized in Table 3.4.

$$\mathcal{F}\{r_m^3(t)\} = \frac{\pi}{2} \sum_{n_1=-\infty}^{\infty} h_{n_1} \delta_{\theta_3}(n) \quad (3.249)$$

$$\begin{aligned} \delta_{\theta_3}(n) &= (j\kappa_{sn2} - \kappa_{sn3}) \delta(\omega + \omega_\psi + 2n_1\omega_\psi) \\ &+ (-j\kappa_{sn2} + \kappa_{sn3}) \delta(\omega + \omega_\psi - 2n_1\omega_\psi) \\ &+ (-j\kappa_{sn2} - \kappa_{sn3}) \delta(\omega - \omega_\psi - 2n_1\omega_\psi) \\ &+ (j\kappa_{sn2} + \kappa_{sn3}) \delta(\omega - \omega_\psi + 2n_1\omega_\psi) \end{aligned} \quad (3.250)$$

The fourth term may be seen in Eq. 3.251 through Eq. 3.253.

$$r_m^4(t) = -C_x z_m s_\theta c_\phi + C_y z_m s_\theta s_\phi \quad (3.251)$$

$$= (-C_x z_m c_\phi + C_y z_m s_\phi) s_\theta \quad (3.252)$$

$$= (\kappa_{sn0} c_\phi + \kappa_{sn1} s_\phi) s_\theta \quad (3.253)$$

The scalars of Eq. 3.253 are shown in Eq. 3.254 and Eq. 3.255.

$$\kappa_{sn0} = -C_x z_m \quad (3.254)$$

$$\kappa_{sn1} = C_y z_m \quad (3.255)$$

The frequency components of Eq. 3.253 may then be found by applying the Fourier Transform. The result may be seen in Eq. 3.256. It produces an infinite number of line contributions at the even spin rate harmonic frequencies plus and minus the precession rate

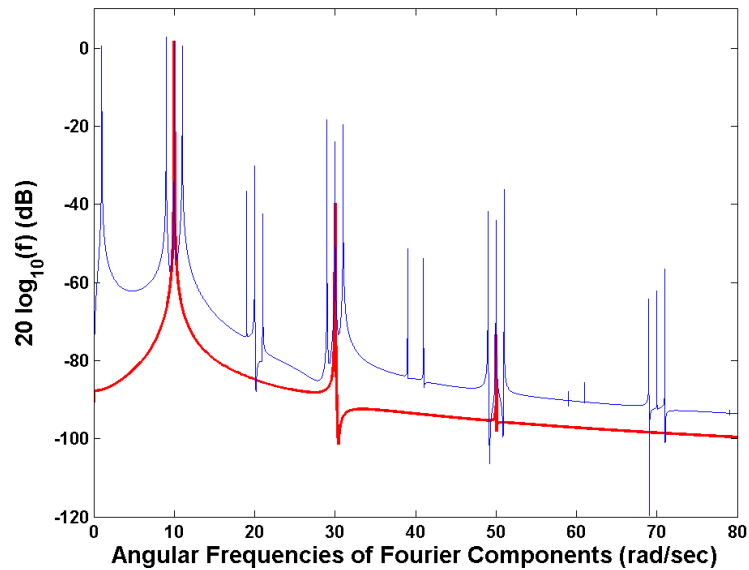


Figure 3.30: Angular Frequency Spectrum: Nutation periodic component,  $r_m^3$ ,  $\omega_\psi = 10$ ,  $\omega_\phi = 1$ ,  $f_s = 80$ ,  $t = 2000$

harmonic frequencies. The harmonics contributed by the nutation FM component in term 4 may be seen in Fig. 3.31.

$$\mathcal{F}\{r_m^4(t)\} = \frac{\pi}{2} \sum_{n_0=-\infty}^{\infty} h_{n_0} \delta_{\theta_4}(n_0) \quad (3.256)$$

$$\begin{aligned} \delta_{\theta_4}(n_0) = & (j\kappa_{sn0} - \kappa_{sn1}) \delta(\omega + \omega_\phi + 2n\omega_\psi) \\ & + (-j\kappa_{sn0} + \kappa_{sn1}) \delta(\omega + \omega_\phi - 2n\omega_\psi) \\ & + (-j\kappa_{sn0} - \kappa_{sn1}) \delta(\omega - \omega_\phi - 2n\omega_\psi) \\ & + (j\kappa_{sn0} + \kappa_{sn1}) \delta(\omega - \omega_\phi + 2n\omega_\psi) \end{aligned} \quad (3.257)$$

Table 3.6 reviews all of the frequencies found in a rigid body's angular frequency spectrum. It is broken down into the contribution of each sinusoid term from each of the rotation function's periodic component.

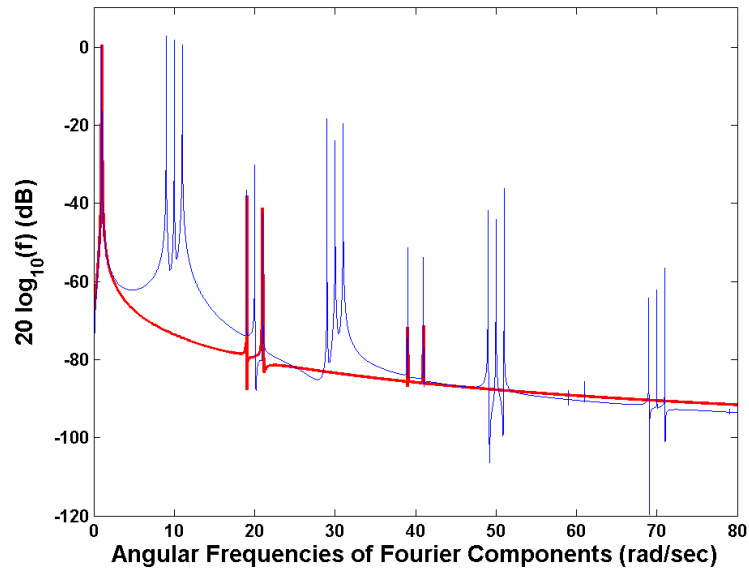


Figure 3.31: Angular Frequency Spectrum: Nutation periodic component,  $r_m^4$ ,  $\omega_\psi = 10$ ,  $\omega_\phi = 1$ ,  $f_s = 80$ ,  $t = 2000$

Table 3.5: Nutation Periodic Component Angular Frequency Spectrum Contributions

	N/A	$2\omega_\psi$	$[1, 3, \dots]\omega_\psi$	$3\omega_\psi \pm \omega_\phi$	$\omega_\psi \pm \omega_\phi$	$[0, 2, \dots]\omega_\psi \pm \omega_\phi$
1	X					
2				X	X	
3			X			
4						X
5		X				

Table 3.6: All Angular Frequency Spectrum Contributions: The first column states which periodic component contributes the frequencies for a given term. For example,  $\theta_3$  refers to the term three nutation periodic component.

	N/A	$2\omega_\psi$	$[1, 3, \dots]\omega_\psi$	$\omega_\psi \pm \omega_\phi$	$3\omega_\psi \pm \omega_\phi$	$[1, 3 \dots]\omega_\psi \pm \omega_\phi$	$[0, 2, \dots]\omega_\psi \pm \omega_\phi$
$\phi_1$				X	X	X	
$\phi_2$				X	X	X	
$\phi_3$							X
$\phi_4$	X						
$\phi_5$	X						
$\theta_1$	X						
$\theta_2$				X	X		
$\theta_3$							X
$\theta_4$			X				
$\theta_5$		X					
$\psi_1$				X	X	X	
$\psi_2$				X	X	X	
$\psi_3$	X						
$\psi_4$			X				
$\psi_5$	X						

### 3.5 Inertial Parameter Estimation

A force-free rigid body's dynamics are determined by five parameters. These five parameters, the principle moments of inertia, the angular momentum magnitude and the total kinetic energy, are thus desirable quantities to determine. If five or more equations in terms of these unknown parameters were available, an estimation problem could be formed to uniquely identify their values.

Two such equations are readily available from a Fourier analysis of the objects RTI. The spin and precession rates,  $\omega_\psi$  and  $\omega_\phi$ , are found by estimating the locations of the line components in the angular velocity spectrum. Using the linear terms from the nearly symmetric spin and precession models, each of these rates may be written in terms of the five unknown parameters.

$$\omega_\psi = \frac{p\pi}{2\mathbf{K}(k)} \quad (3.258)$$

$$= \frac{\pi}{2\mathbf{K}(k)} \sqrt{\frac{(2I_x T - h^2)(I_y - I_z)}{I_x I_y I_z}} \quad (3.259)$$

$$= \frac{\pi}{2\mathbf{K}\left(\sqrt{\frac{(I_x - I_y)(h^2 - 2I_z T)}{(I_y - I_z)(2I_x T - h^2)}}\right)} \sqrt{\frac{(2I_x T - h^2)(I_y - I_z)}{I_x I_y I_z}} \quad (3.260)$$

$$\omega_\phi = \frac{h}{I_x} - \frac{h(I_x - I_z)(\pi + \pi r(I_x, I_y, I_z, k) - 2\mathbf{K}(k))}{2I_x I_z \mathbf{K}(k)} \quad (3.261)$$

$$= \frac{h}{I_x} - \frac{h(I_x - I_z)\left(\pi + \pi r(I_x, I_y, I_z, k) - 2\mathbf{K}\left(\sqrt{\frac{(I_x - I_y)(h^2 - 2I_z T)}{(I_y - I_z)(2I_x T - h^2)}}\right)\right)}{2I_x I_z \mathbf{K}\left(\sqrt{\frac{(I_x - I_y)(h^2 - 2I_z T)}{(I_y - I_z)(2I_x T - h^2)}}\right)} \quad (3.262)$$

If more equations were known, one may be able to solve directly for  $I_x$ ,  $I_y$ ,  $I_z$ . The complex spectral magnitudes corresponding to the various line components are defined by  $5 + 2 + 3m$  unknowns for  $m$  scatterers. Five of the unknowns are the five parameters of interest, two originate from the independent direction cosine components, and  $3m$  originate from the 3D scatterer position coordinates. The magnitude of each line component may be written in terms of these  $5 + 2 + 3 = 10$  unknowns. Each scatterer generates a spectrum with 6 first order line components. Analyzing the frequency spectrum, in particular the line component magnitudes, provides  $\sim 6m$  equations in addition to the 2 equations given the known spin and precession rates.



For example, three scatterers fixed to a free body would generate spectra with  $5 + 2 + 3 * 3 = 16$  unknowns. Analysis of these spectra provides  $\sim 6 * 3 + 2 = 20$  equations. This presents an over-determined nonlinear estimation problem, as it yields 20 equations to estimate 16 unknowns. Table 3.7 shows the number of unknowns and equations provided when there exist up to 5 scatterers. While complicated, estimation of all unknowns may be

Table 3.7: Estimation of Inertial Parameters: Nonlinear Estimation Unknowns & Equations

#	# Unknowns	# Equations
1	10	8
2	13	14
3	16	20
4	19	26
5	22	32

possible given more than one scatterer.

### 3.5.1 Intermediate Result: Parameter Elimination

Given  $\omega_\psi$ ,  $\omega_\phi$  an expression may be formed using elimination in terms of four of the five unknown parameters. The elimination forms a four parameter implicit function,  $f(I_x, I_y, I_z, h)$  or  $f(I_x, I_y, I_z, T)$ , in terms of the three moments of inertia and either the angular momentum magnitude or the kinetic energy.

$$\omega_\psi = \frac{\pi}{2\mathbf{K}(k)} \sqrt{\frac{(2I_x T - h^2)(I_y - I_z)}{I_x I_y I_z}} \quad (3.263)$$

$$\omega_\phi = \frac{h}{I_x} - \frac{(h(I_x - I_z)(\pi + \pi r(I_x, I_y, I_z, k)) - 2\mathbf{K}(k))}{2I_x I_z \mathbf{K}(k)} \quad (3.264)$$

If one additional equation could be provided, such as for the elliptic modulus, an implicit function could be defined involving only the three moments of inertia.

$$k = \sqrt{\frac{(I_x - I_y)(h^2 - 2I_z T)}{(I_y - I_z)(2I_x T - h^2)}} \quad (3.265)$$

This represents a reduction to the dimensionality of a surface, as neither the kinetic energy nor the angular momentum are involved. A method for the estimation of the elliptic

modulus,  $k$ , may be found in Appendix E. The complete form of the implicit function of the three unknown moments of inertia may be found in Appendix F. Fig. 3.32 shows a plot of the 3D implicit function,  $f(I_x, I_y, I_z) = 0$ , derived from the RTI of a single tracked scatterer.

The parameter values used for the examples in this section are found in Table 3.8. If the

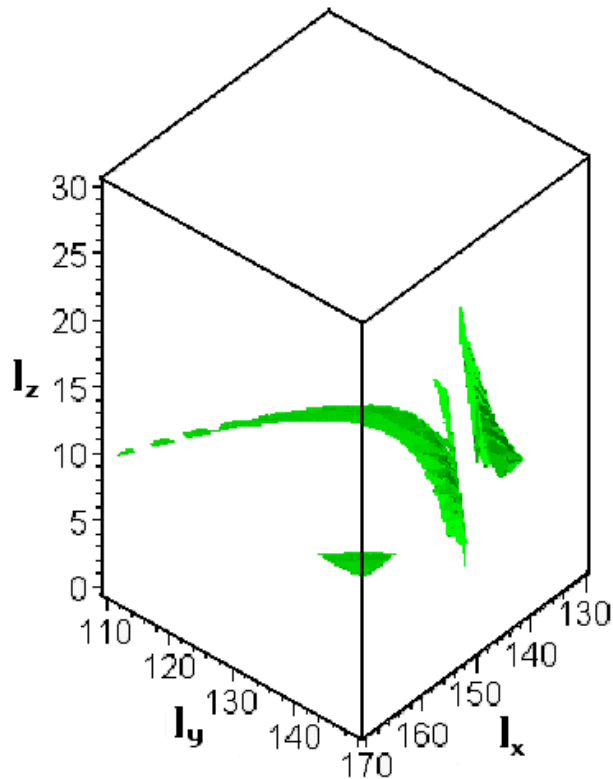


Figure 3.32: Surface of Implicit Inertial Function

Table 3.8: Example Parameters for Estimating Moments of Inertial:  $\bar{I} = [150, 130, 10]$

Surface Color	$\bar{\omega}$	$k$	$\omega_\phi$	$\omega_\psi$
Green	[0.1, 0.3, 10]	0.0209	0.71823	9.28191
Red	[0.1, 0.3, 5]	0.0438	0.77827	9.28521
Blue	[0.1, 0.6, 10]	0.0830	0.9171	9.29681

same object is viewed while it is undergoing different motions, another implicit function may be formed using data collected from each associated RTI. The intersection of the surfaces defined by the several implicit functions provide the inertial parameter values. This is similar to an idea presented in [34], where parameter ambiguity is reduced by perturbing the motion of an object by collisions with targeted projectiles to induce multiple observations. Only three different observations would be needed to uniquely determine the moments of inertia. Fig. 3.33 shows a plot of the 3D implicit functions for three observations. Note that the intersection occurs at correct parameter values of  $I_x = 150, I_y = 130, I_z = 10$  for the example found in Table 3.8.

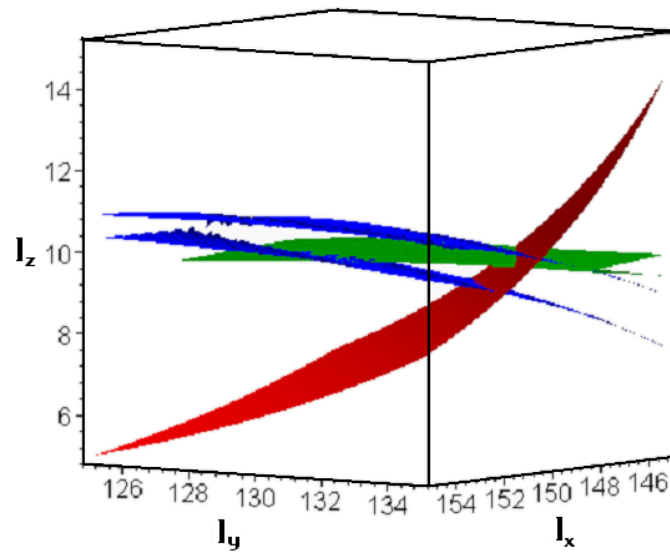


Figure 3.33: Intersecting Surfaces of Implicit Inertial Function: Each surface represents data collected for multiple initial angular velocities given the same body.

## Chapter 4

# Conclusions

This thesis introduced a physics based analysis of the Radar signature with respect to a target's physically allowed free-body rotational motion parameters. In Chapter 2, the motion of a free-body was developed. To form an analytic closed form range function for scatterers fixed to this body, the motion was defined as a series of rotations including spin, nutation, and precession. The spin and nutation time functions were readily available in literature, but the precession was only found expressed as a time derivative. The precession time derivative was thus integrated to form the elliptic integral form of the precession time function.

In Chapter 3, a motion model was developed for the case of a nearly symmetric target. This formulation is expressed in terms of inertial deviation from axial symmetry. It was shown that the angular frequency spectrum of a nearly symmetric target can be expressed as an amplitude and frequency modulated signal, while an axially symmetric target is expressed as simply an amplitude modulated signal. The contribution of each periodic rotation parameter function to the angular frequency spectrum was derived by applying an analytic Fourier decomposition. The complex amplitudes of the Fourier line spectra are then shown to contain information regarding the target inertial parameters, the scatterer positions and the Radar's line of sight.

A range-matrix factorization technique is presented in Appendix C.1. This technique extracts useful information about the target scene given only the ranges of tracked scatter-

ers. In particular, it can determine how many different free bodies are represented by the collection of scatterers and to which body each scatterer belongs.

A means of estimating target inertial parameters using measurements from the angular frequency spectrum and the nearly symmetric model was presented in Section 3.5. An intermediate result shows how observing the same target under different motion conditions may allow the unique determination of the moments of inertia of the rigid body. The importance of this result is an added capability to characterize and identify a target given the range function of a single scatterer for each observation. The result of this work finds immediate application in analyzing aligned range functions of spinning and precessing rigid bodies.

## 4.1 Future Work

The complex amplitudes of the various line components in the spectrum of a range function provide additional equations towards estimating the moments of inertia given the observation of a target undergoing rigid body motion. The formulation of this estimation problem and its application towards field data would be an important step towards target identification. Extending this analysis to the case of unaligned range functions should be considered. Performing correlations in the range dimension for each return could possibly mitigate the range alignment problem by removing all range offsets. Certain Fourier components derived from this correlated range function reference the same motion contributions. It would be pertinent to form an analytic Fourier decomposition of a correlated range function. This would provide the needed equations to estimate the inertial parameters from unaligned ranges. Other techniques to relieve corruption of range estimates should also be explored.

One ultimately desires to take Radar collections from all available sensors and use that data to provide as much discriminatory information as required to identify the target. The addition of multiple sensors could also improve the estimation of the various free body parameters. The position and inertial parameter estimation problem may be reformulated to incorporate data collected by multiple sensors and their possibly diverse viewing angles coverage. In general the multi-sensor data fusion concept has seen a fair amount of exposure[20, 32, 36, 28, 54], but few have explored the possibility of multiple Radar, physics constrained, scatterer position and inertial estimation.

## Appendix A

# Scatterer Frequency Dependence

Some scatterers are best represented using a more descriptive model than one which simply represents the RCS as being constant for all frequencies. For specific interrogation frequencies, their RCS magnitude exhibits frequency dependence according to the Geometric Theory of Diffraction (GTD)[27]. Some common GTD values are exhibited in Table A.1. Furthermore, finding scattering frequency dependencies may also be useful as typing characteristics for a tracking algorithm. The effect of GTD on the collected complex coefficient,  $\gamma(f)$ , in the scatterer model is shown in Eq. A.1.

$$\gamma(f) = \sum_k A_k f^{\alpha_k} e^{-j\frac{4\pi f}{c} r_m} \quad (\text{A.1})$$

The model may be extended to a generalized polynomial of frequency as seen in Eq. A.2.

$$\gamma(f) = \sum_k \sum_m c_{km} f^m e^{-j\frac{4\pi f}{c} r_m} \quad (\text{A.2})$$

The polynomial form may be more appropriate in some instances where ultra-wideband bandwidths are available, as the GTD model estimate will fit a single  $\alpha$  to the dependence, which may be an over simplification.

One direct method for determining the parameters of either frequency dependent model is called Parametric Scattering Law Identification (PSLI) [22]. This algorithm provides characterization of both the complex amplitude envelope and the ranges for each scatterer. Some nonlinear methods for finding the same parameters were investigated in [39][11]. An

Table A.1: GTD-predicted  $\alpha$  for Various Features.

Scattering Geometries	Power Law
Discontinuity of curvature on edge	$-4/2$
Cone tip	$-2/2$
Curved-edge diffraction	$-1/2$
Doubly curved surface, straight edge	$0/2$
Singly curved surface (cylinder)	$1/2$
Corner reflector, plate	$2/2$
Groove, duct	$3/2$
Rayleigh scattering	$4/2$

example of PSLI applied to a cone shaped target may be seen in Fig. A.1. The power-law values of  $0$ ,  $\frac{-1}{2}$ , and  $\frac{3}{2}$  were correctly identified for the sphere tip, base edges, and grooves, respectively.

The addition of this parameter to the model has illuminated an interesting occurrence. If the rank of the Hankel matrix is misjudged as a higher value than the truth, a pole multiplicity occurs for scatterers of  $\alpha$  other than zero. Furthermore, Wilkinson[52] observed that multiple roots of polynomials explode symmetrically with the introduction of noise. An explosion in this case means a movement in the complex plane away from a root's original position. As the noise is increased, the roots into which a multiple root explodes, radiate symmetrically outward. The cluster average turns out to be near the original location. Methods have been developed to recover root multiplicity by clustering the perturbed roots [9] [53] [26]. Unfortunately, these clustering methods are not robust. Clusters and singlet roots due to nearby scatterers cannot in general be separated. The key to avoiding this problem is to estimate the rank as closely as possible.



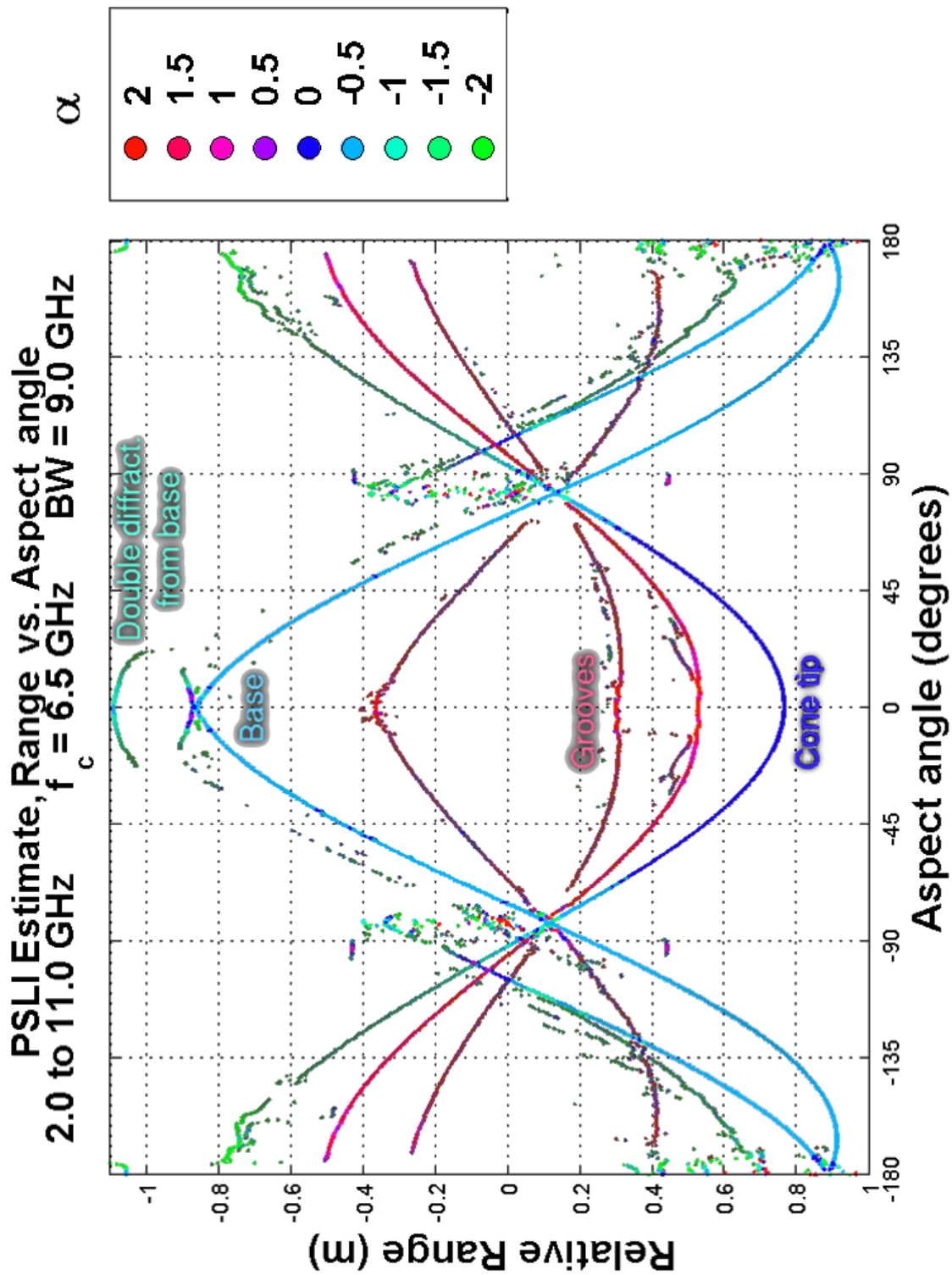


Figure A.1: RTI based upon PSLI algorithm which exploits power law representation of GTD behavior

## Appendix B

# Torque-Free Motion Examples

The rotational motion of a rigid body can produce some interesting trajectories for the affixed scatterers. Even for the same body, as defined by its moments of inertia, the trajectories can be quite different for various initial angular velocities. Table B.1 and Table B.2 list the four examples to be explored in this section. Table B.1 shows the initial conditions for each example and the elapsed time. Table B.2 shows various parameters calculated using the initial conditions

Table B.1: Motion Example - Initial Conditions:  $\bar{I}$ ,  $\bar{\omega}$ ,  $t$

#	$\bar{I} [kg \cdot m^2]$	$\bar{\omega} [\frac{rad}{s}]$	$t[s]$
1	150, 150, 30	1.0, 1.0, 0.1	75
2	150, 150, 30	1.0, 1.0, 5.0	15
3	150, 130, 30	1.0, 1.0, 5.0	15
4	150, 90, 30	1.0, 1.0, 5.0	15

The first and second targets are both axially symmetric. The difference is that the initial condition of  $\omega_z$  is varied. The first case resembles a quickly precessing, or tumbling, target. This occurs because  $\omega_z$  is set smaller than both  $\omega_x$  and  $\omega_y$ . The second case is a quickly spinning target, as the value of  $\omega_z$  is set significantly larger than  $\omega_x$  and  $\omega_y$ . Due to the symmetry, both of these cases have values of zero for  $k$  and  $n$ . The third and fourth

Table B.2: Motion Example - Parameters:  $h, T, k, n, c, \omega_\psi, \omega_\phi$ 

#	$h \left[ \frac{kg \cdot m^2}{s} \right]$	$T [J]$	$k$	$n$	$c$	$\omega_\psi \left[ \frac{rad}{s} \right]$	$\omega_\phi \left[ \frac{rad}{s} \right]$
1	212.2	150.2	0.00	0.00	1	0.08	1.41
2	259.8	525.0	0.00	0.00	1	4.00	1.73
3	248.8	515.0	0.26	-0.04	1.02	3.91	1.79
4	230.4	495.0	0.50	-0.20	1.02	3.51	2.12

examples are of spinning asymmetric targets. They have similar spin and precession rates as example three, but have nonzero  $k$  and  $n$  values. The fourth target has more asymmetry than the third target as it has a  $k$  value which has nearly doubled. The figures will be viewed by category. The five categories are rotation angles, rotation rates, 3D position and RTI.

## B.1 Rotation

In this section the rotations functions, shown in Eq. B.1 through Eq. B.3, are evaluated and plotted for the four examples. The precession  $\phi(t)$  is colored red, the nutation  $\theta(t)$  is green, and the spin  $\psi(t)$  is blue.

$$\phi(t) = \frac{h(I_x - I_z)}{pI_x I_z} \mathbf{\Pi}(sn(pt, k), n, k) - \frac{ht}{I_z} \quad (\text{B.1})$$

$$\theta(t) = \cos^{-1} \left( \frac{I_z \omega_z}{h} \right) \quad (\text{B.2})$$

$$\psi(t) = \tan^{-1} \left( \frac{-I_y \omega_y}{I_x \omega_x} \right) \quad (\text{B.3})$$

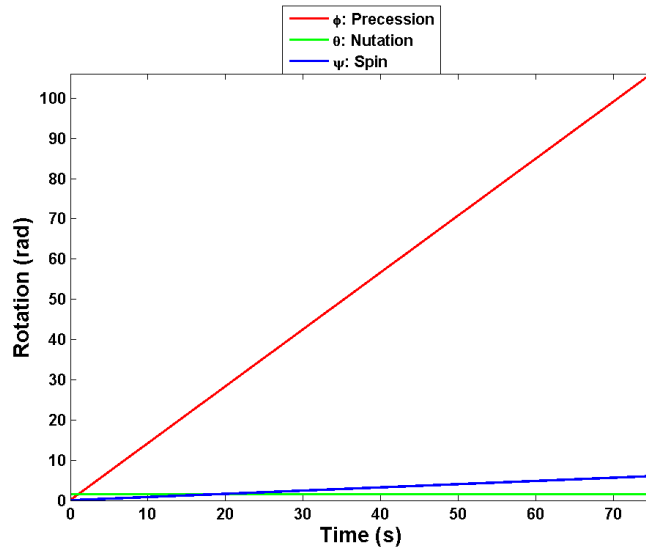


Figure B.1: Spin, nutation and precession: #1,  $\bar{I} = [150.0, 150.0, 30.0]$ ,  $\bar{\omega} = [1.0, 1.0, 0.1]$ . This plot shows a target precessing almost 20 times faster than it is spinning. This is sometimes referred to as a tumbling motion. The rotations are perfectly linear with time as the target is axially symmetric.

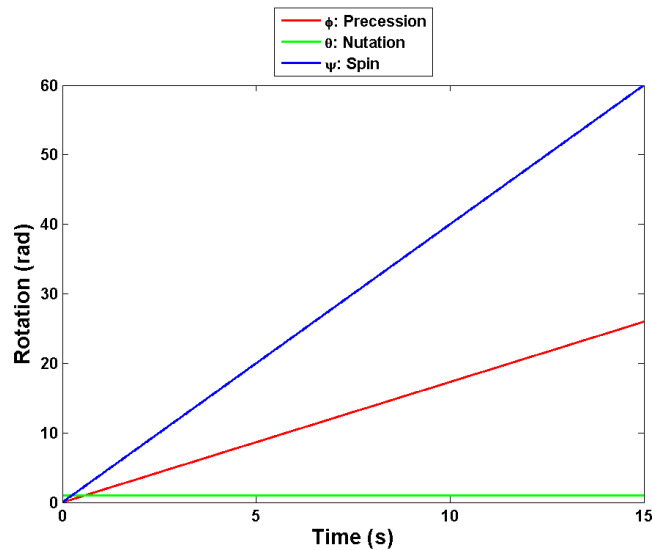


Figure B.2: Spin, nutation and precession: #2,  $\bar{I} = [150.0, 150.0, 30.0]$ ,  $\bar{\omega} = [1.0, 1.0, 5.0]$ . This plot shows a target spinning more than twice as fast as it is precessing. This is sometimes referred to as a spinning motion. The rotations are again perfectly linear with time as this target is also axially symmetric.

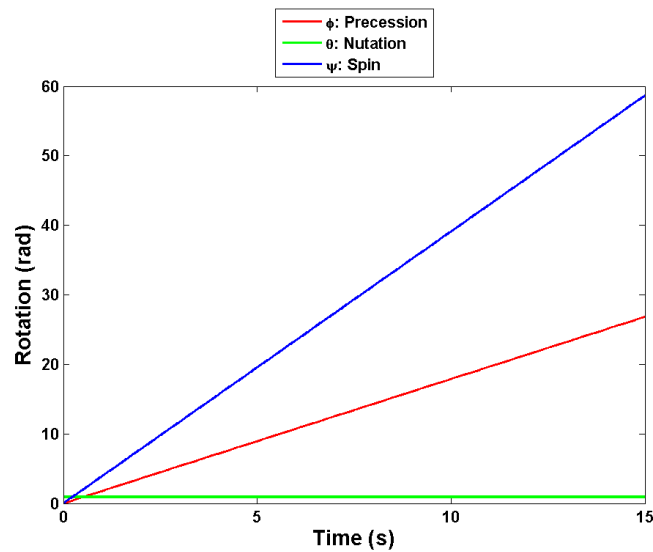


Figure B.3: Spin, nutation and precession: #3,  $\bar{I} = [150.0, 130.0, 30.0]$ ,  $\bar{\omega} = [1.0, 1.0, 5.0]$ . This plot shows a target similar to that found in example 2, although it has some axial asymmetry. It has minor sinusoidal perturbations to each rotation which are difficult to see on this plot.

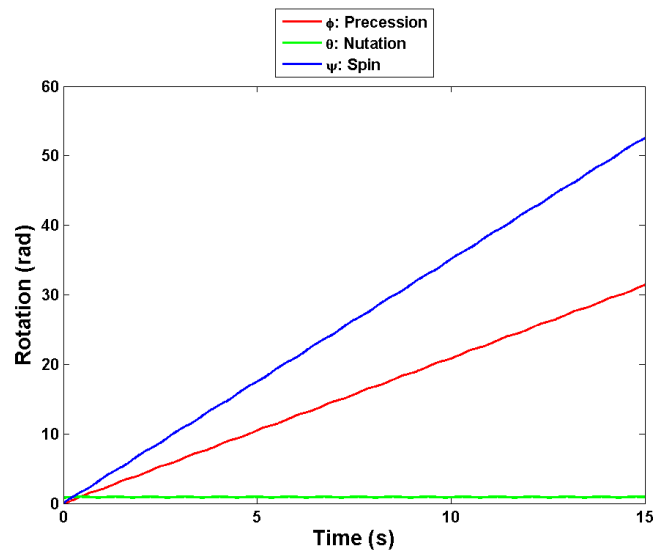


Figure B.4: Spin, nutation and precession: #4,  $\bar{I} = [150.0, 90.0, 30.0]$ ,  $\bar{\omega} = [1.0, 1.0, 5.0]$ . This plot shows a target similar to that found in examples 2 and 3, although it has more axial asymmetry. The sinusoidal perturbations are slightly more apparent on this plot.

## B.2 Rotation Rate

In this section the rotation function derivatives, shown in Eq. B.4 through Eq. B.6, are evaluated and plotted for the four examples. The precession rate  $\dot{\phi}(t)$  is colored red, the nutation rate  $\dot{\theta}(t)$  is green, and the spin rate  $\dot{\psi}(t)$  is blue.

$$\dot{\phi}(t) = \frac{h}{I_x} - \frac{h(I_x - I_z)}{pI_x I_z} \left( \frac{p}{1 - n \operatorname{sn}(pt, k)^2} - p \right) \quad (\text{B.4})$$

$$\dot{\theta}(t) = \frac{-I_z \dot{\omega}_z}{h \sqrt{1 - \frac{I_z^2 \omega_z^2}{h^2}}} \quad (\text{B.5})$$

$$\dot{\psi}(t) = \frac{-I_x I_y (\dot{\omega}_x \omega_y - \dot{\omega}_y \omega_x)}{I_x^2 \omega_x^2 + I_y^2 \omega_y^2} \quad (\text{B.6})$$

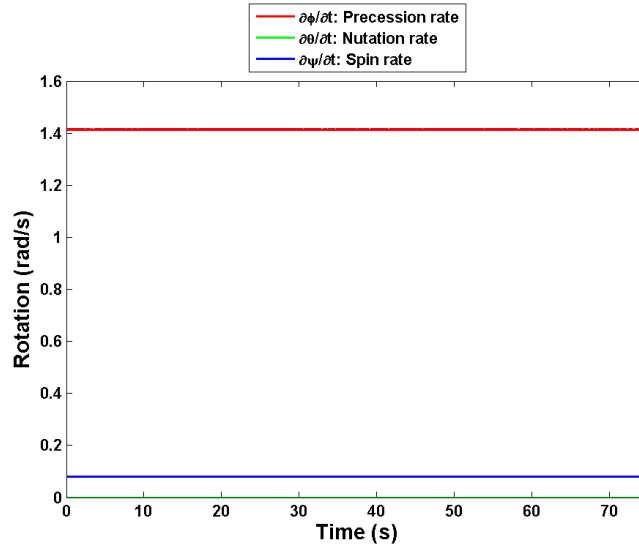


Figure B.5: Spin, nutation and precession rates: #1,  $\bar{I} = [150.0, 150.0, 30.0]$ ,  $\bar{\omega} = [1.0, 1.0, 0.1]$ . This plot shows that all three rotational rates are constant for all elapsed time. As expected from Fig. B.1 the precession rate is larger than the spin rate, and the nutation rate is zero.

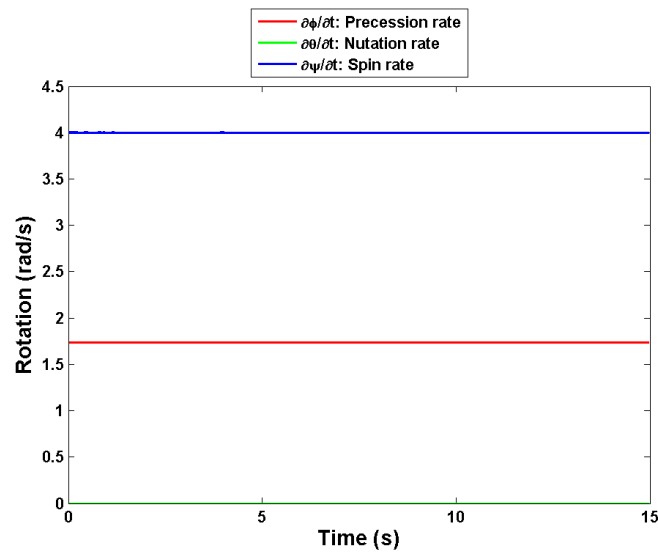


Figure B.6: Spin, nutation and precession rates: #2,  $\bar{I} = [150.0, 150.0, 30.0]$ ,  $\bar{\omega} = [1.0, 1.0, 5.0]$ . This plot shows that all three rotational rates are constant for all elapsed time. As expected from Fig. B.2 the spin rate is larger than the precession rate, and the nutation rate is again zero.

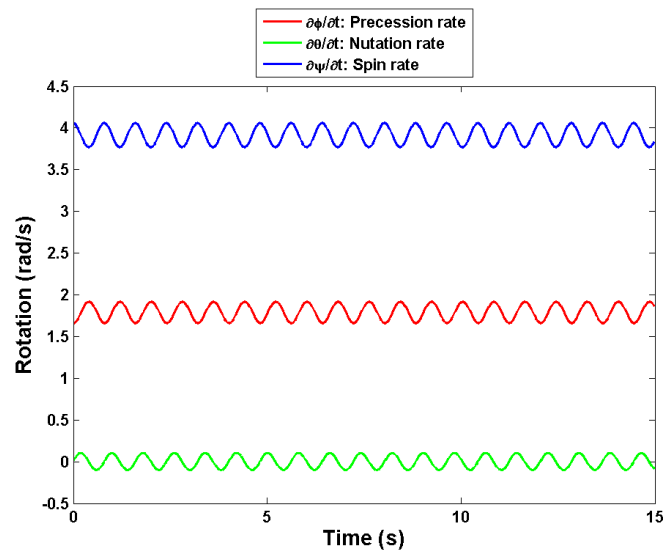


Figure B.7: Spin, nutation and precession rates: #3,  $\bar{I} = [150.0, 130.0, 30.0]$ ,  $\bar{\omega} = [1.0, 1.0, 5.0]$ . This plot shows that for the asymmetric target all three rotational rates are no longer constant. They all have a periodic perturbation of approximately  $\frac{1}{4} \frac{rad}{s}$ .

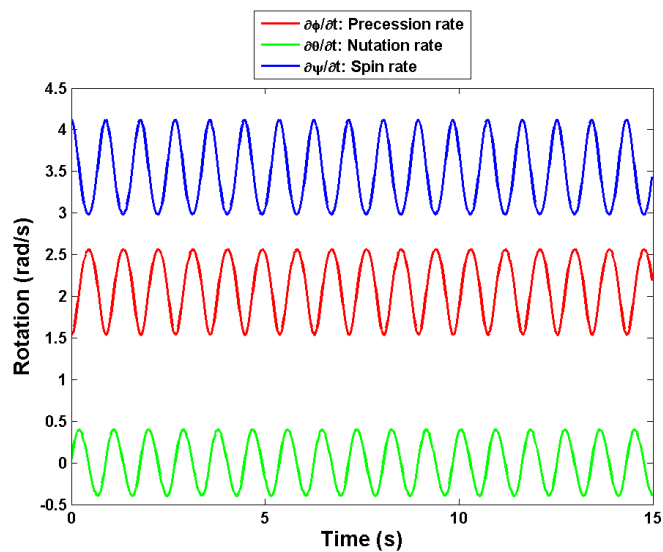


Figure B.8: Spin, nutation and precession rates: #4,  $\bar{I} = [150.0, 90.0, 30.0]$ ,  $\bar{\omega} = [1.0, 1.0, 5.0]$ . This plot shows for another asymmetric target that the three rotational rates are not constant. This target has more asymmetry than that found in the third example, and as such has a larger periodic perturbation of nearly  $1 \frac{rad}{s}$



### B.3 Scatterer Position

In this section the rotation matrices are evaluated and applied to point scatterers, as shown in Eq. B.7 and Eq. B.8, for the four examples.

$$p_m(t) = \begin{bmatrix} c_\psi c_\theta c_\phi - s_\psi s_\phi & c_\psi c_\theta s_\phi + s_\psi c_\phi & -c_\psi s_\theta \\ -s_\psi c_\theta c_\phi - c_\psi s_\phi & -s_\psi c_\theta s_\phi + c_\psi c_\phi & s_\psi s_\theta \\ s_\theta c_\phi & s_\theta s_\phi & c_\theta \end{bmatrix} \begin{bmatrix} x_m \\ y_m \\ z_m \end{bmatrix} \quad (\text{B.7})$$

$$= \begin{bmatrix} x_m(c_\psi c_\theta c_\phi - s_\psi s_\phi) + y_m(c_\psi c_\theta s_\phi + s_\psi c_\phi) - z_m c_\psi s_\theta \\ x_m(-s_\psi c_\theta c_\phi - c_\psi s_\phi) + y_m(-s_\psi c_\theta s_\phi + c_\psi c_\phi) + z_m s_\psi s_\theta \\ x_m s_\theta c_\phi + y_m s_\theta s_\phi + z_m c_\theta \end{bmatrix} \quad (\text{B.8})$$

These examples all use three point scatterers whose initial positions  $p_k$  are specified by  $\langle x, y, z \rangle$  triplets as seen in Eq. B.9 through Eq. B.11. In each example, the first scatterer is colored black, the second scatterer is red, and the third scatterer is blue.

$$p_1 = \langle 0.00, 0.00, 1.00 \rangle \quad (\text{B.9})$$

$$p_2 = \langle 0.05, 0.05, 0.50 \rangle \quad (\text{B.10})$$

$$p_3 = \langle 0.10, -0.10, -0.25 \rangle \quad (\text{B.11})$$

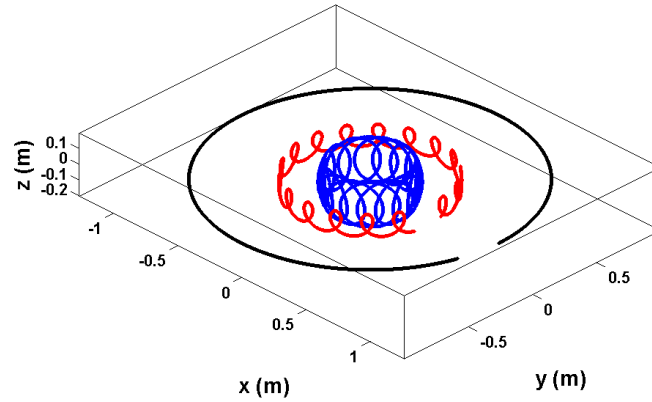


Figure B.9: 3D Scatterer Positions: Colored by scatterer: #1,  $\bar{I} = [150.0, 150.0, 30.0]$ ,  $\bar{\omega} = [1.0, 1.0, 0.1]$ . This plot shows the tumbling target. The black scatterer follows a perfectly circular trajectory due to its location on the  $z$ -axis. The circle is not close because the target does not complete a full revolution.

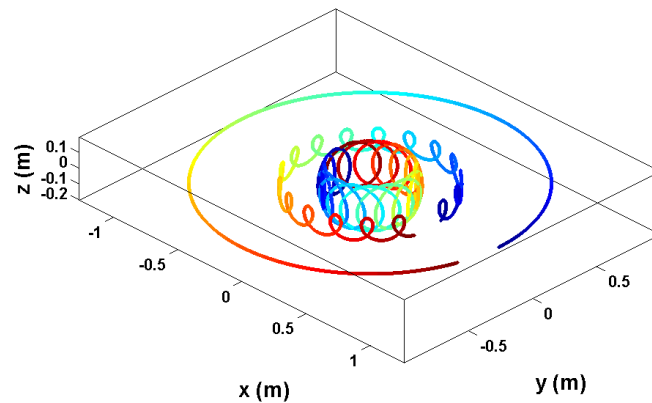


Figure B.10: 3D Scatterer Positions: Colored by time: Red indicates start of time, blue indicates end of time; #1,  $\bar{I} = [150.0, 150.0, 30.0]$ ,  $\bar{\omega} = [1.0, 1.0, 0.1]$ . This plot shows an alternate representation of example 1. The scatterer's color depicts elapsed time instead of scatterer number. Red indicates the start of the elapsed time, blue indicates the end.

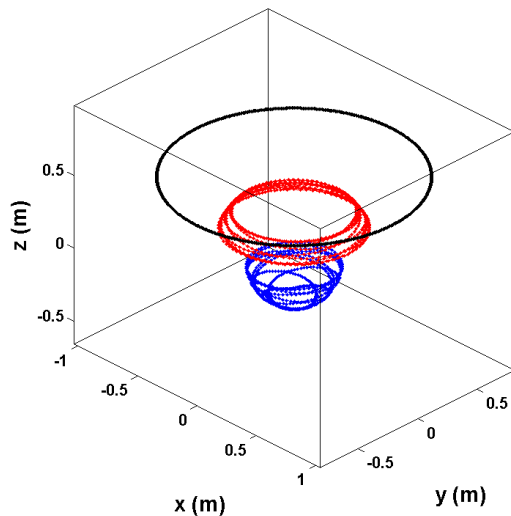


Figure B.11: 3D Scatterer Positions: Colored by scatterer: #2,  $\bar{I} = [150.0, 150.0, 30.0]$ ,  $\bar{\omega} = [1.0, 1.0, 5.0]$ . This plot shows an axially symmetric spinning target. The black scatterer again follows a circular trajectory, but is not on the same plane as the other scatterers.

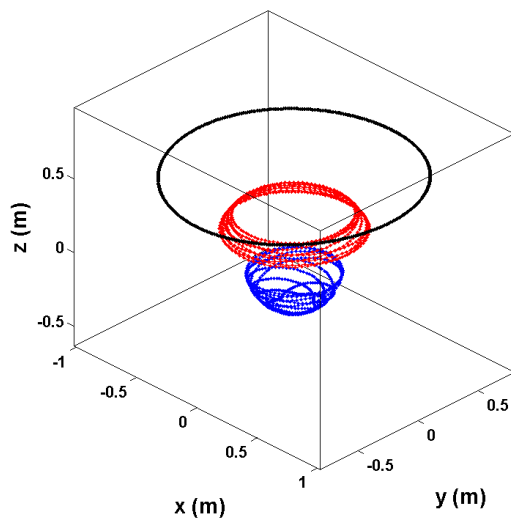


Figure B.12: 3D Scatterer Positions: Colored by scatterer: #3,  $\bar{I} = [150.0, 130.0, 30.0]$ ,  $\bar{\omega} = [1.0, 1.0, 5.0]$ . This plot shows an asymmetric spinning target. The nutation is causing the circular trajectories to become slightly bowed towards the negative  $z$ -axis.

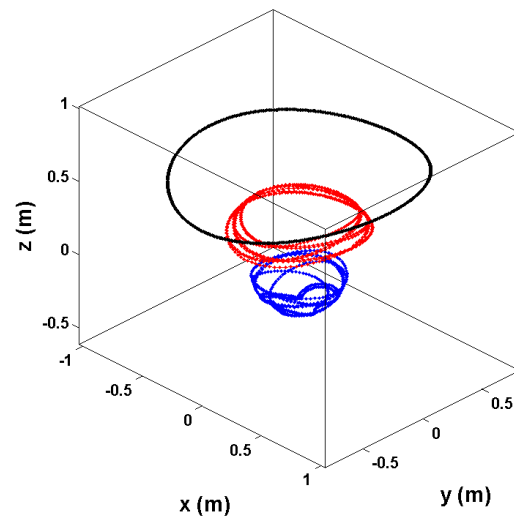


Figure B.13: 3D Scatterer Positions: Colored by scatterer: #4,  $\bar{I} = [150.0, 90.0, 30.0]$ ,  $\bar{\omega} = [1.0, 1.0, 5.0]$ . This plot shows the other asymmetric spinning target. The nutation is causing the circular trajectories to become significantly bowed towards the negative  $z$ -axis.

## B.4 Range versus Time

In this section the 1D projection, shown in Eq. B.12, is evaluated and plotted for the four examples. The projection is taken at  $C_{xyz} = [0.1098, 0.1098, 0.9879]$  for these examples. In each example, the first scatterer is colored black, the second scatterer is red, and the third scatterer is blue.

$$r_m = C_{xyz} p_m(t) \quad (\text{B.12})$$

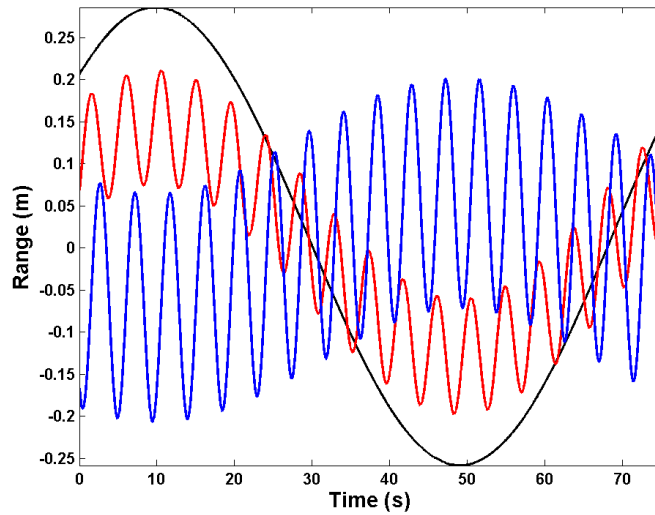


Figure B.14: Range versus Time:#1,  $\bar{I} = [150.0, 150.0, 30.0]$ ,  $\bar{\omega} = [1.0, 1.0, 0.1]$ . This plot shows the amplitude modulated range functions for each scatterer given the constant spin and precession rates of the tumbling motion. The black scatterer has periodicity given solely by the spin rate due to its location on the  $z$ -axis.

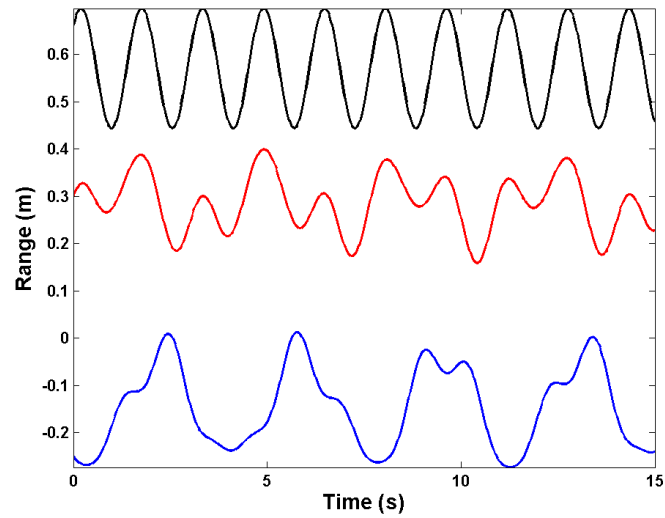


Figure B.15: Range versus Time:#2,  $\bar{I} = [150.0, 150.0, 30.0]$ ,  $\bar{\omega} = [1.0, 1.0, 5.0]$ . This plot shows the amplitude modulated range functions for each scatterer given the constant spin and precession rates of the spinning motion.

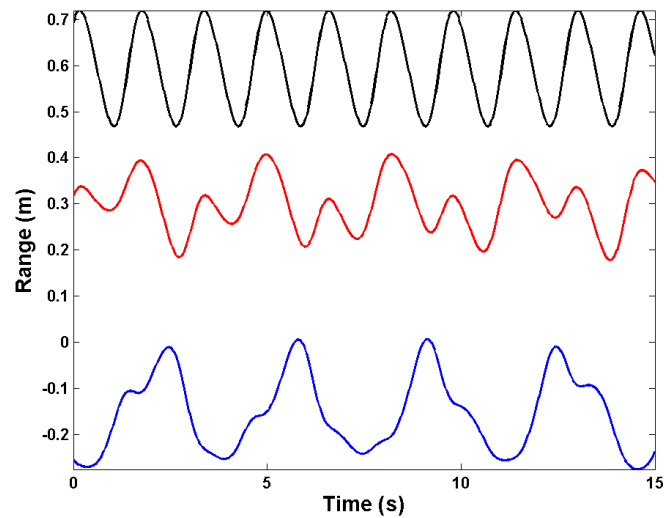


Figure B.16: Range versus Time:#3,  $\bar{I} = [150.0, 130.0, 30.0]$ ,  $\bar{\omega} = [1.0, 1.0, 5.0]$ . This plot shows the amplitude modulated and slightly frequency modulated range functions for each scatterer given the sinusoidally perturbed spin and precession rates of the spinning motion.

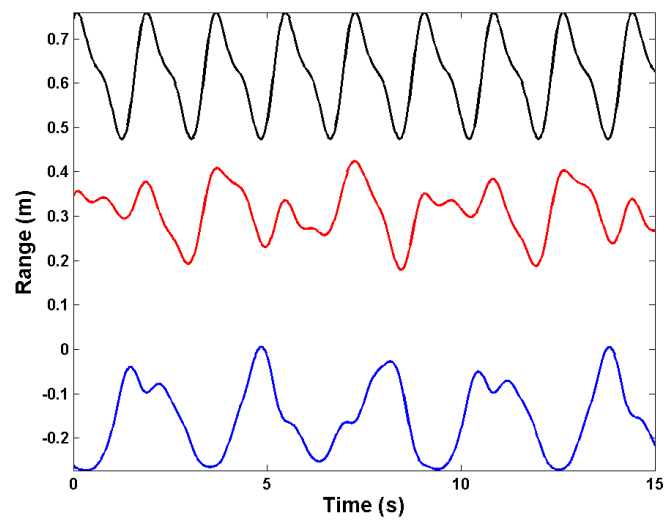


Figure B.17: Range versus Time:#4,  $\bar{I} = [150.0, 90.0, 30.0]$ ,  $\bar{\omega} = [1.0, 1.0, 5.0]$ . This plot shows the amplitude modulated and frequency modulated range functions for each scatterer given the sinusoidally perturbed spin and precession rates of the spinning motion.

## Appendix C

# Scatterer Position Estimation

There are two methods of interest for finding scatterer positions given range-only information. The first method performs a matrix factorization of a tracked scatterer matrix. It has properties well suited to separating multiple bodies. The second method applies a physics-based rotations constraint using knowledge of the rotational rates.

### C.1 Track Factorization Method

There exist methods for joint estimation of the target's motion and the positions of each scattering center. These methods may make the assumption of one or more rigid bodies existing within the target scene although they apply no motion dynamics constraints. The first algorithm to be discussed describes how to determine scatterer positions given tracked scatterers residing on a single body. The second algorithm is a novel extension to a pre-existing multiple shape factorization technique for a rotating body.

#### C.1.1 Single Body

Methods are known for the determination of a motion solution of a rigid body with limited restriction of the domain of feasible solutions. One method exploits a matrix factorization of tracked data. This has been explored in the 2D image domain[45] and has also been considered in the context of 1D interpretation[6]. It is the 1D algorithm which is particularly suited to the Radar problem. It is possible to find a 3D reconstruction of a tracked



scatterer system using a Singular Value Decomposition (SVD) of a series of scatterer ranges arranged into a rectangular matrix.

A benefit of this algorithm is that not only do we not need to know the line of sight at each return, but the returns need not be consecutive nor evenly spaced in time. This is convenient if the Radar has a variable pulse repetition frequency (PRF). However, all scatterers must be rigidly attached to the object, or undergoing identical rotational motions, else a false solution will be generated.

A scatterer track matrix  $R$  may be decomposed into two factors as seen in Eq. C.1. The first factor is an array of the scatterers affixed to the object in a target fixed coordinate system. The second is an array of direction cosines for each return signifying the rotation at each moment in time.

$$R = \begin{bmatrix} C_{x0} & C_{y0} & C_{z0} \\ C_{x1} & C_{y1} & C_{z1} \\ \vdots & \vdots & \vdots \\ C_{xn} & C_{yn} & C_{zn} \end{bmatrix} \begin{bmatrix} x_1 & x_2 & \cdots & x_m \\ y_1 & y_2 & \cdots & y_m \\ z_1 & z_2 & \cdots & z_m \end{bmatrix} \quad (\text{C.1})$$

$$= \begin{bmatrix} C_{x0}x_1 + C_{y0}y_1 + C_{z0}z_1 & \cdots & C_{x0}x_m + C_{y0}y_m + C_{z0}z_m \\ C_{x1}x_1 + C_{y1}y_1 + C_{z1}z_1 & \cdots & C_{x1}x_m + C_{y1}y_m + C_{z1}z_m \\ \vdots & \ddots & \vdots \\ C_{xn}x_1 + C_{yn}y_1 + C_{zn}z_1 & \cdots & C_{xn}x_m + C_{yn}y_m + C_{zn}z_m \end{bmatrix} \quad (\text{C.2})$$

The results of an SVD on this tracked range matrix may be used to find the motion and positions. The rank determines the complexity of the motion[45]. A rank of two would signify a 2D, or planar motion, whereas a rank of three implies a full 3D rotation space.

$$R = U\Sigma V^H \quad (\text{C.3})$$

$$= U\alpha\zeta^\top V^H \quad (\text{C.4})$$

The positions and direction cosines may then be found from Eq. C.5 and Eq. C.6.

$$\begin{bmatrix} x_1 & x_2 & \cdots & x_m \\ y_1 & y_2 & \cdots & y_m \\ z_1 & z_2 & \cdots & z_m \end{bmatrix} = -V\zeta \quad (\text{C.5})$$

$$\begin{bmatrix} C_{x0} & C_{y0} & C_{z0} \\ C_{x1} & C_{y1} & C_{z1} \\ \vdots & \vdots & \vdots \\ C_{xn} & C_{yn} & C_{zn} \end{bmatrix} = U\alpha \quad (\text{C.6})$$

The parameter  $\alpha$  is found by applying the fact that the product of a direction cosine row  $[C_x C_y C_z]$  with its transpose is one. This implies that the diagonal of a matrix product of direction cosines, each cosine vector forming a row, with its transpose is all ones. This product is shown in Eq. C.7. This may be used in the solution for  $\alpha$  by asserting that the diagonal of  $U\alpha\alpha^T U^T$  need also be ones[6, 45]. A system of equations may be composed to assert this fact. Given  $\alpha$ , the value of  $\zeta$  may be found by computing  $\Sigma\alpha^\dagger$ . Further discussion of implementation details and performance of this algorithm may be found in [45].

$$\begin{bmatrix} C_{x0} & C_{y0} & C_{z0} \\ C_{x1} & C_{y1} & C_{z1} \\ \vdots & \vdots & \vdots \\ C_{xn} & C_{yn} & C_{zn} \end{bmatrix} \begin{bmatrix} C_{x0} & C_{x1} & \cdots & C_{xn} \\ C_{y0} & C_{y1} & \cdots & C_{yn} \\ C_{z0} & C_{z1} & \cdots & C_{zn} \end{bmatrix} = \begin{bmatrix} 1 & ? & ? & ? \\ ? & 1 & ? & ? \\ ? & ? & \ddots & ? \\ ? & ? & ? & 1 \end{bmatrix} \quad (\text{C.7})$$

A 2D example RTI and resulting  $\langle x, y \rangle$  solutions of this position estimation technique may be seen in Fig. C.1 and Fig. C.2. The initial positions of the scatterers and estimated values are listed in Table C.1.

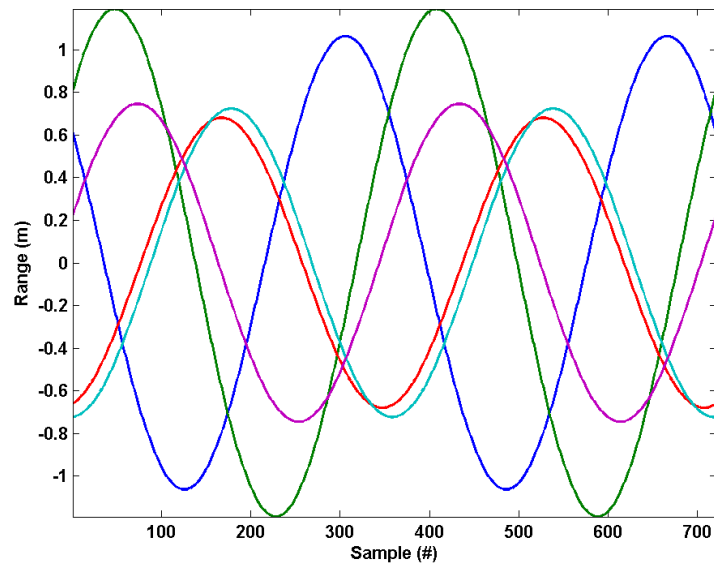


Figure C.1: RTI - 1 Body, 5 Scatterers: All scatterers follow the identical trajectory.

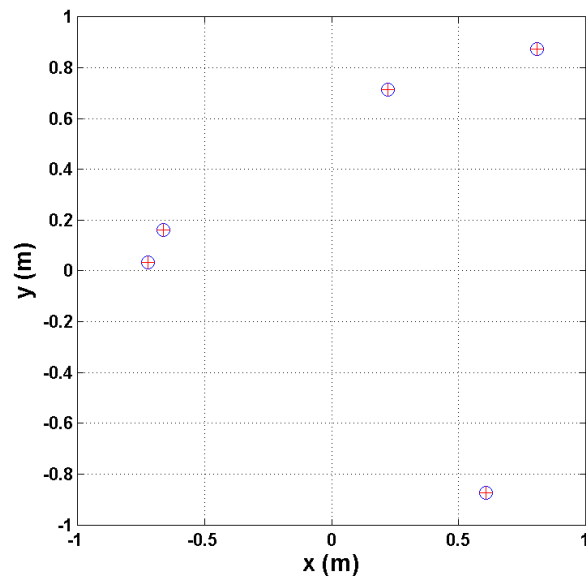


Figure C.2: Position Estimation - 1 Body, 5 Scatterers: The initial positions are depicted by the blue circles, whereas the estimated positions are shown as red + signs.

Table C.1: Position Estimation Example.  $x$  and  $y$  are truth positions,  $x'$  and  $y'$  are estimated positions.

$x$	$y$	$x'$	$y'$	$ x' - x  * 10^{-5}$	$ y' - y  * 10^{-5}$
0.6096	-0.8723	-0.6095	-0.8723	5.608	3.919
0.8110	0.8735	-0.8111	0.8734	-5.616	5.214
-0.6617	0.1605	0.6617	0.1605	-1.032	-4.254
-0.7233	0.0329	0.7233	0.0329	-0.212	-4.650
0.2211	0.7128	-0.2211	0.7128	-4.583	1.422

### C.1.2 Multiple Bodies

The target scene need not be limited to one containing a single object. When multiple objects occupy a region of space, making it difficult to determine which scattering centers belong to which object, a preprocessing step is needed in order to continue the motion estimation problem. A novel extension to the Radar multiple body problem is found by applying the concept of shape interaction matrix discussed in length by Kanade[10] to separate the tracks of their respective bodies.

This step requires the same tracked scatterer input as the previously discussed SVD factorization method, but can identify and separate the rigid bodies motions and their corresponding tracked scatterers. The algorithm is also based upon an analysis originally composed using 2D images for motion estimation of scenes containing multiple moving objects.

As previously mentioned, the rank of the tracked scatterer matrix determines the number of degrees of freedom, or the total motion dimension. When multiple bodies are present, the rank may be larger than three. For example, if the rank is five, then there possibly exists two rigid bodies, one having a 2D motion and the other a 3D motion.

The shape interaction matrix,  $Q$ , given in Eq. C.8, shows the number of objects and the dimensionality of the motion for each object.

$$Q = VV^H \quad (\text{C.8})$$

It is found by forming a product of the shape space matrix, defined in Eq. C.3,  $V$  with its hermitian. The shape space matrix is comprised of linear combinations of each rigid body sub space and can be permuted in such a way as to separate each sub-space into blocks in a block diagonal matrix  $Q$ [45]. Costeira and Kanade have shown that formation of this matrix is possible by simply sorting the columns or rows of the initial tracked scatterer matrix  $R$  such that the total off diagonal energy of Eq. C.8 is minimized. The algorithm may be summarized as follows:

1. Form  $Q$  matrix.
2. Sort the first column or row by magnitude.
3. Find all “large” values. The columns which contained these values correspond to the tracks of the  $n^{th}$  body.
4. Remove these tracks from the  $V$  matrix.
5. Repeat until all tracks are assigned to a body.

An example set of crossing tracks from three bodies may be seen in Fig. C.3. For this example, the scatterers lie in the same 2D plane. Their positions were arbitrarily chosen. The three bodies are rotating about the plane at three different rates. The position of each of the scatterers and how many rotation periods they progress in the sampled window may be found in Table C.2. The original  $Q$  matrix, graphically depicted in Fig. C.4, has no visible block structure. The process of block diagonalization determines which tracks belong to which body. The block diagonalized  $Q$  matrix for this example may be seen in Fig. C.5. The newly separated tracks, seen in Fig. C.6, may then be processed independently for motion and parameter estimation.

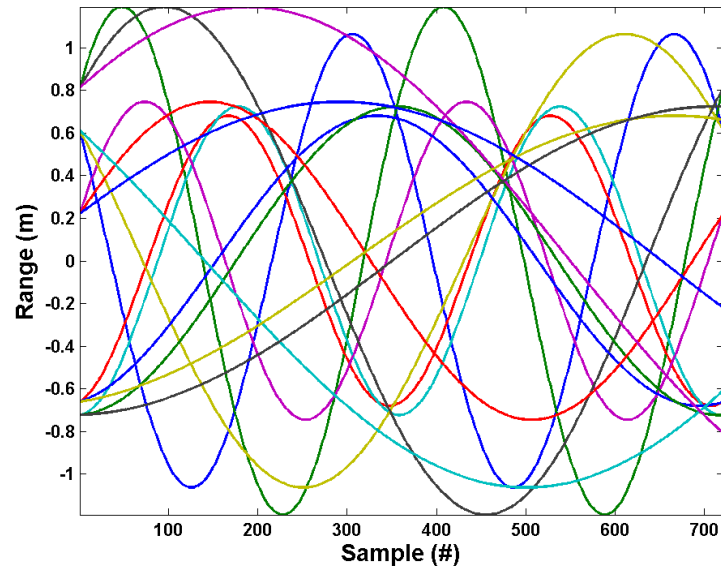


Figure C.3: RTI - 3 Bodies, 12 Scatterers: It is difficult to visually separate the overlapping tracks.

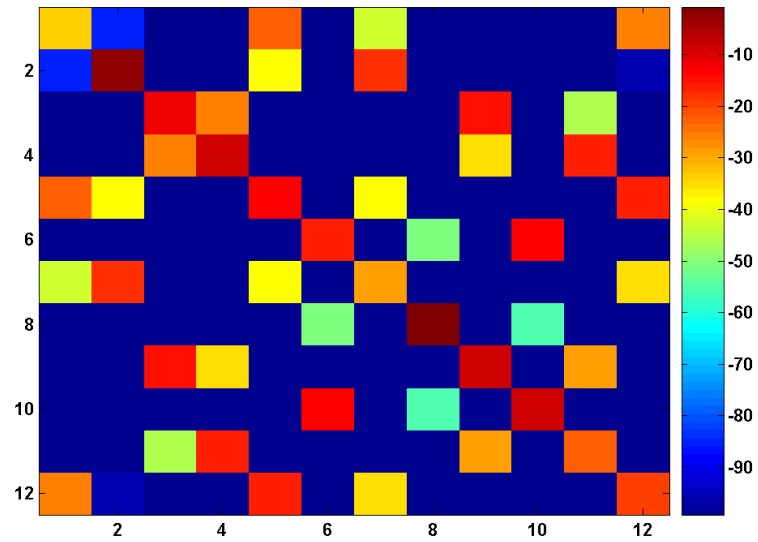


Figure C.4: Q-Matrix: There is no initial apparent structure

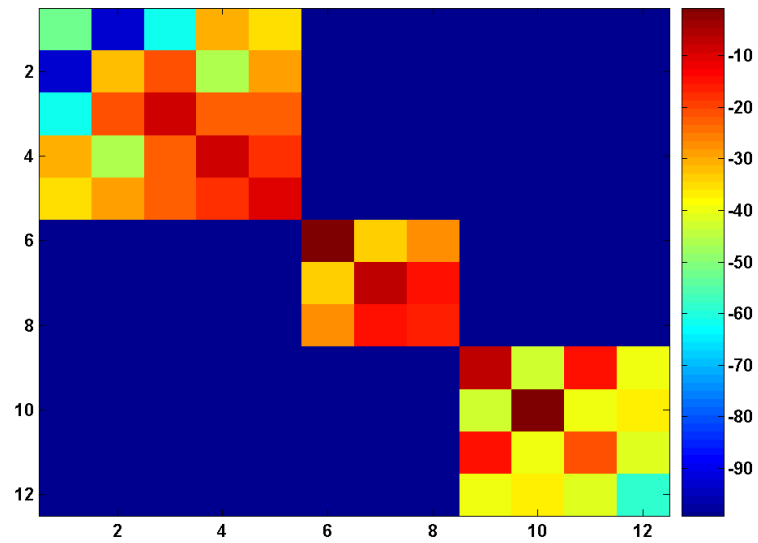


Figure C.5: Q-Matrix, Block Diagonalized: The structure shows that there are three bodies, the first has 5 scatterers, the second has 3, and the third has 4.

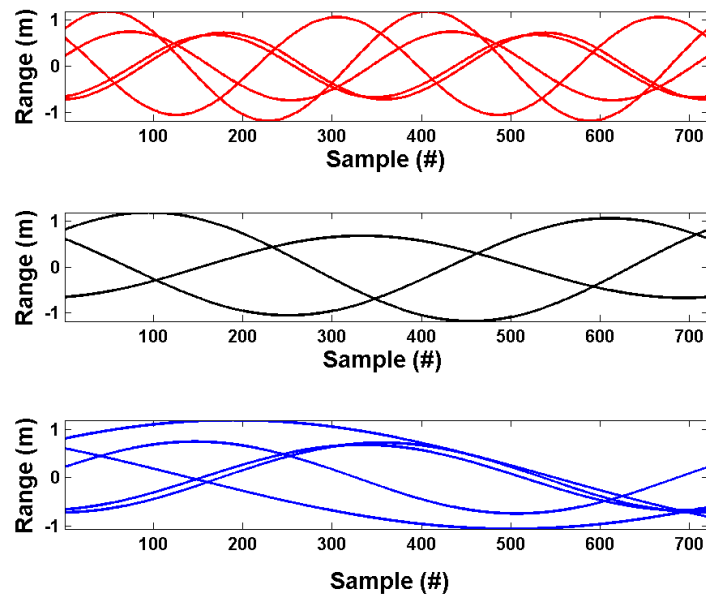


Figure C.6: RTI - Separated Bodies: The tracks from each body may now be independently processed.

Table C.2: Multi-body Identification Example.

Body #	# Rotation Periods	x	y
1	2	0.6096	-0.8723
		0.8110	0.8735
		-0.6617	0.1605
		-0.7233	0.0329
		0.2211	0.7128
2	1	-0.0690	0.2976
		0.4791	0.0813
		0.1925	-0.8936
3	0.5	-0.3322	0.1059
		-0.6568	-0.8295
		0.2498	0.1025
		-0.0871	-0.2220



## C.2 Rate Constrained

If an estimate of the rotation rates is available, such as from the frequency decomposition of a range track, the position estimate problem may be constrained to use these rates. This differs from the matrix factorization technique by requiring that the target rotates in a particular manner, not simply that it rotates. The first section briefly covers the simpler problem of a planar rotation. It shows how the estimation of the scatterers position may be posed as a least squares problem. The following section briefly covers the solution of parameters for a spinning and precessing target. This problem is posed as a nonlinear estimation problem.

### C.2.1 Planar Motion

A special case is that of a 2D planar rotation, or a tumble. This motion has a single rate of rotation, reducing the complexity of the problem to two dimensions of movement for each scatterer. Given the ranges to tracked scatterers across multiple known angles of look, one may setup a linear system of equations, seen in Eq. C.10, to solve for the position of each scatterer. The scatterers need to be tracked to extract this information. This system is solved with a single least squares fit of a sparse matrix to the range data[23]. It requires a single matrix pseudo-inverse.

$$r_m(t) = r_m \cos(\omega_\psi t + \varphi) \tag{C.9}$$

$$= x_m \cos(\omega_\psi t) + y_m \sin(\omega_\psi t) \tag{C.10}$$

The following equations represent blocks within a sparse matrix which is fit to the tracked scatterers. The constraint of each scatterer undergoing a sinusoidal motion at a fixed rate is constructed by forming a two column block for each scatterer consisting of sin

and cos evaluations of the rate times the collection time.

$$\rho = \begin{bmatrix} c_{\omega_\psi t_0} & s_{\omega_\psi t_0} \\ c_{\omega_\psi t_1} & s_{\omega_\psi t_1} \\ \vdots & \vdots \\ c_{\omega_\psi t_n} & s_{\omega_\psi t_n} \end{bmatrix} \quad (\text{C.11})$$

Each range track is formed using a corresponding coordinate, as seen in Eq. C.12.

$$\sigma_m = \begin{bmatrix} x_m \\ y_m \end{bmatrix} \quad (\text{C.12})$$

The ranges of the  $m^{\text{th}}$  tracked scatterer,  $r_m$ , are stacked in a column.

$$r_{m*} = \begin{bmatrix} r_{m(t_0)} \\ r_{m(t_1)} \\ \vdots \\ r_{m(t_n)} \end{bmatrix} \quad (\text{C.13})$$

The system of equations may be seen in Eq. C.27.

$$Ax = b \quad (\text{C.14})$$

$$\begin{bmatrix} \rho & 0 & 0 & 0 \\ 0 & \rho & 0 & 0 \\ 0 & 0 & \ddots & 0 \\ 0 & 0 & 0 & \rho \end{bmatrix} \begin{bmatrix} \sigma_1 \\ \sigma_2 \\ \vdots \\ \sigma_m \end{bmatrix} = \begin{bmatrix} r_{1*} \\ r_{2*} \\ \vdots \\ r_{m*} \end{bmatrix} \quad (\text{C.15})$$

This problem is in the form of a traditional  $Ax = b$  Least Squares problem. A pseudo-inverse is required due to the systems rectangular dimensions.

$$Ax = b \quad (\text{C.16})$$

$$x = A^\dagger b \quad (\text{C.17})$$

If the rotation rate is known and the scatterers are tracked, but there is range offset  $\xi$  occurring at each moment in time, a similar algorithm may be used to find the scatterer positions.

$$r_m(t) = x_m \cos(\omega_\psi t) + y_m \sin(\omega_\psi t) - \xi(t) \quad (\text{C.18})$$

The range offset can be represented in multiple ways. It can be arbitrary for each return, or approximated as a polynomial of some order. Arbitrary offsets add  $n$  additional unknowns, whereas polynomial offsets would only add an unknown for each degree of time. The polynomial offset is represented by a series of column vectors raising  $t$  to values up to the polynomial order.

$$t_\epsilon = \begin{bmatrix} t_1^0 & t_1^1 & \dots & t_1^o \\ t_2^0 & t_2^1 & \dots & t_2^o \\ \vdots & \vdots & \vdots & \vdots \\ t_n^0 & t_n^1 & \dots & t_n^o \end{bmatrix} \in \mathbb{R}^{(n+1) \times (o+1)} \quad (\text{C.19})$$

The arbitrary offset is represented by an identity matrix. This signifies that each time instant has its own corresponding range offset.

$$t_\epsilon = I \in \mathbb{R}^{(n+1) \times (n+1)} \quad (\text{C.20})$$

The result of the least squares fit of the new  $A$  matrix seen in Eq. C.21 to the tracked scatterer ranges produces  $x, y$  pairs and either polynomial coefficients when using Eq. C.19

or a list of range offsets using Eq. C.20.

$$A = \begin{bmatrix} \rho & 0 & 0 & 0 & t_\epsilon \\ 0 & \rho & 0 & 0 & t_\epsilon \\ 0 & 0 & \ddots & 0 & t_\epsilon \\ 0 & 0 & 0 & \rho & t_\epsilon \end{bmatrix} \quad (\text{C.21})$$

### C.2.2 Spinning and Precessing Motion

Given knowledge of the spin and precession rates, and assuming an amplitude modulation model, a nonlinear constrained estimation problem may be composed to estimate range offsets, the average nutation angle, and the fixed scatterer positions. The range offsets are with respect to the target's center of gravity, relative to the current zero range. There is one range offset for each return, creating  $n$  unknowns. The nutation angle and scatterer locations in the target's coordinate system remain constant for the collections duration adding  $1 + 3m$  more unknowns. The line of sight direction cosine adds an additional 3 unknowns.

Using the scatter coordinates, the three Euler rotations defined in Chapter 2, as well as the two Radar line of sight rotations for looking down the z-axis, one may construct an equation that would produce the RTI, as seen in Eq. C.22.

$$r_m(t) = C_{xyz} R_z(\omega_\psi t) R_y(\kappa_\theta) R_z(\omega_\phi t) p_m \quad (\text{C.22})$$

The rotations and direction cosines of Eq. C.22 may be evaluated to form Eq. C.23.

$$\begin{aligned}
r_m(\omega_\phi, \omega_\psi, t, x_m, y_m, z_m, \kappa_\theta, C_x, C_y, C_z, \xi) = & C_x x_m \cos(\kappa_\theta) [\cos(\omega_\phi \mathbf{t}) \cos(\omega_\psi \mathbf{t})] \\
& - C_y x_m \cos(\kappa_\theta) [\cos(\omega_\phi \mathbf{t}) \sin(\omega_\psi \mathbf{t})] \\
& + C_x y_m \cos(\kappa_\theta) [\sin(\omega_\phi \mathbf{t}) \cos(\omega_\psi \mathbf{t})] \\
& - C_y y_m \cos(\kappa_\theta) [\sin(\omega_\phi \mathbf{t}) \sin(\omega_\psi \mathbf{t})] \\
& - C_x z_m \sin(\kappa_\theta) [\cos(\omega_\psi \mathbf{t})] \\
& + C_y z_m \sin(\kappa_\theta) [\sin(\omega_\psi \mathbf{t})] \\
& + C_z x_m \sin(\kappa_\theta) [\cos(\omega_\phi \mathbf{t})] \\
& + C_z y_m \sin(\kappa_\theta) [\sin(\omega_\phi \mathbf{t})] \\
& - C_x x_m [\sin(\omega_\phi \mathbf{t}) \sin(\omega_\psi \mathbf{t})] \\
& - C_y z_m [\sin(\omega_\phi \mathbf{t}) \cos(\omega_\psi \mathbf{t})] \\
& + C_x y_m [\cos(\omega_\phi \mathbf{t}) \sin(\omega_\psi \mathbf{t})] \\
& + C_y y_m [\cos(\omega_\phi \mathbf{t}) \cos(\omega_\psi \mathbf{t})] \\
& + C_z z_m \cos(\kappa_\theta) - \xi \tag{C.23}
\end{aligned}$$

The equation may be organized into products of known variables with unknown variables, as seen in Table C.3. Since one knows the two rotation frequencies,  $\omega_\phi$  and  $\omega_\psi$ , as well as the scatterer range for each moment in time, we may solve for the scatterer locations in two phases. The first phase involves performing a linear least squares fit of the RTI data to the *sin* and *cos* evaluations of the the rates and corresponding times. The results of this

Table C.3: Motion Decomposition: Unknown and known terms.

Unknown	Known
$C_x x_m \cos(\kappa\theta) + C_y y_m$	$\cos(\omega_\phi \mathbf{t}) \cos(\omega_\psi \mathbf{t})$
$C_y x_m \cos(\kappa\theta) - C_x y_m$	$-\cos(\omega_\phi \mathbf{t}) \sin(\omega_\psi \mathbf{t})$
$C_x y_m \cos(\kappa\theta) - C_y x_m$	$\sin(\omega_\phi \mathbf{t}) \cos(\omega_\psi \mathbf{t})$
$C_y y_m \cos(\kappa\theta) + C_x x_m$	$-\sin(\omega_\phi \mathbf{t}) \sin(\omega_\psi \mathbf{t})$
$C_x z_m \sin(\kappa\theta)$	$-\cos(\omega_\psi \mathbf{t})$
$C_y z_m \sin(\kappa\theta)$	$\sin(\omega_\psi \mathbf{t})$
$C_z x_m \sin(\kappa\theta)$	$\cos(\omega_\phi \mathbf{t})$
$C_z y_m \sin(\kappa\theta)$	$\sin(\omega_\phi \mathbf{t})$
$C_z z_m \cos(\kappa\theta)$	1

fit is a vector,  $\sigma$ , containing the functions of unknowns.

$$\sigma_k = \begin{bmatrix} C_x x_m \cos(\kappa\theta) + C_y y_m \\ C_y x_m \cos(\kappa\theta) - C_x y_m \\ C_x y_m \cos(\kappa\theta) - C_y x_m \\ C_y y_m \cos(\kappa\theta) + C_x x_m \\ C_x z_m \sin(\kappa\theta) \\ C_y z_m \sin(\kappa\theta) \\ C_z x_m \sin(\kappa\theta) \\ C_z y_m \sin(\kappa\theta) \\ C_z z_m \cos(\kappa\theta) \end{bmatrix} \quad (\text{C.24})$$

Contained within these functions are the scatterer positions as well as the direction cosines and the average nutation angle. The second phase involves nonlinear estimation of

these remaining variables from this vector of functions.

### Least Squares

A system of equations may be generated of the form  $Ax = b$ , where  $A$  is formed from the known rotation rates and time,  $x$  is the vector unknowns for each scatterer and  $b$  is a vector of tracked scatterer ranges. To aid in the formation in the matrix  $A$ , a sub-matrix  $\rho$  is formed. This matrix, seen in Eq. C.25, contains the evaluations of the *sin* and *cos* functions for each moment in time.

$$\rho = \begin{bmatrix} c_{\omega_{\phi}t_0}c_{\omega_{\psi}t_0} & -c_{\omega_{\phi}t_0}s_{\omega_{\psi}t_0} & s_{\omega_{\phi}t_0}c_{\omega_{\psi}t_0} & -s_{\omega_{\phi}t_0}s_{\omega_{\psi}t_0} & -c_{\omega_{\psi}t_0} & s_{\omega_{\psi}t_0} & c_{\omega_{\phi}t_0} & s_{\omega_{\phi}t_0} & 1 \\ c_{\omega_{\phi}t_1}c_{\omega_{\psi}t_1} & -c_{\omega_{\phi}t_1}s_{\omega_{\psi}t_1} & s_{\omega_{\phi}t_1}c_{\omega_{\psi}t_1} & -s_{\omega_{\phi}t_1}s_{\omega_{\psi}t_1} & -c_{\omega_{\psi}t_1} & s_{\omega_{\psi}t_1} & c_{\omega_{\phi}t_1} & s_{\omega_{\phi}t_1} & 1 \\ \vdots & & \vdots & & \vdots & & \vdots & & \vdots \\ c_{\omega_{\phi}t_n}c_{\omega_{\psi}t_n} & -c_{\omega_{\phi}t_n}s_{\omega_{\psi}t_n} & s_{\omega_{\phi}t_n}c_{\omega_{\psi}t_n} & -s_{\omega_{\phi}t_n}s_{\omega_{\psi}t_n} & -c_{\omega_{\psi}t_n} & s_{\omega_{\psi}t_n} & c_{\omega_{\phi}t_n} & s_{\omega_{\phi}t_n} & 1 \end{bmatrix} \quad (\text{C.25})$$

The system of equations may be seen in Eq. C.27, where again  $x$  may found using a pseudo-inverse of  $A$ .

$$Ax = b \quad (\text{C.26})$$

$$\begin{bmatrix} \rho & 0 & 0 & 0 \\ 0 & \rho & 0 & 0 \\ 0 & 0 & \ddots & 0 \\ 0 & 0 & 0 & \rho \end{bmatrix} \begin{bmatrix} \sigma_1 \\ \sigma_2 \\ \vdots \\ \sigma_m \end{bmatrix} = \begin{bmatrix} r_1 \\ r_2 \\ \vdots \\ r_m \end{bmatrix} \quad (\text{C.27})$$

Range offsets may be handled in a similar fashion as in the 2D case for this least squares problem using Eq. C.19 and Eq. C.20.

### Nonlinear Estimation

The second step requires nonlinear minimization because of the *sin* and *cos* evaluations of the nutation angle. Nonlinear minimization also allows application of the unit magnitude constraint for the direction cosine elements. A small number of iterations using Newton's method for a nonlinear system of equations produces each of the unknowns of Eq. C.24[2]. The iterative formula for Newton's method may be seen in Eq. C.28. The variable  $x$  is a vector containing the unknowns,  $f(x)$  is the function of the unknowns, and  $J\{f(x_i)\}$  is the Jacobian of the function of unknowns.

$$x_{i+1} = x_i - J\{f(x_i)\}^\dagger * f(x_i) \quad (\text{C.28})$$

The only additional work needed for this algorithm is to determine the vector's Jacobian  $J(\sigma)$ . This Jacobian is too large to legibly illustrate in this thesis. Instead, the Jacobian of the sub-vector  $\sigma_k$  is shown in Eq. C.29. The derivative order is  $C_x, C_y, C_z, x_m, y_m, z_m, \kappa\theta$ .



$$J(\sigma_k) = \begin{bmatrix} x_m c_{\kappa_\theta} & y_m & 0 & C_x c_{\kappa_\theta} & C_y & 0 & -C_x x_m s_{\kappa_\theta} \\ -y_m & x_m c_{\kappa_\theta} & 0 & C_y c_{\kappa_\theta} & -C_x & 0 & -C_y x_m s_{\kappa_\theta} \\ y_m c_{\kappa_\theta} & -z_m & 0 & 0 & C_x c_{\kappa_\theta} & -C_y & -C_x y_m s_{\kappa_\theta} \\ x_m & y_m c_{\kappa_\theta} & 0 & C_x & C_y c_{\kappa_\theta} & 0 & -C_y y_m s_{\kappa_\theta} \\ z_m s_{\kappa_\theta} & 0 & 0 & 0 & 0 & C_x s_{\kappa_\theta} & C_x z_m c_{\kappa_\theta} \\ 0 & z_m s_{\kappa_\theta} & 0 & 0 & 0 & C_y s_{\kappa_\theta} & C_y z_m c_{\kappa_\theta} \\ 0 & 0 & x_m s_{\kappa_\theta} & C_z s_{\kappa_\theta} & 0 & 0 & C_z x_m c_{\kappa_\theta} \\ 0 & 0 & y_m s_{\kappa_\theta} & 0 & C_z s_{\kappa_\theta} & 0 & C_z y_m c_{\kappa_\theta} \\ 0 & 0 & z_m c_{\kappa_\theta} & 0 & 0 & C_z c_{\kappa_\theta} & -C_z z_m s_{\kappa_\theta} \end{bmatrix} \quad (\text{C.29})$$

An initial estimate vector must be supplied to begin the iteration sequence. The tracked scatterer factorization method is appropriate for providing initial position estimates. Since this could take an infinite number of iterations we set a tolerance factor,  $\epsilon$ , to which we compare the norm of the error.

$$\epsilon > \|x_{i+1} - x_i\|_2 \quad (\text{C.30})$$

Once this tolerance is achieved, the estimation is completed.

## Appendix D

### Frequency Decomposition: $\sin(\theta(t))$

The nutation function, as shown in Eq. D.1 has a non-trivial frequency spectrum due to its definition in terms of an inverse cosine.

$$\tilde{\theta}(t) = \cos^{-1} \left( \frac{I_z \gamma}{h} \frac{\pi}{2\mathbf{K}(k)} + \frac{I_z \gamma}{h} \frac{(2\mathbf{K}(k) - \pi)}{2\mathbf{K}(k)} \cos \left( \frac{pt\pi}{\mathbf{K}(k)} \right) \right) \quad (\text{D.1})$$

The function as an argument to sine may be written in the form shown in Eq. D.2.

$$\sin(\tilde{\theta}(t)) = \sqrt{1 - \left( \frac{I_z \gamma}{h} \frac{\pi}{2\mathbf{K}(k)} + \frac{I_z \gamma}{h} \frac{(2\mathbf{K}(k) - \pi)}{2\mathbf{K}(k)} \cos \left( \frac{pt\pi}{\mathbf{K}(k)} \right) \right)^2} \quad (\text{D.2})$$

Eq. D.2 shall be written in the compressed notation of Eq. D.3. The quantity of  $|a \pm b|$  must be less than one to keep Eq. D.3 real.

$$\sin(\tilde{\theta}(t)) = \sqrt{1 - (a + b \cos(\omega_m t))^2} \quad (\text{D.3})$$

$$a = \frac{I_z \gamma}{h} \frac{\pi}{2\mathbf{K}(k)} \quad (\text{D.4})$$

$$b = \frac{I_z \gamma}{h} \frac{(2\mathbf{K}(k) - \pi)}{2\mathbf{K}(k)} \quad (\text{D.5})$$

$$\omega_m = \frac{pt\pi}{\mathbf{K}(k)} \quad (\text{D.6})$$

As shown in Eq. D.7, the form of the transform is similar to that of a typical FM signal as it possesses an infinite number of spectral line components located at  $n\omega$ . An example spectrum is shown in Fig. D.1. The Fourier Transform, written as the integral shown in Eq. D.8, can not be directly computed. It instead is computed as a series expansion about

$b = 0$ .

$$\mathcal{F}\{\sin(\theta(t))\} = \sum_{n=-\infty}^{\infty} h_n \delta(\omega - n\omega_m) \quad (\text{D.7})$$

$$h_n = \int_0^{2\pi} e^{-jn\omega t} \sqrt{1 - (a + b \cos(\omega_m t))^2} \quad (\text{D.8})$$

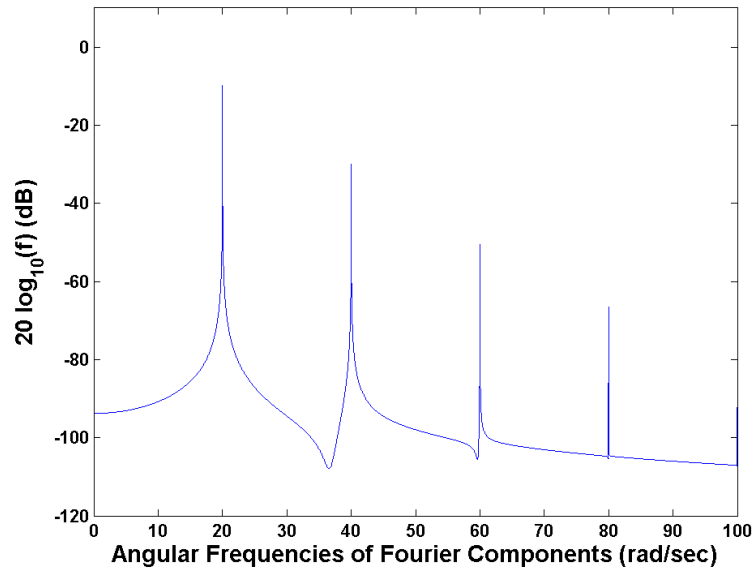


Figure D.1: Angular Frequency Spectrum:  $\sin(\theta(t))$ . Parameters:  $\omega_m = 20$ ,  $a = 0.5$ ,  $b = 0.2$ ,  $f_s = 80$ ,  $t = 2000$

To acquire the Fourier amplitudes, the integral must be computed independently for each harmonic. The amplitudes of harmonics from first to seventh order  $b$  expansion are

shown in Eq. D.9 through Eq. D.15.

$$\begin{aligned}
h_1 &= c_1((700a^2 + 175 + 280a^4)b^7 + (-160a^2 - 400a^4 + 320a^6 + 240)b^5) \\
&\quad + c_1(2304a^4 - 1536a^6 + 384 - 1536a^2 + 384a^8)b^3 \\
&\quad + c_1(1024a^{12} - 6144a^{10} + 1024 + 15360a^8)b \\
&\quad + c_1(15360a^4 - 6144a^2 - 20480a^6)b
\end{aligned} \tag{D.9}$$

$$\begin{aligned}
h_2 &= c_2((180a^2 + 120a^4 + 15)b^6 + (128a^6 + 64a^2 - 224a^4 + 32)b^4) \\
&\quad + c_2(128a^8 + 128 - 512a^6 - 512a^2 + 768a^4)b^2
\end{aligned} \tag{D.10}$$

$$\begin{aligned}
h_3 &= c_3((168a^4 + 420a^2 + 105)b^7 + (160a^6 - 80a^2 - 200a^4 + 120)b^5) \\
&\quad + c_3(128a^8 + 128 - 512a^6 - 512a^2 + 768a^4)b^3
\end{aligned} \tag{D.11}$$

$$h_4 = c_4((24a^4 + 36a^2 + 3)b^6 + (16a^6 - 28a^4 + 8a^2 + 4)b^4) \tag{D.12}$$

$$h_5 = c_5((56a^4 + 140a^2 + 35)b^7 + (32a^6 - 40a^4 - 16a^2 + 24)b^5) \tag{D.13}$$

$$h_6 = c_6(1 + 12a^2 + 8a^4)b^6 \tag{D.14}$$

$$h_7 = c_7(5 + 20a^2 + 8a^4)b^7 \tag{D.15}$$

The coefficients  $c_1$  through  $c_7$  may be seen in Eq. D.16 through Eq. D.22.

$$c_1 = \frac{-a\pi}{c(1 - 6a^2 + 15a^4 - 20a^6 + 15a^8 - 6a^{10} + a^{12})1024} \tag{D.16}$$

$$c_2 = \frac{-\pi c}{(1 - 6a^2 + 15a^4 - 20a^6 + 15a^8 - 6a^{10} + a^{12})512} \tag{D.17}$$

$$c_3 = \frac{ac\pi}{(-1 + 7a^2 - 21a^4 + 35a^6 - 35a^8 + 21a^{10} - 7a^{12} + a^{14})1024} \tag{D.18}$$

$$c_4 = \frac{-c\pi}{(1 - 6a^2 + 15a^4 - 20a^6 + 15a^8 - 6a^{10} + a^{12})256} \tag{D.19}$$

$$c_5 = \frac{ac\pi}{(-1 + 7a^2 - 21a^4 + 35a^6 - 35a^8 + 21a^{10} - 7a^{12} + a^{14})1024} \tag{D.20}$$

$$c_6 = \frac{-c\pi}{(1 - 6a^2 + 15a^4 - 20a^6 + 15a^8 - 6a^{10} + a^{12})512} \tag{D.21}$$

$$c_7 = \frac{ac\pi}{(-1 + 7a^2 - 21a^4 + 35a^6 - 35a^8 + 21a^{10} - 7a^{12} + a^{14})1024} \tag{D.22}$$

$$c = \sqrt{1 - a^2} \tag{D.23}$$

## Appendix E

# Elliptic Modulus Estimation

The elliptic modulus, (Eq. E.1), provides a measure of asymmetry for a nearly symmetric target.

$$k = \sqrt{\frac{\epsilon}{I_x - \epsilon - I_z} \frac{(h^2 - 2I_z T)}{(2I_x T - h^2)}} \quad (\text{E.1})$$

Estimation of this parameter would thereby present an analyst with an additional metric useful for the characterization of a target. This section shows how the modulus may be determined using the angular frequency spectrum along with estimates of the Radar line of sight, the scatterer position, and the average nutation angle. Each of these parameters may be estimated using a method such as the one described in Appendix C. As shown in section 3.1, the elliptic modulus is determined by the moment of inertia and the initial angular velocities. When the target is axially symmetric, the elliptic modulus is zero. In section 3.3, a nearly symmetric target was defined as having a modulus of less than 0.5.

Two important time-constant parameters describing the motion of an axially asymmetric object are its spin and precession rates, found in Eq. E.2 and Eq. E.3, which have units of angular velocity, radians per second.

$$\omega_\psi = \frac{p\pi}{2\mathbf{K}(k)} \quad (\text{E.2})$$

$$\omega_\phi = \frac{h}{I_x} - \frac{h(I_x - I_z)(\pi + \pi r - 2\mathbf{K}(k))}{2I_x I_z \mathbf{K}(k)} \quad (\text{E.3})$$

In the following, we will examine the relationship between these two rates and the asymmetry of the target as characterized by its elliptic modulus. A visual aid for this discussion

appears in Fig. E.1. The figure describes the Fourier component frequencies of the range function for a given set of targets,  $\bar{I} = [150, 150 \rightarrow 60, 10]$ , for which the initial body-fixed angular velocities are  $\bar{\omega} = [1, 1, 10]$ . This sweeping of  $I_y$  away from  $I_x$  increases the target's axial asymmetry, thereby increasing the elliptic modulus. The spin and precession rates are indicated in the graph by dots which provide the associated rate value on the angular frequency axis and the magnitude of the Fourier components of the range function on the dependent axis. The target asymmetry, and thus the elliptic modulus, is denoted by the color of the dots. For values of  $k$  ranging from 0 to 0.5, the colors transition from black to a light beige. The dots representing the first spin harmonic instead transition from blue to red, as these are the angular frequencies of immediate interest in the discussion that follows.

As shown in the modulation analysis, (section 3.4.2), the spin harmonic is generated by the nutation periodic component of the fifth rotation term. The Fourier Transform of this term may be seen again in Eq. E.4. It contains three spectral impulses located at 0,  $2\omega_\psi$ , and  $-2\omega_\psi$ .

$$\begin{aligned} \mathcal{F}\{r_m^5(t)\} &= 2C_z z_m \kappa_\theta \pi \delta(0) \\ &+ C_z z_m \kappa_\theta \frac{(2\mathbf{K}(k) - \pi)}{\pi} \pi \delta(\omega - 2\omega_\psi) \\ &+ C_z z_m \kappa_\theta \frac{(2\mathbf{K}(k) - \pi)}{\pi} \pi \delta(\omega + 2\omega_\psi) \end{aligned} \quad (\text{E.4})$$

The magnitude of the positive frequency spin harmonic may be seen in Eq. E.5. The function is simplified in Eq. E.6 and Eq. E.7.

$$v(k) = C_z z_m \kappa_\theta \frac{(2\mathbf{K}(k) - \pi)}{\pi} \pi \quad (\text{E.5})$$

$$= C_z z_m \kappa_\theta (2\mathbf{K}(k) - \pi) \quad (\text{E.6})$$

$$= 2C_z z_m \kappa_\theta \mathbf{K}(k) - \pi C_z z_m \kappa_\theta \quad (\text{E.7})$$

Solving Eq. E.7 for the Complete Elliptic Integral of the First Kind,  $\mathbf{K}(k)$ , produces Eq. E.8. Values of  $\mathbf{K}(k)$  for various  $k$  are shown in Fig. E.2.

$$\mathbf{K}(k) = \frac{v(k) + C_z z_m \kappa_\theta \pi}{2C_z z_m \kappa_\theta} \quad (\text{E.8})$$

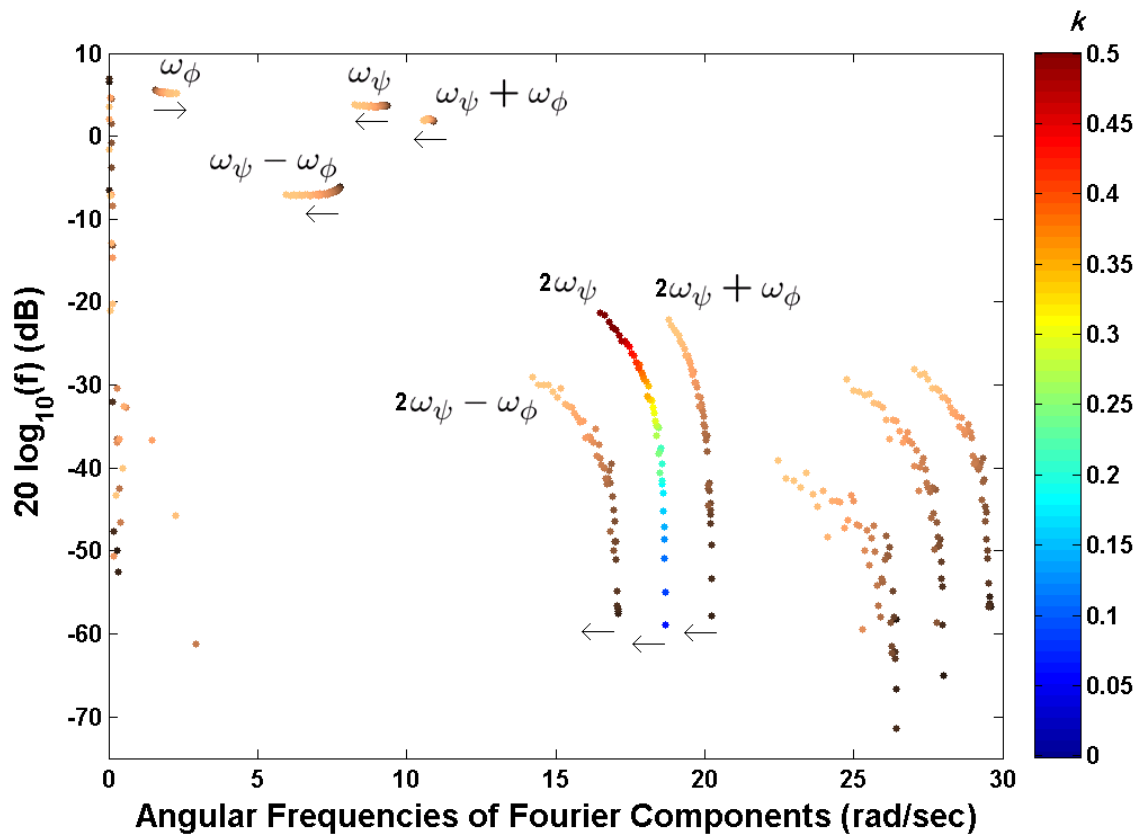


Figure E.1: Angular Frequency Spectrum for various  $k$ :  $I_x = 150$ ,  $I_y = 150 \rightarrow 60$ ,  $I_z = 10$ ,  $\bar{\omega} = [1, 1, 10]$ . The color denotes  $k$  value. The arrows indicate the direction toward which the measured rate travels as the elliptic modulus is increased.

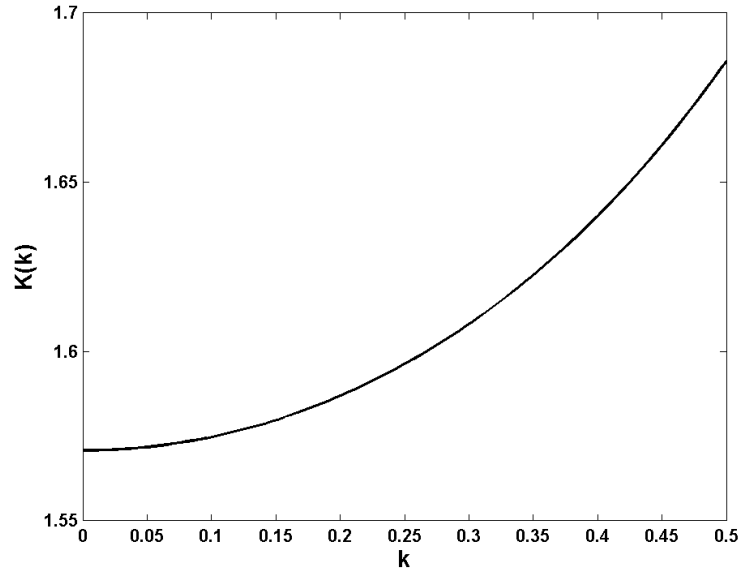


Figure E.2:  $K(k)$  versus  $k$

The value of  $k$  can be determined by evaluating the inverse of  $\mathbf{K}(k)$ . As an analytical inverse was not available, a table of values is used to compute the value of  $k$  given an estimate of  $\mathbf{K}(k)$ . This table was generated by evaluating  $k$  values ranging from 0.00 to 0.75, spaced apart by 0.0005 with the  $\mathbf{K}(k)$  function.

An example angular frequency spectrum to be used for elliptic modulus estimation may be seen in Fig. E.3. The magnitude of the spin harmonic frequency component is found from the figure to be  $-46.63dB$ , or 0.0047. Substituting this magnitude into Eq. E.8 produces a  $\mathbf{K}(k)$  value of 1.6179. Evaluating this in the inverse  $\mathbf{K}(k)$  function produces an elliptic modulus of 0.3349, whereas the truth value is 0.3390.

Results of estimating the elliptic modulus for various input parameters may be seen in Fig. E.4. This plot shows the average magnitude of the elliptic modulus estimation error for various  $C_z$  and  $z$ . For each combination of  $C_z$  and  $z$ , there were 45 trials sweeping the value of  $k$  from 0.05 to 0.5. There were 625 combinations of  $C_z$  and  $z$  tested. The values of  $C_z$  ranged from  $-1$  to  $1$  while  $z$  ranged from  $-4$  to  $4$ . The initial conditions are summarized in Table E.1.



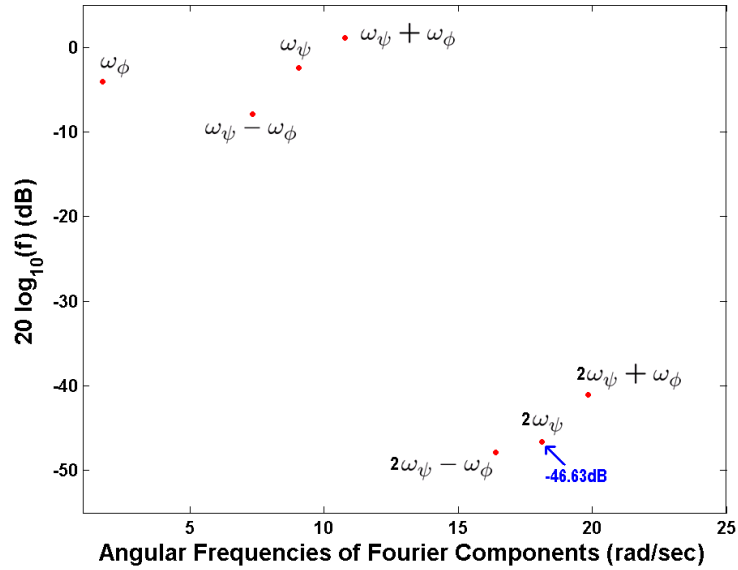


Figure E.3:  $k$  Estimation Example: Angular Frequency Spectrum.  $C_{xyz} = [0.71, 0.58, 0.43]$ ,  $p_{xyz} = [2.92, 1.62, 1.52]$ ,  $\kappa_\theta = 0.48$

Table E.1: Parameters for  $k$  Estimation Trials

Parameter	Values
$I_x$	150
$I_y$	150, 148, 146, . . . , 64, 62, 60
$I_z$	10
$\bar{\omega}$	[1, 1, 10]
$C_z$	-1.0000, -0.9625, -0.9250, . . . , 0.9250, 0.9625, 1
$z$	-4.0000, -3.6667, -3.3333, . . . , 3.3333, 3.6667, 4.000

The results shown in Fig. E.4 indicate that on average, the value of  $k$  was estimated with an error of less than 0.05 for  $C_z$  and  $z$  values larger than 0.25. As these values increase, the estimation error decreases. To estimate  $k$ , the values of  $C_z$ ,  $z_m$  and  $\kappa_\theta$  must not be near zero, else the magnitude of the first harmonic is too small to accurately measure. Fig. E.5 illustrates the region on the direction cosine unit sphere where the magnitude of the second

harmonic is negligible.

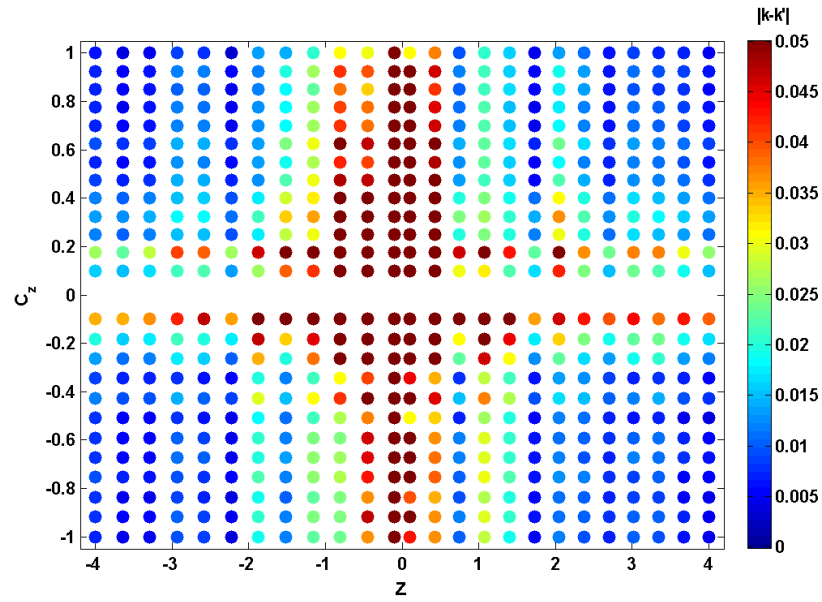


Figure E.4: Error in the estimation of  $k$ :  $|k - k_{est}|$ . For each  $C_z$  and  $z$  trial there is a dot whose color denotes the average elliptic modulus estimation error.

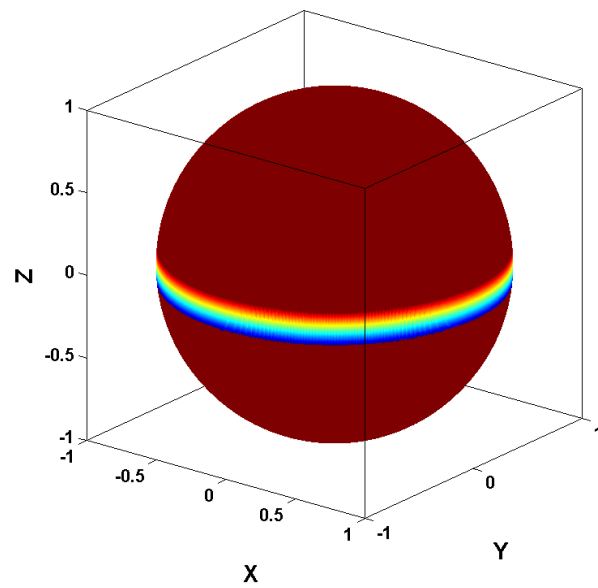


Figure E.5: Direction Cosine constraint: The rainbow colored band represents values of  $C_z$  in the target fixed coordinate system near zero. A range function that is generated using a line of sight which pierces this region would not generate a harmonic magnitude large enough to accurately measure.

## Appendix F

# Elimination: 3 Parameter Implicit Function

Elimination may be applied to reduce the number of unknown parameters in the estimation of the inertial values. In this particular case, three equations are known, so two parameters may be eliminated.

$$\omega_\psi = \frac{\pi}{2\mathbf{K}(k)} \sqrt{\frac{(2I_x T - h^2)(I_y - I_z)}{I_x I_y I_z}} \quad (\text{F.1})$$

$$\omega_\phi = \frac{h}{I_x} - \frac{(h(I_x - I_z)(\pi + \pi r(I_x, I_y, I_z, k)) - 2\mathbf{K}(k))}{2I_x I_z \mathbf{K}(k)} \quad (\text{F.2})$$

$$k = \sqrt{\frac{(I_x - I_y)(h^2 - 2I_z T)}{(I_y - I_z)(2I_x T - h^2)}} \quad (\text{F.3})$$

The result is an implicitly defined function in terms of the three principle moments of inertia.

$$f(I_x, I_y, I_z) = 0 \quad (\text{F.4})$$

$$f(I_x, I_y, I_z) = k - \sqrt{\frac{n_q(I_x, I_y, I_z)}{d_q(I_x, I_y, I_z)}} \quad (\text{F.5})$$

$$(\text{F.6})$$

The various variables used in Eq. F.4 may be seen in Eq. F.7 through Eq. F.25.

$$n_q = c_1 (\gamma_1 + \gamma_2 + \gamma_3) \quad (\text{F.7})$$

$$d_q = c_2 (\gamma_4 + \gamma_5 + \gamma_6) \quad (\text{F.8})$$

$$c_1 = I_z (I_x - I_y) \omega_\phi^2 \quad (\text{F.9})$$

$$c_2 = I_x (I_y - I_z) I_y \omega_\psi^2 \quad (\text{F.10})$$

$$\gamma_1 = -\pi I_{x2y} + \pi I_{x2y} - 4I_{x2y} \mathbf{K}(k) + 4 \frac{I_{x2y}}{\pi} \mathbf{K}(k)^2 + \pi I_{x2y} r^2 \quad (\text{F.11})$$

$$\gamma_2 = 2\pi I_{x2y} r - 4I_{x2y} r \mathbf{K}(k) + I_{yz2} r^2 + 2I_{yz2} r + I_{yz2} + I_{xz2} - I_{x2z} \quad (\text{F.12})$$

$$\gamma_3 = -2\pi I_{xyz} r^2 - 4\pi I_{xyz} r + 4I_{xyz} r \mathbf{K}(k) - 2\pi I_{xyz} + \pi I_{xyz} + 4I_{xyz} \mathbf{K}(k) \quad (\text{F.13})$$

$$\gamma_4 = 4\mathbf{K}(k) \left( -I_{x2} r - I_{x2} + \frac{I_{x2}}{\pi} \mathbf{K}(k) + I_{xz} + I_{xz} r - \frac{I_{xz} \pi r}{\mathbf{K}(k)} \right) \quad (\text{F.14})$$

$$\gamma_5 = 2\pi (-I_{xz} r^2 + I_{x2} r - I_{xz} + I_{z2} r) \quad (\text{F.15})$$

$$\gamma_6 = \pi (I_{x2} r^2 + I_{z2} r^2 + I_{x2} + I_{z2}) \quad (\text{F.16})$$

$$I_{x2} = I_x^2 \pi \quad (\text{F.17})$$

$$I_{z2} = I_z^2 \pi \quad (\text{F.18})$$

$$I_{xy} = I_x I_y \pi \quad (\text{F.19})$$

$$I_{xz} = I_x I_z \pi \quad (\text{F.20})$$

$$I_{xyz} = I_y I_z I_x \pi \quad (\text{F.21})$$

$$I_{x2y} = I_y I_x^2 \pi \quad (\text{F.22})$$

$$I_{yz2} = I_y I_z^2 \pi^2 \quad (\text{F.23})$$

$$I_{x2z} = I_z I_x^2 \pi^2 \quad (\text{F.24})$$

$$I_{xz2} = I_x I_z^2 \pi^2 \quad (\text{F.25})$$

# Bibliography

- [1] ABOUZAHERA, M.D.; AVENT, R. The 100-kW millimeter-wave radar at the Kwajalein Atoll. *IEEE Antennas and Propagation Magazine* 36, 2 (1994), 7–19.
- [2] ATKINSON, K. *An Introduction to Numerical Analysis*. John Wiley and Sons, Inc, 1988, pp. 108–111.
- [3] AVENT, R.K.; SHELTON, J. B. P. The ALCOR C-band imaging radar. *IEEE Antennas and Propagation Magazine* 38, 3 (1996), 16–27.
- [4] BELCHER, M. Tracking unresolved targets in theater ballistic missile defense. *Proceedings of the Twenty-Ninth Southeastern Symposium on System Theory* (1997), 426–429.
- [5] BURROWS, M. L. Two-dimensional ESPRIT with tracking for radar imaging and feature extraction. Tech. Rep. 1084, MIT Lincoln Laboratory, Aug. 2002.
- [6] BURROWS, M. L. Private conversations. 2004.
- [7] CAMP, W. W., MAYHAN, J. T., , AND O'DONNELL, R. M. Wideband Radar for Ballistic Missile Defense and Range-Doppler Imaging of Satellites. *Lincoln Laboratory Journal* 12, 2 (2000).
- [8] COPPOLA, V. The Method of Averaging for Eulers Equations of Rigid Body Motion. *Nonlinear Dynamics* 14 (1997), 295–308.
- [9] CORLESS, R., AND GIANNI, P. A reordered Schur factorization method for zero-dimensional polynomial systems with multiple roots. ISSAC '97, Maui Hawaii, pp. 133–140.

- [10] COSTEIRA, J., AND KANADE, T. A multi-body factorization method for motion analysis. *IEEE Proceedings of the Fifth International Conference on Computer Vision* (1995), 1071–1076.
- [11] CUOMO, K. M., PIOUS, J. E., AND MAYHAN, J. T. Ultrawide-band coherent processing. *IEEE Transactions on Antennas and Propagation* 47, 6 (June 1999), 1094–1107.
- [12] CYGANSKI, D. Private conversations. 2003.
- [13] EFROIMSKY, M. Precession of a freely rotating rigid body. *Journal of Mathematical Physics* 41 (2001), 1854–1895.
- [14] GOLDSTEIN, H. *Classical Mechanics*. Addison-Wesley Publishing Company, 1980, pp. 128–232.
- [15] GOLUB, G., AND LOAN, C. V. *Matrix Computations, 3rd Ed.* The Johns Hopkins University Press, 1996, p. 324.
- [16] GOLUB, G., AND PEREYRA, V. The differentiation of pseudo-inverses and nonlinear least squares problems whose variables separate. *SIAM Journal of Numerical Analysis* 10, 2 (Apr. 1973).
- [17] GOLUB, G., AND VAN DER VORST, H. Eigenvalue computation in the 20th century. *Journal of Computational and Applied Mathematics* 123 (2000), 35–65.
- [18] GRADSHTEYN, I., AND RYZHIK, I. *Table of Integrals, Series, and Products*. Academic Press, Inc, 1967, pp. 904–920.
- [19] HAARDT, M. Structured least squares to improve the performance of esprit-type algorithms. *IEEE Transactions on Signal Processing* 45, 3 (1997), 792–799.
- [20] HALL, D., AND LLINAS, J. An introduction to multisensor data fusion. *Proceedings of the IEEE* 85 (jan 2004), 6 – 23.
- [21] HALLIDAY, D., RESNICK, R., AND WALKER, J. *Fundamentals of Physics*. John Wiley and Sons, Inc, 1993, pp. 296–297.

- [22] HATCH, N., HOLL, D., AND CYGANSKI, D. Power-law scattering models and nonlinear parametric estimation for super-resolution radar. Tech. Rep. 1095, MIT Lincoln Laboratory, Apr. 2004.
- [23] HOLL, D. JR. Private conversations. 2003.
- [24] INGWERSEN, P. A., AND LEMNIOS, W. Z. Radars for Ballistic Missile Defense Research. *Lincoln Laboratory Journal* 12, 2 (2000).
- [25] IRO, H. *A Modern Approach to Classical Mechanics*. World Scientific, 2002, pp. 249–273.
- [26] KAGSTROM, B., AND RUHE, A. An algorithm for numerical computation of the Jordan normal form of a complex matrix. *ACM Transactions on Mathematical Software* 6, 3 (Sept. 1980).
- [27] KELLER, J. Geometrical theory of diffraction. *Journal of the Optical Society of America* (1962).
- [28] KESTER, L., AND THEIL, T. Fusion of radar and EO-sensors for surveillance. *Proceedings of the International Conference on Information Fusion* (2000), 3–9.
- [29] KUNG, S., ARUN, K., AND RAO, B. State space and svd based modeling methods for the harmonic retrieval problem. *Journal of the Optical Society Of America*. 73, 12 (1983), 1799–1811.
- [30] LATHI, B. *Modern Digital and Analog Communication Systems*. CBS College Publishing, 1983, pp. 213–317.
- [31] LATHI, B. *Signal Processing and Linear Systems*. Berkely Cambridge Press, 1998, pp. 47,252.
- [32] LIGGINS, M. E., AND CHONG, C. Y. Distributed multi-platform fusion for enhanced radar management. *IEEE National Radar Conference* (1997), 115 – 119.



- [33] MASUTANI, Y., IWATSU, T., AND MIYAZAKI, F. Motion Estimation of Unknown Rigid Body under No External Forces and Moments. *Proceedings of the IEEE International Conference on Robotics and Automation 2* (1994), 1066–1072.
- [34] MATSUNO, F., AND SAWADA, T. Parameter Estimation of Unknown Rigid Objects Moving Freely in Non-Gravity Field by Stereo Vision. *Proceedings of the International Conference on Intelligent Robots and Systems 3* (1998), 1455–1460.
- [35] MENSA, D. L. *High Resolution Radar Cross-Section Imaging*. Artech House, Inc., 1991, p. 47.
- [36] MOBUS, R., AND KOLBE, U. Multi-target multi-object tracking, sensor fusion of radar and infrared. *IEEE Intelligent Vehicles Symposium* (2004), 732 – 737.
- [37] MOLINA, A., AND MORENO, F. Comet hale-bopp as a free-rotation rigid body. *Journal of Astronomy and Astrophysics 347*, 1 (Mar. 1999), 366–369.
- [38] PIO, R. Euler angle transformations. *IEEE Transactions on Automatic Control 11*, 4 (1966), 707–715.
- [39] POTTER, L. A GTD-based parametric model for radar scattering. *IEEE Transactions on Antennas and Propagation 43*, 10 (Oct. 1995), 1058–1067.
- [40] RAO, B., AND ARUN, K. Model based processing of signals: a state space approach. *Proceedings of the IEEE 80*, 2 (1992), 283–309.
- [41] SCHEERES, D., OSTRO, S., HUDSON, R., DEJONG, E., AND SUZUKI, S. Dynamics of orbits close to asteroid 4179 toutatis. *International Journal of Solar System Studies 132*, 1 (Mar. 1998), 53–79.
- [42] SINGLA, P., MORTARI, D., AND JUNKINS, J. How to Avoid Singularity for Euler Angle Set? *Space Flight Mechanics Meeting Conference, Maui, Hawaii* (February 2004).
- [43] STUFF, M. A., SULLIVAN, R. C., THELEN, B. J., AND WERNESS, S. A. Automated two- and three-dimensional, fine-resolution radar imaging of rigid targets with arbi-

- trary unknown motion. In *Proc. SPIE Vol. 2230, p. 180-189, Algorithms for Synthetic Aperture Radar Imagery, Dominick A. Giglio; Ed.* (June 1994), pp. 180–189.
- [44] SYNGE, J., AND GRIFFITH, B. *Principles of Mechanics*. McGraw-Hill Book Company, 1959, pp. 314–380.
- [45] TOMASI, C., AND KANADE, T. Shape from motion from image streams under orthography: A factorization method. *ICCV* (1992).
- [46] TSIOTRAS, P., AND LONGUSKI, J. Analytic solution of euler’s equations of motion for an asymmetric rigid body. *ASME Journal of Applied Mechanics* 63, 1 (1996), 149–155.
- [47] VARBERG, D., AND PURCELL, E. *Calculus, 7<sup>th</sup> Edition*. Prentice-Hall, 1997, pp. 672–674.
- [48] VIGNAUD, L. Inverse synthetic aperture radar imaging of satellites. *International Journal of Imaging Systems and Technology* 9 (1998), 24–28.
- [49] WALKER, J. L. Range-Doppler imaging of rotating objects. *IEEE Transactions on Aerospace Electronic Systems* 16 (Jan. 1980), 23–52.
- [50] WELLS, D. *Theory and Problems of Lagrangian Dynamics*. Schaum Publishing Company, 1967, pp. 139–197.
- [51] WHITTAKER, E. *A Treatise on the Analytical Dynamics of Particles and Rigid Bodies*. Cambridge University Press, 1989, pp. 144–151.
- [52] WILKINSON, J. *Rounding Errors in Algebraic Processes*. Prentice-Hall, Englewood Cliffs, N.J., 1963, p. 39.
- [53] ZENG, Z. A method computing multiple roots of inexact polynomials. ISSAC ’03 Aug. 3-6, Philadelphia, pp. 266–272.
- [54] ZHOU, Y. Multi-sensor image fusion. *Proceedings of the IEEE International Conference Image Processing* (1994), 193–197.